2018

THE PHYSICAL BEHAVIOR AND CHARACTERIZATION OF NANOPOROUS SILICON AND DISPENSER CATHODE SURFACES

Tyler Lucius Corey Maxwell
University of Kentucky, tlva224@g.uky.edu
Digital Object Identifier: https://doi.org/10.13023/etd.2018.513

STUDENT AGREEMENT:

I represent that my thesis or dissertation and abstract are my original work. Proper attribution has been given to all outside sources. I understand that I am solely responsible for obtaining any needed copyright permissions. I have obtained needed written permission statement(s) from the owner(s) of each third-party copyrighted matter to be included in my work, allowing electronic distribution (if such use is not permitted by the fair use doctrine) which will be submitted to UKnowledge as Additional File.

I hereby grant to The University of Kentucky and its agents the irrevocable, non-exclusive, and royalty-free license to archive and make accessible my work in whole or in part in all forms of media, now or hereafter known. I agree that the document mentioned above may be made available immediately for worldwide access unless an embargo applies.

I retain all other ownership rights to the copyright of my work. I also retain the right to use in future works (such as articles or books) all or part of my work. I understand that I am free to register the copyright to my work.

REVIEW, APPROVAL AND ACCEPTANCE

The document mentioned above has been reviewed and accepted by the student's advisor, on behalf of the advisory committee, and by the Director of Graduate Studies (DGS), on behalf of the program; we verify that this is the final, approved version of the student's thesis including all changes required by the advisory committee. The undersigned agree to abide by the statements above.

Tyler Lucius Corey Maxwell, Student

Dr. T. John Balk, Major Professor

Dr. M. J. Beck, Director of Graduate Studies

THE PHYSICAL BEHAVIOR AND CHARACTERIZATION OF NANOPOROUS SILICON AND DISPENSER CATHODE SURFACES

DISSERTATION

A dissertation submitted in partial fulfillment of the requirements for the degree of Doctor of Philosophy in the College of Engineering at the University of Kentucky

By

Tyler Lucius Corey Maxwell

Lexington, Kentucky

Director: Dr. T. John Balk, Professor of Materials Engineering

Lexington, Kentucky

2018

ABSTRACT OF DISSERTATION

THE PHYSICAL BEHAVIOR AND CHARACTERIZATION OF NANOPOROUS SILICON AND DISPENSER CATHODE SURFACES

Nanostructured materials have received a surge of interest in recent years since it has become apparent that reducing the size of a material often leads to heightened mechanical behavior. From a fundamental standpoint, this stems from the confinement of dislocations. Applications in microelectromechanical devices, lithium ion batteries, gas sensing and catalysis are realized by combining the improvements in mechanical behavior from material size reduction with the heightened chemical activity offered by materials with a high surface-area-to-volume ratio. In this study, films of nanoporous Si-Mg were produced through magnetron sputtering, followed by dealloying using an environmentally benign process with distilled water. The film composition and structure was characterized both at the surface and throughout the film thickness, while the mechanical behavior was explored with nanoindentation.

Dispenser cathodes operate via thermionic emission and are an important area of interest in vacuum electron devices. While scientists have known for many years what elemental constituents are used to manufacture dispenser cathodes of excellent emission behavior, a fundamental understanding has yet to be realized. In this study, components of a scandate cathode that exhibited excellent emission behavior were characterized and used to inform the study of model thin films. Isolating relevant components of the scandate cathode for careful study could help inform future breakthroughs in understanding the working mechanism(s) of the scandate cathode. The structure, composition and electronic behavior of model W-Al alloy films were characterized experimentally and compared to computation. Moreover, a unique vacuum chamber was designed to activate modern thermionic dispenser cathodes, observe residual gas species present, and measure the work function through various state-of-the-art techniques.

KEYWORDS: Nanoporous; Silicon; Nanoindentation; Dispenser cathode; W-Al alloying

Tyler L. Maxwell

December 19th, 2018

THE PHYSICAL BEHAVIOR AND CHARACTERIZATION OF NANOPOROUS SILICON AND DISPENSER CATHODE SURFACES

By

Tyler Lucius Corey Maxwell

Dr. T. John Balk

Director of Dissertation

Dr. M. J. Beck

Director of Graduate Studies

December 19th, 2018

Date

Acknowledgements

This dissertation represents the culmination of my formal education and the beginning of my journey outside academia. Before entering college, I always thought that being educated was something that one would obtain such that he/she could then rest on his/her laurels perpetually. This naïve view dissolved rather quickly my freshman year at Berea College. At first, I was a little disappointed, but I now see how dull life would be without life-long learning. I also learned that achieving an education does not exclusively occur within the realm of academia. Here is to those individuals that inspired me and contributed in so many different ways to my own self-enrichment; it has made all the difference.

First off, I would like to thank my adviser, Dr. T. John Balk, for the opportunity to learn under his guidance. The countless hours we have spent discussing data and reviewing research papers has equipped me well as a budding young scientist. I am also grateful for the emphasis Dr. Balk has put in the learning of characterization techniques, beyond just knowing how to operate a machine. I feel it has helped develop my critical thinking skills in unique ways. I would like to thank Dr. Matthew Beck for providing supplemental insight into the research problems I have faced throughout my PhD. He is incredibly articulate and his enthusiasm is contagious. He and Dr. Balk complement each other well, and I am fortunate to have had the opportunity to study under their combined efforts. I would also like to thank the members of my committee including: Dr. Jonathan Wenk, Dr. Stephen Rankin, Dr. Matthew Beck and Dr. John Balk for taking the time to carefully consider this work and judge it based on merit. I would also like to thank NSF for funding the research on nanoporous silicon and DARPA for funding the research on dispenser cathodes.

I am also grateful for my lab mates, both past and present. We have shared experiences unique to our group, celebrated one another's successes and provided solace at failures. I would especially like to thank Dr. Nicolas J. Briot. He has been a presence even before I started my PhD and played a large role in my deciding to join the Balk group. His support has been unwavering, his advice has been sound and his integrity is inspiring. I would also like to thank Michael J. Detisch for all the help in managing the laboratories and help developing ideas by listening and providing input to my own rambling. Artashes Ter-Isahakyan was instrumental in challenging my ideas and in teaching machining techniques, however unconventional they may be.

My time at Berea College was no doubt some of the most important years in my life. The relationships that developed between myself and my peers, the faculty, and the community left me a transformed individual. Beyond the rigorous curriculum offered by the Physics, Math and Chemistry departments that garnered my critical thinking skills, I learned creativity through the other facets a liberal arts education offers. Specifically, I would like to thank Dan Brewer, Dr. Martin Veillette, Dr. Tracy Hodge, Dr. James Blackburn-Lynch, Dr. Jing-Pang Lee, and Dr. Fred de Rosset. I would especially like to thank the late Amer Lahamer, whose simple belief in my ability pushed me to achieve things I would have never thought possible. The character and work ethic of the individuals at Berea College are world-class. I was shown a world of equality, self-respect and integrity that I will always carry with me. I am also deeply grateful to Marty Miller, Rohan Isaac, Tanner Slagel, Titay Ayano, Dipendra Chapagain, and Franceska Mehmeti for their friendship. I am better for having known each of you.

The late Carol Howlin, or Spud, was a dear friend whose guidance led me to Berea College and knew the opportunities that I would be afforded by having gone there. Jim and Barbara Holmes have been like a second family to me that I do not get to see often enough. Their support and encouragement have been truly invaluable. I was afforded opportunities that impacted my life in a large way by having known the Holmes family.

My own family have gone to extraordinary lengths to provide me opportunities they never had. I am in awe to look back on the sacrifices that they endured to ensure I had the best chance of success. I would especially like to thank James Derek Sumner, the late James Estel Maxwell, the late Lora Alice Maxwell and – of course – Donna Lynn Maxwell for the love and support that were manifested in so many different ways over the years. I will never forget it. I would also like to thank my brothers and sisters for keeping me grounded, especially DeDee DeLaine Skelton.

Lastly, I want to thank my wife, Franceska Mehmeti. The love, support, encouragement, and selflessness that you embody is humbling. With you, I find a sense of inspiration and love beyond any I have ever known. I love that we build each other up such that we have become better individuals. I look forward to the things we will accomplish together.

Table of Contents

List of Tables

List of Figures

List of Equations

1 Introduction

Two different thin film binary alloy systems are the subject of this dissertation; namely silicon-magnesium (Si-Mg) and tungsten-aluminum (W-Al). The overarching contribution from this work is an improved understanding of how to fabricate each material system using a non-equilibrium physical vapor deposition process, characterize the film structure and chemical composition, examine the mechanical behavior insofar as the film dimensions allow, study the surface chemical state and interpret these results in the parlance of energy storage/conversion or thermionic dispenser cathode operating mechanisms. During this process, I also designed and constructed a unique vacuum chamber – with the help of a team – that can be used to study specific material parameters and indirectly inform the working mechanism(s) of thermionic dispenser cathodes.

The thin films manufactured throughout this dissertation were created through a physical vapor deposition process known as magnetron sputtering, which is an attractive technique to create thin films in a reproducible manner due to the wide variety of control mechanisms one has in the deposition process. Sputtering is a non-equilibrium process that lends itself well to the study of binary systems where there are stringent stoichiometry requirements. In many instances, the non-equilibrium nature is beneficial because it allows one to study interesting phases at room temperature that the equilibrium phase diagram for binary alloy systems would otherwise preclude. Moreover, the fabrication of thin films is one method that can be used to increase the surface area-to-volume ratio.

The attractiveness in increasing the effective surface area per unit volume of a given material stems from the new properties that emerge that leads to a wide variety of

applications that benefit from doing so. The most intuitive method to increase the surface area and decrease the volume of a material is to simply reduce the dimensions, giving way to the enthusiasm for research on nanowires, nanoparticles and thin films, for example. Another approach to increase the effective surface area is to introduce pores into a given material. There are several techniques that can be used to create porous materials, but the method used in this dissertation is known as dealloying and was only used on the Si-Mg binary alloy system.

A large portion of this dissertation is dedicated to the fabrication and characterization of nanoporous silicon and subsequent mechanical testing. The motivation for using silicon stems from its application in energy storage devices like lithium-ion battery research. Silicon has the ability to absorb large quantities of lithium, having a theoretical capacity of 4200 mAh g^{-1}. This stands in stark contrast to the commonly used carbon-based anode with a relatively low theoretical capacity of 372 mAh g^{-1}. For perspective, this means each silicon atom can accommodate 4.4 lithium atoms, which naturally leads to a large volume expansion. Silicon is a brittle material and cannot absorb lithium without pulverizing. However, it has been observed that by making silicon nanosized, it can exhibit ductility without failing. In single crystalline nanopillars, for example, pillars with and average diameter below 310 nm exhibit ductility due to dislocation confinement [1]. Additionally, nanostructured silicon reduces the diffusion distance of lithium and helps promote chemical activity while relieving absolute volume expansion that results from lithiation. The nanoporous silicon created in this study exhibits a heterogeneous structure/chemical composition throughout the film thickness. The resulting characteristics of this film appear to be desirable when analyzed in the light of

nanostructured silicon anodes that display long cycle life and good rate capabilities. Beyond the apparently desirable structure/chemical composition, the process that was used to fabricate these nanoporous thin films of silicon is environmentally benign. The process of dealloying involves only distilled water to remove the sacrificial magnesium and is a free corrosion process that does not require a potentiostat. The novelty of the technique alone is remarkable, but the true test of this material application will come when it has undergone rigorous testing as an anode in a lithium-ion battery. The work of Feng et al. gives an excellent overview of the recent advances in nanostructured silicon as a lithium-ion battery, complete with battery performance and current issues [2].

The field of study that is thermionic dispenser cathode research is largely undeveloped in terms of understanding the fundamental working mechanism(s) that lead to excellent emission behavior for cathodes that contain complex chemistries. Porous tungsten pellets that are impregnated with BaO, CaO, and Al_2O_3 are termed the B-type cathodes. Recently, there has been increased interest in understanding scandate cathodes, which are just B-type cathodes that also have Sc_2O_3 in the mix. The reason for the interest in scandate cathodes stems from their ability to operate at lower temperatures than other dispenser cathodes and still emit well, thereby increasing the longevity of the scandate cathode [3]. As one might imagine, attempting to understand the scandate cathode that has a more complex chemical make-up than the B-type cathode – which is already not well understood – makes for a challenging task. The approach that was taken in this dissertation - to add to the literature already available on cathode research - was to study a scandate cathode that exhibited excellent emission behavior and attempt to isolate components that appear to be of interest and study those isolated components in what could be described as

a model system. We observed small concentrations of what appears to be aluminum embedded in tungsten grains of a cathode of excellent emission behavior. We then created a model system with thin films to study the effect alloying aluminum with tungsten has on the electron work function. We also observed binding energy shifts in the tungsten core levels with XPS in a scandate cathode of excellent emission behavior and also in the aluminum alloyed tungsten films. It is clear that this effect leads to a lower overall work function at room temperature, but it is not clear if aluminum alloyed into the tungsten matrix is a critical feature of scandate cathodes of excellent emission behavior.

The unique vacuum system that was designed for cathode characterization has the ability to study the electron work function under vacuum conditions at temperatures ranging from room temperature up to approximately 1200°C. The system is also capable of analyzing residual gases in the vacuum chamber that have a mass range from 1 – 300 AMU to help inform the working mechanism(s) of thermionic dispenser cathodes that allow excellent emission behavior at high temperatures. The system is also equipped with two photoemission systems that allow the probing of material work functions that lie within 1.24 – 7.0 eV. There are other vacuum systems that are equipped with these characterization techniques, but none to our knowledge that is equipped with these characterization techniques and can function in conjunction with a heater whose capability maxes out at sample temperatures around 1200°C. In summary, a novel dealloying technique was developed to produce nanoporous silicon with retained magnesium films on the order of 1μm in thickness using an environmentally benign method. The ligament size, crystal structure, and chemical composition appear to be desirable characteristics in applications involving lithium-ion batteries and the simple, non-hazardous method makes

this attractive as well. The mechanical behavior of the as-dealloyed and annealed nanoporous silicon films were subsequently tested with nanoindentation in both the time and frequency domains. Both the as-dealloyed and annealed films exhibit time-dependence, but this seems to stem largely from plasticity. The reduced modulus and hardness of the films were reported as well. A fundamental study on the way that aluminum alloys with tungsten was performed due to the discovery of small amounts of aluminum alloyed in tungsten grains in a scandate cathode of excellent emission behavior. It was discovered that alloying aluminum with tungsten does indeed decrease the electron work function at room temperature and could therefore help promote the emission of electrons at high temperatures. It is unclear, however, if this is a critical aspect of scandate cathodes that leads to excellent emission behavior at lower operating temperatures than in B-type cathodes, for example.

2 Background

2.1 Dealloying

Dealloying is a corrosion process where one constituent of a multi-constituent solid solution is preferentially removed leaving a skeleton of the other constituents [4]. The sponge-like geometry of the resulting structure is a three-dimensional, bi-continuous open porous structure. This technique has existed for many years dating back to Incan civilizations where copper was removed from a homogeneous alloy of Au-Cu in a process called depletion guilding [5]. This resulted in a lustrous gold surface that imitated pure gold and was often used for decoration. In 1979, A.J. Forty was at the forefront of the investigation of the dealloying mechanisms studying Ag-Au alloys dealloying in nitric acid [6]. This resulted in the well-known and easily produced nanoporous gold that has become the standard against which all other dealloying systems are compared. It was not until 2001 when Erlebacher propsed a detailed description of the atomistic evolution of nanopores that a much more sophisticated approach was established for the methodical selection of dealloying materials/parameters [7].

2.1.1 Guidelines for Dealloying

Based on a large number of experiments with several different alloy systems, a standard set of characteristics have been developed to better understand what is required for dealloying to take place, such that a controlled nanoporous structure results [8]:

Galvanic Series Separation: The difference in corrosion potential ($\Delta\varphi$) of the elements in the precursor must be separated by a few hundred millivolts. In other words, there needs to be a significant difference between the metals in terms of the galvanic series.

In most cases, the difference between metals in the galvanic series is not large enough to be dealloyed via free corrosion. As a result, a potential is applied to force the dissolution of the less noble element.

Parting Limit: It has been observed that the less noble (LN) element composes the larger atomic fraction of the precursor alloy, i.e. before dealloying occurs. From experiment (and my own personal experience) this is one of the major deciding factors to determine whether or not selective dissolution will occur. Typically, there is a range over which dealloying will occur and this range is known as the parting limit. If the amount of more noble (MN) atoms is too rich, dealloying will not take place because of surface passivation. Conversely, if the amount of MN atoms is too low, there will not be a "backbone" to which other MN atoms can move by surface diffusion.

Solid Solution Homogeneous Alloy: The precursor must be a homogeneous solid solution with no phase separation prior to dissolution. One of the reasons the Au-Ag system is a great candidate is because it is completely miscible across the composition range and no phase separation occurs [9]. It should be clear that there is no hidden skeleton that is being excavated, but rather created as the dynamic dissolution/surface diffusion process occurs monolayer by monolayer.

Rate of Surface Diffusion vs. Dissolution: It has been observed that the surface diffusion of MN atoms must be sufficiently fast. There is a competing effect between surface diffusion of MN atoms and dissolution of LN atoms, such that dealloying can continue unimpeded.

2.1.2 Critical Potential

The critical potential (the lower bound is sometimes referred to as overpotential) has been observed to be an important parameter when discussing dealloying. Critical potential is perhaps a bit of a misnomer because it does not signify a single value for which dealloying occurs, but rather a range of values. Illustrated in Figure 2.1 is a polarization curve of a single-phase alloy undergoing selective dissolution. Below the critical potential, dissolution does not occur and a passive-like layer is formed [10]. Conversely, above the critical potential dissolution of one or more of the LN elements takes place and results in a sponge-like structure consisting of the MN elements [10]. However, if the potential is continuously raised, the leaching process will occur too fast and result in a structure that is cracked and not nanoporous. In other words, the critical potential is the specific range where leaching of the LN element occurs, but not too fast.

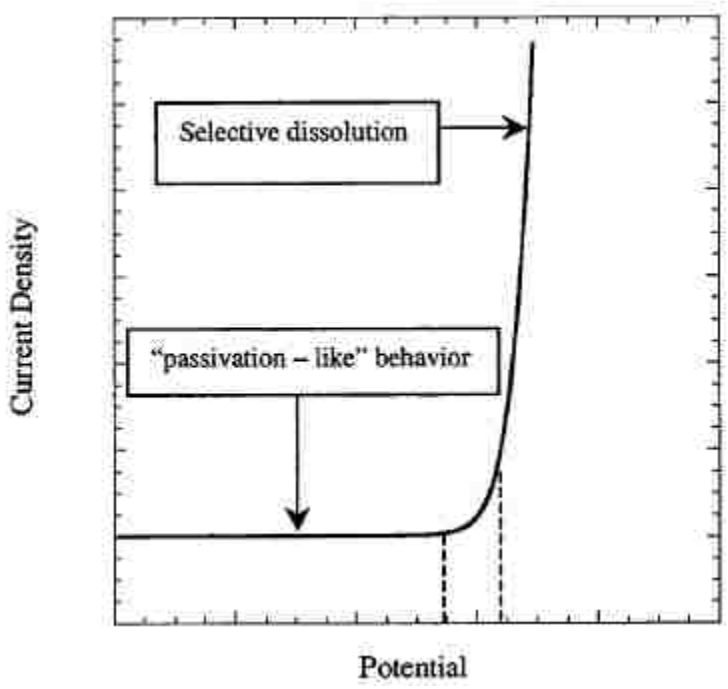

Figure 2.1 Schematic depiction of current/potential behavior of a single-phase alloy undergoing selective dissolution. The area between the two dotted lines represents the region where one might observe the critical potential. The lower potential represents the potential where the leaching of the LN element is initiated and the upper potential represents the limit on how quickly the LN element is leached (Reproduced from [10] with permission from The Electrochemical Society, Inc.).

One should take careful note of the gradual current density rise as potential increases because this is the region indicative of the critical potential for a given alloy. The physical explanation for why there is some ambiguity in defining a certain value is the result of competitive kinetic interactions occurring at the nanoscale [10]. For example, the relative rate of LN element dissolution to MN element surface diffusion. A detailed description of kinetic interactions and pore formation are given below.

2.1.3 Spinodal Decomposition

Understanding the physical reasons for the agglomeration of MN atoms that surface diffuse (adatoms) is key to understanding porosity formation. The first step in this solution

involves treating the MN adatoms (silicon in this case) to be confined to the monolayer sitting on top of undealloyed material. The free energy density (*f*) of a regular solution at the interface is given by Equation 2.1 and is a necessary step in determining the solubility of MN adatoms at the interface [7].

$$f(c,T) = \alpha c(1-c) + k_B T[cln(c) + (1-c)\ln(1-c)]$$

Equation 2.1 Free energy density of a regular solution at the interface during dealloying.

Where c is the mole fraction of silicon, α is a function of interaction energies between silicon and electrolyte, k_B is Boltzmann's constant, and T is absolute temperature. The solubility of MN adatoms can be considered as the equilibrium concentration of MN adatoms [7]. As the LN element is dissolved into solution, this represents a non-equilibrium condition where the driving force that allows the MN adatoms to agglomerate into clusters is the result of local site MN adatoms having an occupancy fraction much greater than the equilibrated concentration given by Equation 2.1. The agglomeration of MN adatoms onto nearby clusters would be considered uphill diffusion and is the result of composition fluctuation that ultimately leads to a lower free energy state [7]. However, the system becomes unstable at long length scales such that the characteristic length, λ, previously mentioned is very close to the final ligament spacing observed once dealloying is complete. This is formally known as spinodal decomposition [11].

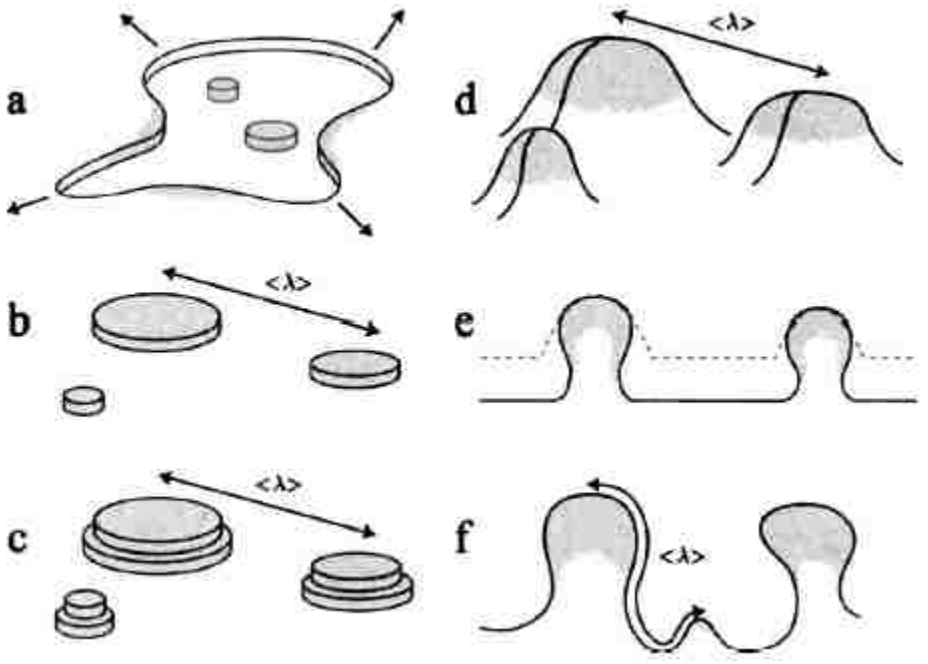

Figure 2.2 Schematic illustration of pore formation during dealloying. a) Stripping of LN species and agglomeration of MN species. b) Formation and coarsening of MN-rich mounds. c) Second layer dissolution of LN atoms and surface diffusion. D) Reduced accumulation of MN atoms at the base e) Undercutting of the hills and f) formation of new mounds (Reproduced from [8] with permission from The Electrochemical Society, Inc.).

2.1.4 Rate Laws for Diffusion and Dissolution

A bond-breaking model was used to describe diffusion such that atoms could translate into adjacent sites by surmounting an activation barrier. The height of the barrier is given by the sum of the surrounding bonding energies of all adjacent atoms. The rate at which an atom will translate into an adjacent site is given in Equation 2.2, where E_b is the bond energy, k_B is Boltzmann's constant, T is absolute temperature, ν_D is the attempt frequency, and n is the number of adjacent atoms [8].

$$k_n^{diff} = \nu_D \exp\left(-\frac{nE_b}{k_B T}\right)$$

Equation 2.2 Adatom diffusion rate during dealloying.

The model used to describe the dissolution of the LN atoms is given in Equation 2.3, where k_n^{diss} is the dissolution rate, ν_E is the product of the attempt frequency and a term that depends on the activation entropy for dissolution, φ is the applied potential, and the other terms are defined above. There is a simple interpretation to the rate law equations that govern dealloying; an atom must overcome an activation barrier of height nE_b during both diffusion and dissolution, but this height can be lowered during dissolution by an amount equal to the applied potential (φ) [8].

$$k_n^{diss} = \nu_E \exp\left(-\frac{(nE_b - \varphi)}{k_B T}\right)$$

Equation 2.3 Kinetic rate equation for dissolution of less noble elements [8].

2.2 Porous Silicon

Porous silicon (PS) was first reported by Uhlir in the 1950's through experiments on the electrolytic shaping of germanium and silicon [12]. Uhlir noticed that the surface was not polished as he had hoped and the experiment was deemed a failure. Afterwards, Turner began performing electropolishing experiments on silicon at Bell Laboratories and explored this area further [13]. Porous silicon remained virtually unexplored until the 1990's when Canham et al. began to investigate the optical properties of PS [14], at which point interest in the scientific community began to grow.

There are two main techniques used to create PS: stain etching and anodic etching. Stain etching is a simple and scalable procedure, but does not allow the user to have optimum control over parameters as compared to anodic etching. For this reason, stain etching is not as widely utilized within the scientific community and will only be briefly discussed.

Stain etching of silicon is a method based on the use of hydrofluoric acid (HF) and intense oxidizing agents (hydrogen peroxide) such that a porous structure forms, without the use of a power supply to drive the process [15]. The etching occurs as the oxidizing agent reacts with the surface of silicon and is subsequently dissolved by the HF. The reaction is considered to be a closed circuit electrochemical reaction because the anodic and cathodic reactions occur on the surface of the silicon.

There have been other methods used to create PS structures that are either a top-down or bottom-up variety. Metal assisted chemical etching (MACE, another example of stain etching) is one of the more notable techniques that have been developed in recent years [16]. The etching is done by the catalysis of a metal coating on the silicon. Since the etching is more vigorous at the metal-silicon interface it causes the metal to sink into the silicon. One can pattern the metal and overlay it on the silicon to create nanostructures in a process called template based MACE [16].

2.2.1 Anodic Etching

The most common method to produce PS utilizes the anodic etching technique, sometimes referred to as simply anodization [17]. Here a silicon wafer is typically etched by submerging it in a biased etching cell containing ethanol and HF. There are three common geometries that the etching cell can have: the single tank cell, the lateral anodization cell, and the double tank cell. Each of these geometries are shown in Figure 2.3. A common material used for the cathode is Pt because it is conductive and resistant to HF attack. As a potential bias is applied to the electrode in any of the tank cells, current will flow and etching results [18].

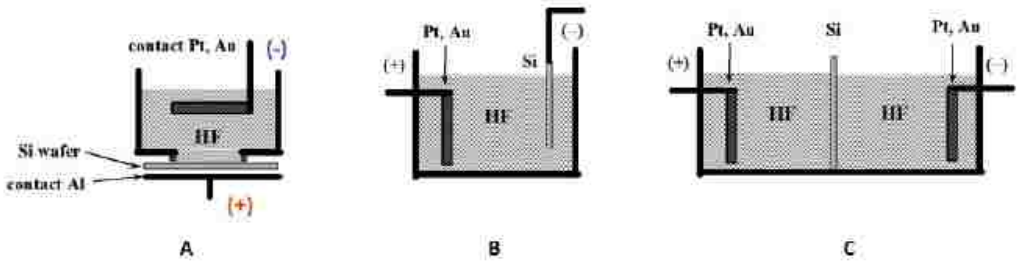

Figure 2.3 Schematic showing the different geometries of silicon etching cells. A) Single tank cell, B) is a lateral anodization cell, and C) is a double tank cell [18].

Typically, the silicon wafer is polished before inserted into the etching cell such that the surface is hydrophobic [19]. The ethanol in solution serves two purposes: 1) It is used to increase the wettability of the silicon surface such that the electrolyte can penetrate deeper into the pores and 2) it helps whisk the H_2 bubbles that form during anodization away from the surface [19]. In this way, there is a homogeneous current density that can be maintained that results in the formation of porous silicon. The typical controllable parameters during etching are: the applied anodic current density, etching time and concentration of solution. These can be used to control the resulting microstructure of the silicon.

2.2.2 Doping Considerations

One of the major factors that affects pore growth is how the sample is doped. In p-type silicon there are an excess of holes whereas in n-type silicon there are an excess of electrons. Due to the dissolution chemistry it has been commonly agreed upon by scientists that a hole supply from the bulk silicon is a necessary condition to create porous silicon [20]. Therefore, hole supply can be regarded as the limiting reagent in the dissolution reaction and an understanding of hole generation in both n and p type silicon is essential.

Since holes are the majority carriers in p-type silicon, anodization causes the silicon substrate to become forward biased [17]. That is to say that the p-type silicon is connected to the positive terminal of the electromotive force (emf). This results in a forward bias in the substrate and causes current to flow as a large supply of holes accumulate in the p-type silicon [17].

Electrons are the majority carriers in n-type silicon. When the n-type silicon substrate is anodized it will put it into reverse bias [17]. That is to say that the substrate will be connected to the negative terminal on the emf. This is similar to the reverse bias of a p-n junction diode. At low applied potential there will be a very low current flow and holes are not abundant [17]. Under these conditions, etching is severely limited and photons are utilized to stimulate hole supply. See Figure 2.4 for current-voltage curves.

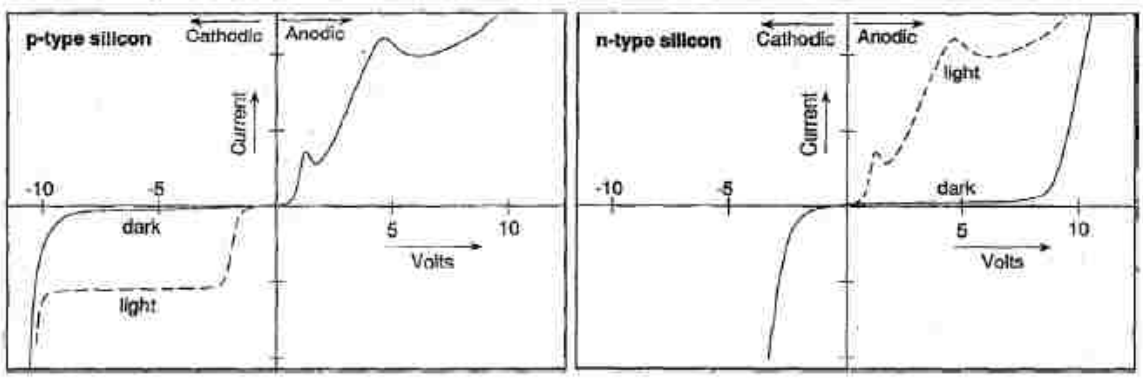

Figure 2.4 These current-voltage curves illustrate typical curves that would be seen for the anodic etching of n and p type silicon substrates (Reproduced from [21] with permission from Elsevier).

2.2.3 Morphology

There are a wide array of geometries that can be formed through the dissolution of silicon. The classification of pore sizes are summarized in Table 2.1. A complete study is

beyond the scope of this dissertation. As a result, an overview of some of the more common geometries are summarized along with controlling parameters in Table 2.2.

Table 2.1 Pore size as defined by IUPAC (Reproduced from [19] with permission from Elsevier).

Pore width	Pore type
< 2 nm	Micro porous porous
2 – 50 nm	Meso porous
> 50 nm	Macro porous

Table 2.2 Controllable parameters that affect the resulting pore size and morphology of the silicon wafer (Reproduced from [19] with permission from Elsevier).

Increasing the values of	Porosity	Etching rate
HF concentration	Decreases	Decreases
Current Density	Increases	Increases
Anodization time	Slightly increases	Slightly decreases
Wafer doping (p-type)	Decreases	Increases
Wafer doping (n-type)	Increases	Increases

A natural starting point for describing a porous material would be its porosity (P) and thickness (t). These are given by the following relations [19]:

$$P = \frac{m_1 - m_2}{m_1 - m_3}$$

Equation 2.4 Calculation of film porosity [19].

$$t = \frac{m_1 - m_3}{\rho A}$$

Equation 2.5 Calculation of film thickness [19].

Where m_1 is the mass of the sample before dissolution, m_2 is the mass of the sample after dissolution and m_3 is the mass of the sample after removal of the porous layer. While doping level and doping type play a key role in the resulting pore size and microstructure, there are other parameters that also affect dissolution such as electrolyte composition, current density, and dissolution time[19]. Some general pore morphologies are given in Figure 2.5.

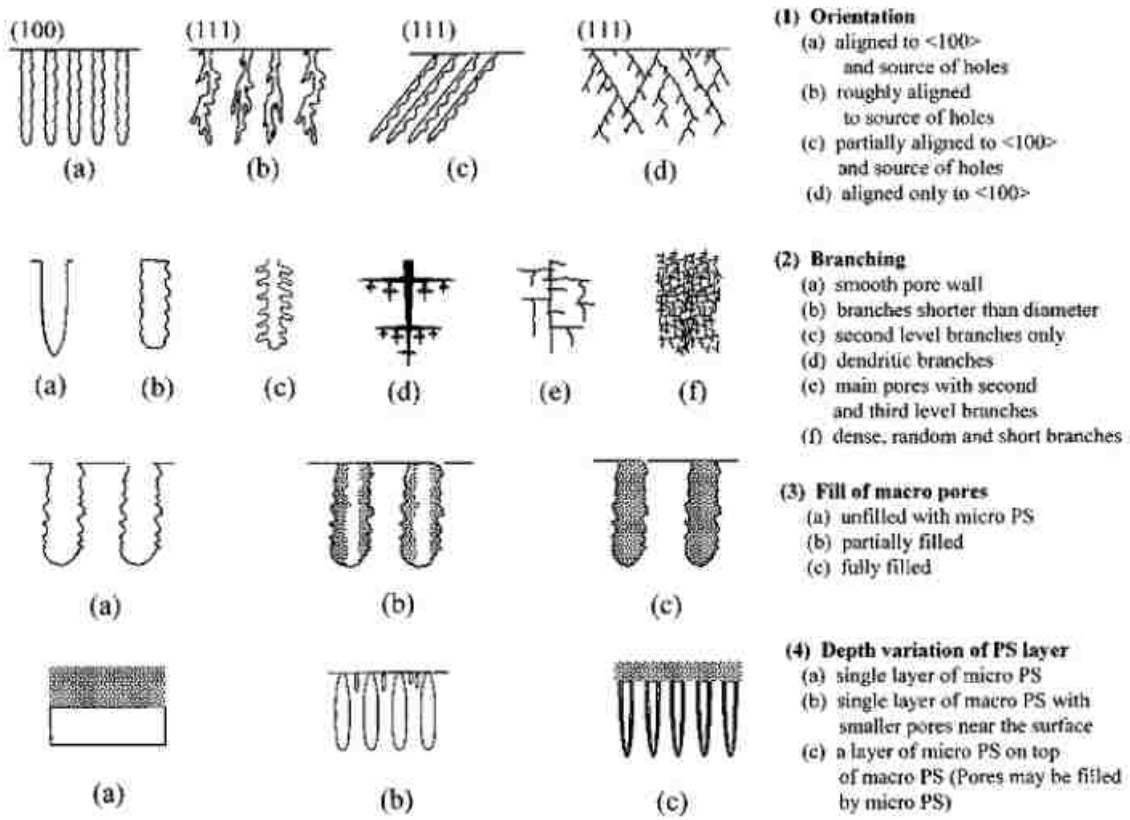

Figure 2.5 An overview of the different types of pore morphologies that have been observed by etching silicon (Reproduced from [22] with permission from The Electrochemical Society, Inc.).

2.2.4 Hierarchal Structure and Nanoporous Silicon

The most ubiquitous binary system for dealloying is that of Au-Ag, which is a well-behaved system that has been the subject of intense research [7, 8]. Upon dealloying, this system produces ligaments that are of uniform dimensions that create the bi-continuous structure. More recently, nanoporous materials that exhibit a hierarchal (multimodal) structure have been developed and studied [23-25]. Systems that have such structural characteristics are defined by having different classes of ligaments. This can be beneficial in engineering applications where mass transport and chemical activity are desired [26, 27]. There have been several studies on systems containing silicon that take advantage of this structural hierarchy for applications in lithium-ion batteries [28-30]. The study by Hao et al. incorporated a ternary alloy of Si-Ag-Al that was subsequently dealloyed in a solution of HCl [28]. The ternary alloy was fabricated through the use of an induction melter in an inert atmosphere of argon. The bimodal structure that resulted is shown in Figure 2.6.

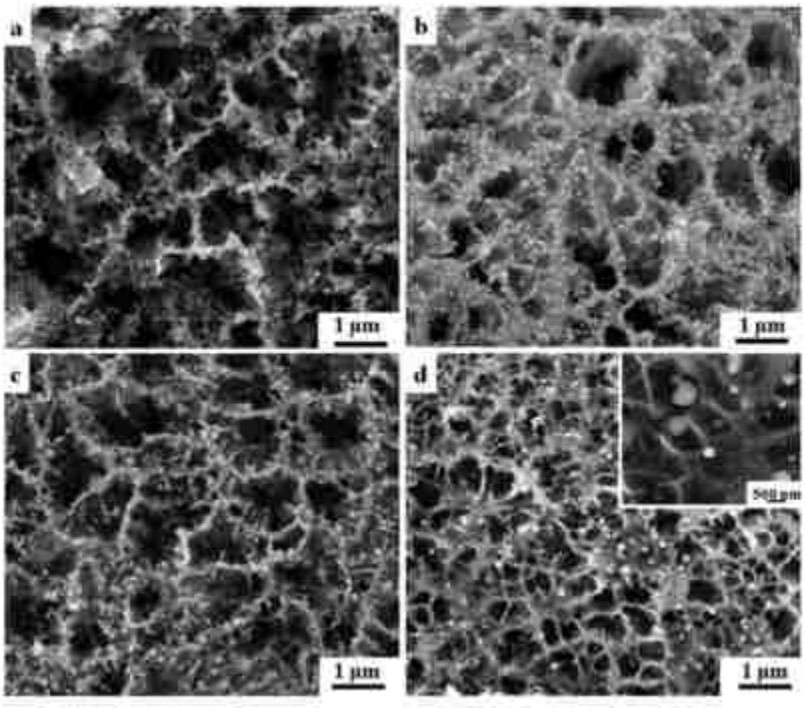

Figure 2.6 SEM images of the dealloyed Si-Ag-Al ternary alloy in 0.1 M HCl solution for a) 2, b) 5, c) 10 and 4) 24 hours (Reproduced from [28] with permission from The Royal Society of Chemistry).

Using electrochemistry to create nanoporous materials is not the only technique that can be to create nanoporous materials. Liquid metal dealloying (LMD) is a recent technique that was first published in 1959 by Harrison and Wagner, but studied further by Kato et al. [27, 29-32]. LMD is different from electrochemical dealloying in that it does not rely on a corrosion reaction in an aqueous solution, but on a metallurgical reaction between an alloy precursor and a metallic melt [29]. It is an attractive technique because electrochemical dealloying tends to require precious metals for the process. Of particular interest to the topic of this dissertation was the method used by Kato et al. to produce np Si [29, 30]. In that study, np Si was produced through LMD a Si-Mg alloy in a metallic melt of Bi. Subsequently, the Bi was corroded away with 1 M nitric acid, leaving the np Si intact. The resulting nanoporous structure is displayed in Figure 2.7.

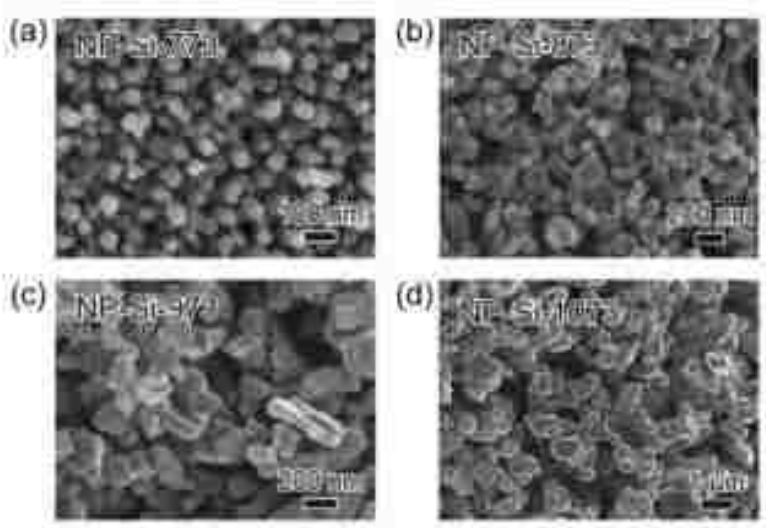

Figure 2.7 SEM images (a)-(d) corresponding to the structure obtained after annealing the np Si at temperatures from 773 to 1073 K (Reproduced from [30] with permission from Elsevier).

The motivation, in part, for pursuing the work on nanoporous silicon and using the Si-Mg system has foundations here at the University of Kentucky and was discovered serendipitously by Lei Wang [33]. Wang had made several attempts to make nanoporous iridium through dealloying of several binary alloy systems, but found that Ir-Mg was able to dealloy in the presence of benign substances like ethanol and water through free corrosion [33]. This was then extrapolated to other binary metal systems and shown to produce nanoporous structures with relative ease [33]. Jiang took the method developed by Wang et al. and applied it to thin films of Si-Mg [34]. Jiang et al. was able to create nanoporous Si thin films by using magnetron sputtering and dealloying in distilled water at 50°C. A gradient sample shown in Figure 2.8 was used to determine the parting limit for the Si-Mg system, which was 57 at.% Si [34]. Then homogeneous film compositions were sputtered and dealloyed using the parting limit range discovered on the gradient films. The homogeneous films produced a well-defined bi-continuous structure characteristic of nanoporous metals, as observed in Figure 2.9. Jiang et al. successfully created nanoporous

silicon films with thickness up to 200 nm, but had difficulties creating thicker films (600 nm >) due to delamination and excessive corrosion, as depicted in Figure 2.10. Jiang et al. needed to create thicker films to accurately extract film mechanical behavior.

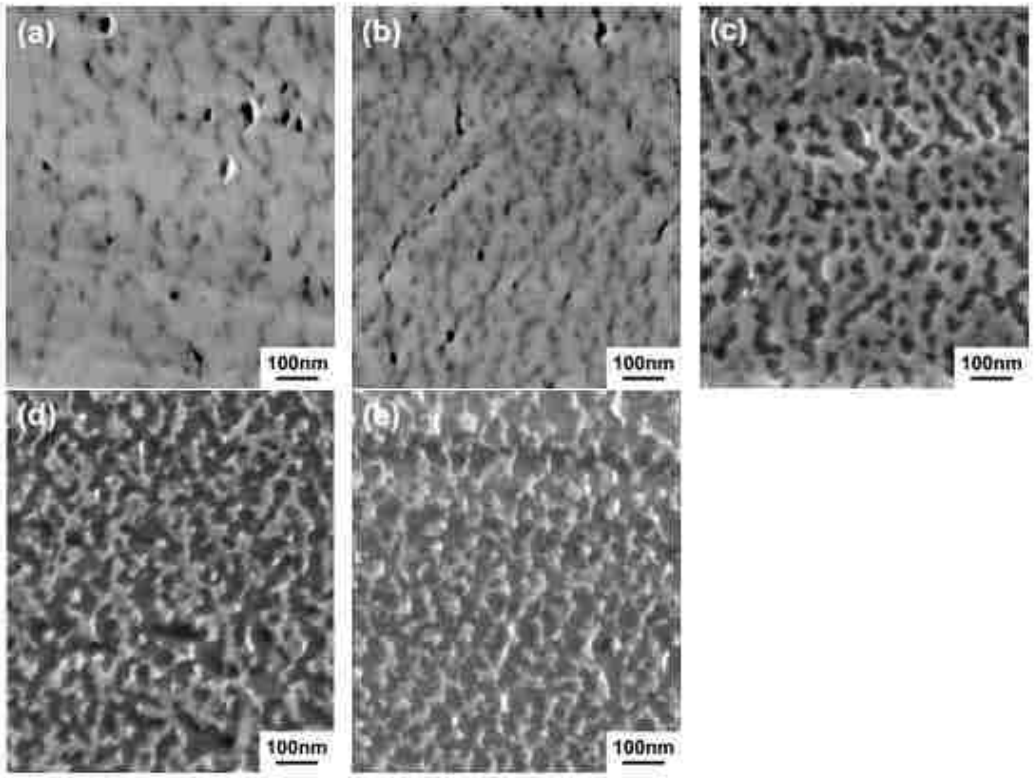

Figure 2.8 Gradient samples of Si-Mg with varying precursor compositions after dealloying. One can observe that in images (a) and (b) dealloying is incomplete and there is not a bi-continuous structure, this is more characteristic of passivation. In contrast, images (d) and (e) show large cracks in the film and islands of stand-alone material. The film pictured in (c) displayed the best microstructure and had a parting limit of 57 at. % Si [34].

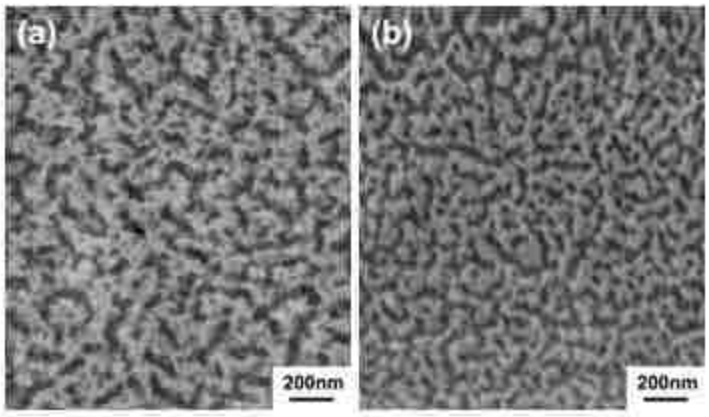

Figure 2.9 A 200 nm thick nanoporous Si film after dealloying. (a) represents the as-dealloyed structure, while (b) shows the ligaments have coarsened after vacuum annealing at 400°C [34].

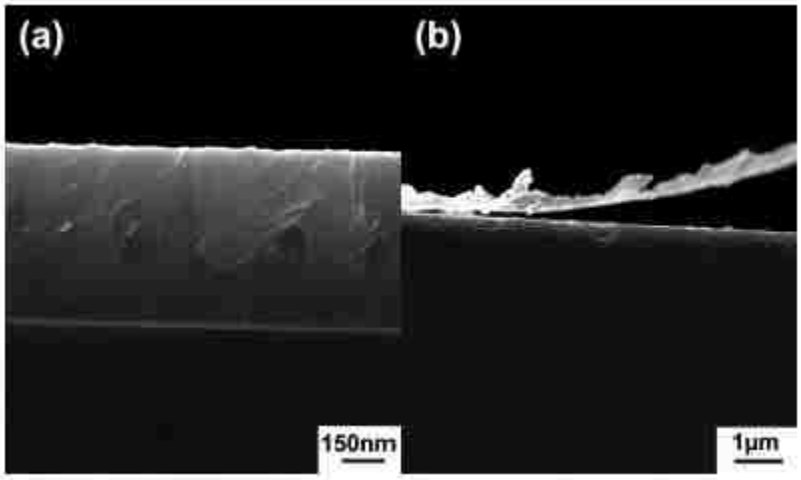

Figure 2.10 (a) cross-section of a 600 nm precursor film and (b) after dealloying [34].

2.3 Nanoindentation and Non-ideal Materials

The mechanical behavior of materials is of paramount interest for engineering applications. Nanoindentation is an attractive technique for determining the mechanical behavior because of its experimental simplicity and ability to probe small volumes of material on the order of 1 μm or less [35-37]. Additionally, there are a wide variety of indenter tips, shown in Figure 2.11, each having specific geometries that can be tailored to

the information required from the sample of interest [38]. The indenter tip used to characterize the materials in this dissertation was the Berkovich because it is better suited for studies that probe small-scale materials [38].

The seminal work by Oliver and Pharr introduced in 1992 had great implications because it meant that researchers no longer had to image indents after performing nanoindentation testing because the tip area function could be modeled with a high degree of accuracy [39]. The tip area function could be modeled according to the polynomial in Equation 2.6.

$$A = \sum_{n=0}^{8} C_n (h_c)^{2-n}$$

Equation 2.6 Tip area function model developed by Oliver and Pharr [39].

Where A is the contact area and $C_0 \ldots C_8$ are constants determined by curve fitting procedures [37]. Additionally, they introduced the continuous stiffness measurement (CSM) technique that would allow scientists to accurately obtain mechanical information as the indenter is pressed into the sample by oscillating the tip [39]. In this way, data could be obtained as a function of depth.

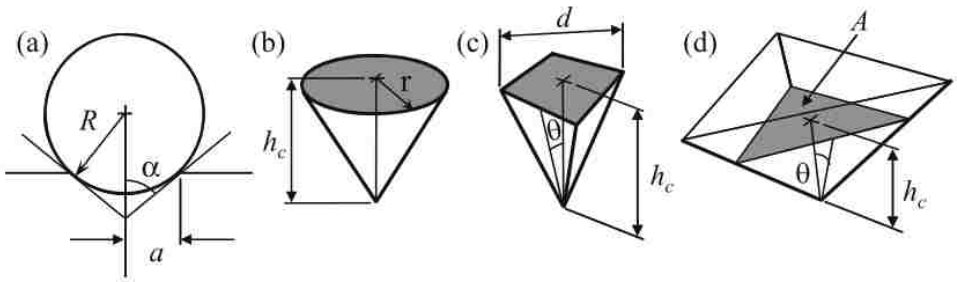

Figure 2.11 Schematic showing several different indenter tip geometries: (a) spherical, (b) conical, (c) Vickers, and (d) Berkovich. The cube corner and flat punch (not pictured) are also useful geometries (Reproduced from [38] with permission from Springer Nature).

Prior to the advent of the CSM technique, nanoindentation tests were relatively rudimentary and did not require expensive electronics. Nevertheless, the important quantities that were obtained from a typical load-displacement curve were the maximum load, P_{max}, the maximum displacement, h_{max}, and the elastic unloading stiffness, $S = dP/dh$. These quantities are shown in Figure 2.12. The residual indent in the sample material would be imaged such that the contact area, A, of the impression could be obtained. Material parameters like the elastic modulus and hardness could then be obtained by experimentally determining these values, as shown in Equation 2.7 - Equation 2.9.

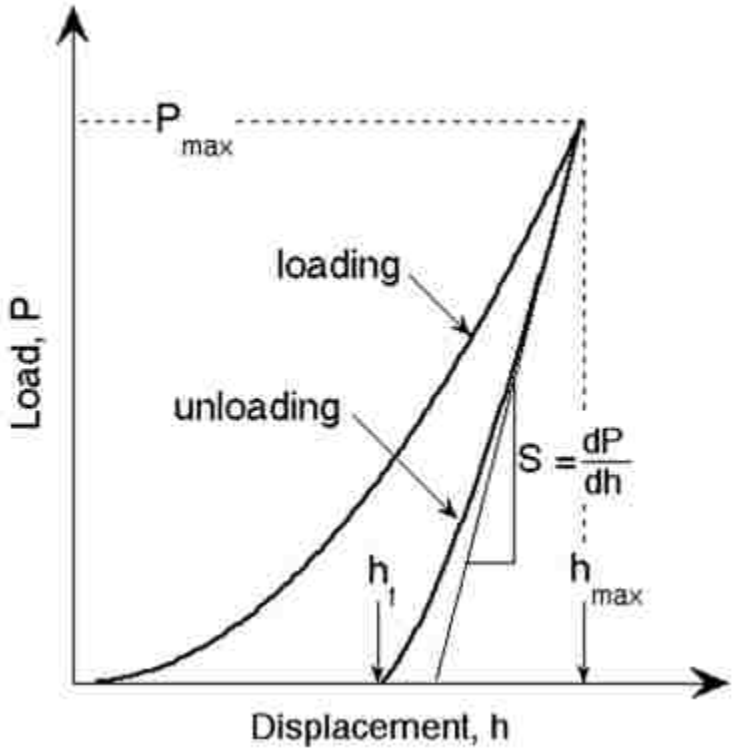

Figure 2.12 Schematic of a typical load-displacement curve obtained with a Berkovich tipped indenter showing important parameters obtained from experiment (Reproduced from [37] with permission from The Cambridge University Press).

$$H = \frac{P_{max}}{A}$$

Equation 2.7 Indentation hardness [37].

$$S = \beta \frac{2}{\sqrt{\pi}} E_{eff} \sqrt{A}$$

Equation 2.8 Indentation stiffness [37].

$$\frac{1}{E_{eff}} = \frac{1 - \nu^2}{E} + \frac{1 - \nu_i^2}{E_i}$$

Equation 2.9 Indentation elastic modulus [37].

Where H is the hardness, β is a geometric factor near unity, E_{eff} is the effective elastic modulus, E and ν are the elastic modulus and Poisson's ratio of the specimen, and E_i and ν_i are the elastic modulus and Poisson's ratio of the indenter tip.

A considerable amount of research has been devoted to the study of homogenous bulk materials that exhibit insignificant time-dependence since the appearance of the first commercial indentation apparatus. Advancements in system electronics and algorithms have led to the ability to study thin films, porous materials, time-dependence and much more. Naturally, these advancements are relatively new and therefore the least developed as opposed to those procedures developed for bulk homogeneous elastic-plastic material deformation. A brief overview of the current state of the field on pertinent topics for the materials tested in this study are reviewed below.

2.3.1 Porous Materials

The elastic response from porous materials are different from their bulk counterparts and follow a relation proposed by Gibson and Ashby [40]. The relation was first postulated to apply to nanoporous metals, but has since been extended to other nanoporous systems as well [41-44]. The relation is given in Equation 2.10.

$$\frac{E^*}{E_S} = C_1 \left(\frac{\rho^*}{\rho_S}\right)^2$$

Equation 2.10 The Gibson and Ashby relation [45].

Where E^* is the Young's modulus of the porous material, E_s is the Young's modulus of the dense material, ρ^* is the volume represented by the solid material (not counting voids), ρ_s is the volume of the total cell (solid and voids) and C_1 is a constant of proportionality.

Experimental data found in the literature for porous materials find the value of C_1 to be close to unity. As a result, it is often assumed to be 1.

There are difficulties that can complicate obtaining the true modulus and hardness of nanoporous films - like pile-up around the indenter tip, for example - but those are generally documented [46, 47]. It is well-known that densification directly below the indenter tip occurs and that this can influence the measured elastic response of the nanoindenter [46, 48]. The work by Vlassak et al. have shown, however, that the effect on the measured elastic modulus is small provided there is not a distinct difference in the mechanical behavior of the nanoporous material and the dense counterpart [46]. More specifically, when the modulus of the dense material (E_D) is greater than 3 times that of the porous material (E_P), as shown in Figure 2.13. The reason that densification plays a small role, given the conditions, are that it is limited to a relatively small region beneath the indenter tip and the region that deforms elastically is much larger than that. This is supported by the work of Briot et al. where nanoporous gold was indented and a FIB lift-out was done, shown in Figure 2.14. The nanoporous gold was indented at a maximum indentation depth of 2.5 μm and the densification field propagated to about 5 μm into the sample, or about twice the maximum indentation depth. The effect of densification in porous materials is something that leads to an overestimate of both the modulus and hardness and there is no current consensus on how to remove this effect.

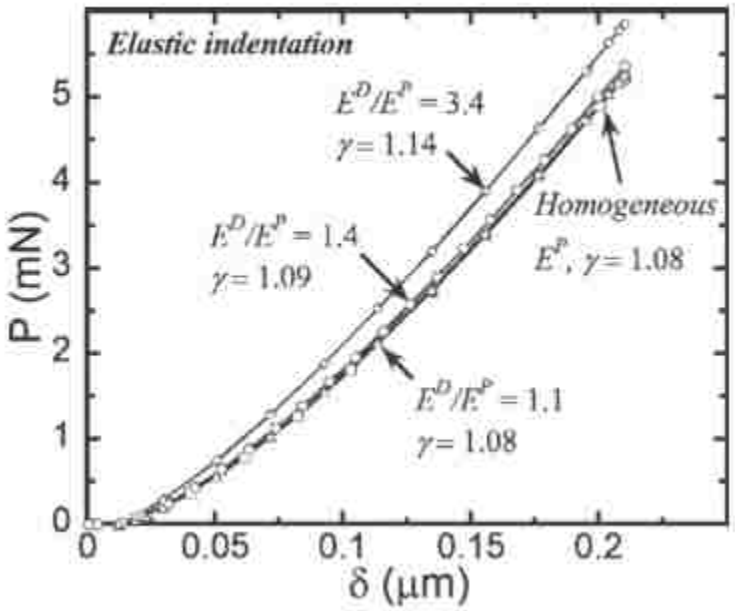

Figure 2.13 Finite element modeling results that show densification has a relatively small effect on elastic response, given some very general conditions are satisfied (Reproduced from [46] with permission from The Cambridge University Press).

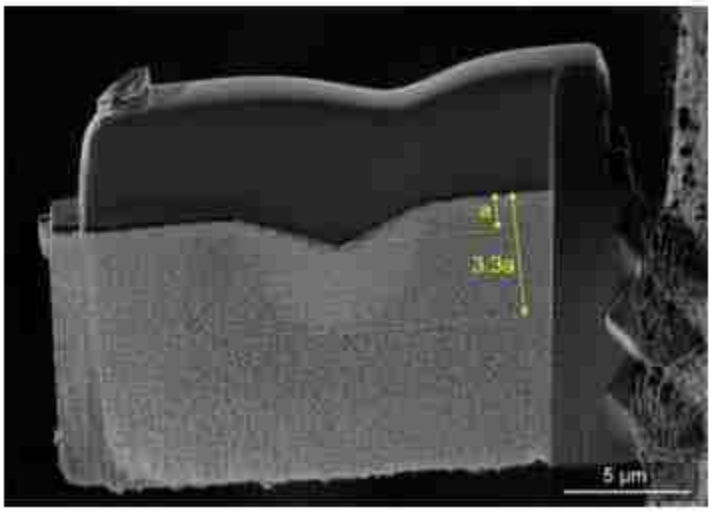

Figure 2.14 A cross-section SEM image at the center of an indent performed on nanoporous Au. The final depth after indentation was approximately 1.5 μm and the depth of the densification zone directly below the tip was about 3.3 times the final indentation depth (Reproduced from [48] with permission from The Cambridge University Press).

2.3.2 Thin Films

Nanoindentation is an attractive technique for probing small volumes of material because of its ability to accurately determine bulk mechanical behavior in confined spaces. The study of the mechanical behavior of films is a natural implementation because of its dimensions and wide variety of applications. There is an often quoted rule that the measurement of the film behavior must be performed at 10% of the film thickness of less [49]. Whether or not this generalization holds depends upon the relative mechanical behavior of the film-substrate system, the mechanical behavior of interest, as well as the geometry of the indenter used [36, 49-52].

The work by Hay et al. showed that the contact radius of the indenter, not the depth, was the most significant parameter for determining whether there was substrate influence. For Vickers and other self-similar geometries, the 10% rule applies but typically only for the elastic modulus and not the hardness [50, 52]. This is because the elastic field that propagates ahead of the indenter tip is much larger than the plastic field, under the same conditions [46]. Of course, this depends on the relative mechanical behavior of the film-substrate system. For example, indentation of a porous film on a silicon wafer (soft film on a hard substrate) can yield accurate results of hardness up to 50% of the film thickness [50]. This is portrayed in Figure 2.15.

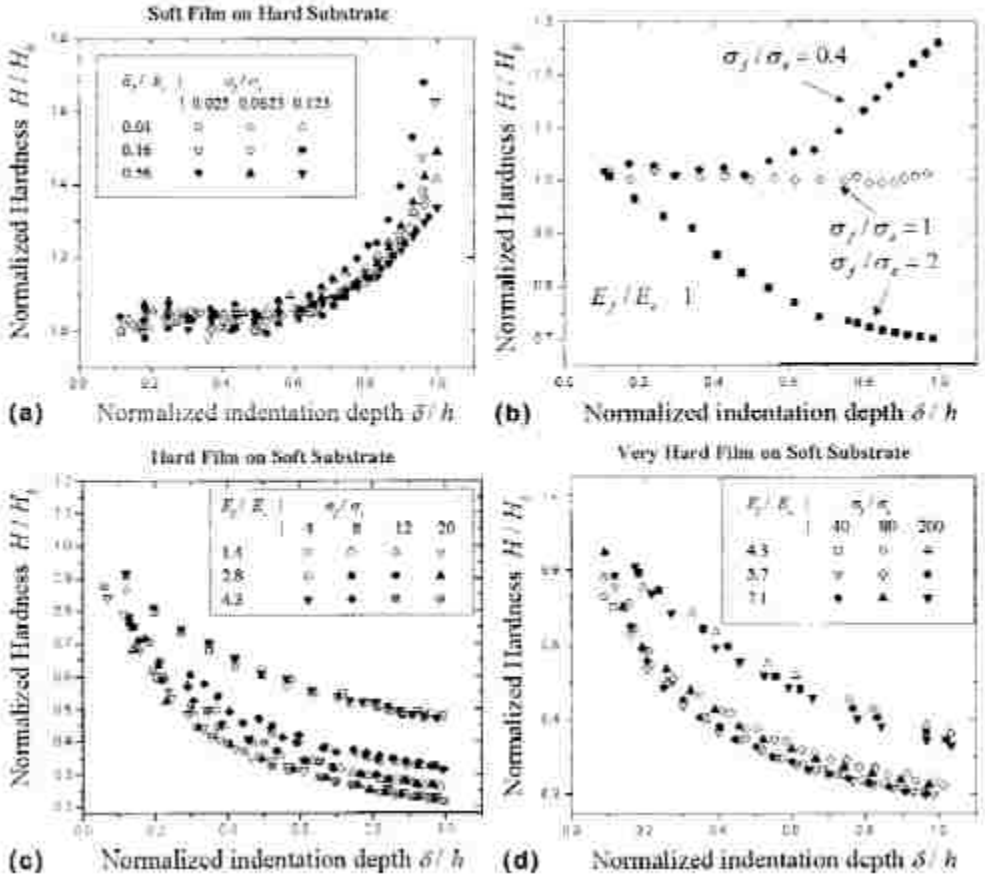

Figure 2.15 Exploring the substrate effects on different film-substrate systems through plots of the normalized film hardness (H/H_b) against the normalized indentation depth (δ/h) with relative constraints of E_f/E_s and σ_f/σ_s. (a) and (b) soft film-hard substrate, (c) hard film-soft substrate and (d) very hard film on soft substrate (Reproduced from [50] with permission from The Cambridge University Press).

2.3.3 Time-Dependent Materials

When a material is indented with a sharp tip, it is subject to elastic (reversible), plastic (instantaneously irreversible) and viscous (time-dependent irreversible) deformation [53]. Researchers have made great strides in understanding the complex relationships between structure/defects and mechanical behavior of materials that exhibit an elastic-plastic response similar to that observed in Figure 2.12. Advancements in system electronics and algorithms have helped in the testing of time-dependent materials, but the

field is still in its infancy. An outline of state-of-the-art procedures to study time-dependence is given below.

The quantification of the viscous component of deformation can be performed in either the time or the frequency domain. One domain is not inherently better than the other, but each has their own advantages and disadvantages.

Time Domain: There are three basic stages to experiments carried out in the time domain: a loading segment, a hold segment and an unloading segment [54]. The load, time and displacement data gathered from these basic stages can be used to determine the creep compliance, *D(t)*, or the stress relaxation modulus, *E(t)* [54]. The creep compliance and the stress relaxation modulus are highly dependent on the indenter geometry. Simple solutions exist for the flat punch, and more complex solutions for spherical and pyramidal geometries [55, 56]. These techniques are also subject to thermal drift and transient effects that could significantly influence the gathered data, but do not require a known contact area.

Frequency Domain: Experiments performed in the frequency domain typically utilize a phase-lock amplifier (PLA) that measures the material response to a harmonic oscillation of the indenter tip at a fixed frequency. The ultimate goal is to determine the in-phase and out-of-phase components that correspond to the elastic and damping behavior of the material, respectively. In this way, a key metric used to characterize the amount of energy a material can dissipate – the loss factor ($tan\ \delta$) – can be quantified. The limits of the loss factor are between $0° \leq \delta \leq 90°$, which represent purely elastic and viscous deformation, respectively [57]. Operating in the frequency domain requires expensive electronics and a well-behaved system. However, the stiffness and damping measurements are not subject to thermal drift and there is no need to assume any parametric model.

Ultimately, the time-dependent materials of interest were characterized in the frequency domain because it best made use of the state-of-the-art nanoindenter and required the fewest assumptions about the material.

Experiments in the frequency domain are typically performed using one of two load-time histories [54]: In the first, the dynamic response is measured as the indenter is continuously loaded to a prescribed load/depth. In the second, the material's dynamic response is measured while the load or displacement is held at a constant, predetermined value. The second load-time history is preferred because it is better suited for achieving steady-state harmonic motion and has undergone rigorous experimental verification [55, 58].

As previously mentioned, the accurate characterization of the loss factor requires a well-behaved or well-characterized system. This means that spurious data may be caused by two issues: (i) an additional phase shift from the system electronics or physical damping in the load frame and (ii) not being able to achieve steady-state harmonic motion over the time scale in which the phase angle measurement was performed [57]. While the instrument's contribution to the loss factor is always present, it can effectively dominate the measured response under some very general guidelines outlined in Equation 2.11 and Equation 2.12 [57].

$$\left.\frac{f_0}{h_0}\right|_{coupled} \gg \left.\frac{f_0}{h_0}\right|_{free\ space}$$

Equation 2.11 Inequality showing when the specimen dominates the measured phase angle response, not the actuator [57].

$$K_{lf} \gg K_{contact}$$

Equation 2.12 Inequality showing when the damping of the load frame is insignificant compared to that of the specimen [57].

where $f_0/h_0|_{coupled}$ is the apparent power of the actuator and specimen, $f_0/h_0|_{free\ space}$ is the apparent power of the actuator hanging in free space, K_{lf} is the stiffness of the load frame, and $K_{contact}$ is the stiffness of the contact. It is not possible to define absolute values that those equations must exceed because they depend on numerous complex factors. In general, the magnitude of these inequalities must increase with the resolution of phase angle and/or the phase angle of the specimen approaches zero [57]. Relative magnitudes for these inequalities are provided in Table 2.3 for common linear elastic and viscoelastic materials. Given the magnitude of the inequalities, it can be concluded that the specimen and not the test system dominate the measured response. By using Equation 2.13 - Equation 2.15, one can correct for any additional phase shift caused by the system electronics [57, 58].

Table 2.3 Relative magnitudes to the inequalities in Equation 2.11 and Equation 2.12 for common materials obtained at an operating frequency of 48 Hz [57].

	Fused Silica	PC	PMMA
$\frac{\left.\frac{f_0}{h_0}\right\|_{coupled}}{\left.\frac{f_0}{h_0}\right\|_{free\ space}}$	430	28	48
$\frac{K_{lf}}{K_{contact}}$	10	165	96

$$\delta_{corrected} = \tan^{-1}\left(\frac{C_{contact}\omega}{K_{contact} - m\omega^2}\right)$$

Equation 2.13 The corrected phase angle the subtracts the contributions from the instrument's actuator and physical damping from the load frame [57].

$$C_{contact}\omega = \frac{f_0}{h_0} sin\delta\Big|_{coupled} - \frac{f_0}{h_0} sin\delta\Big|_{free\ space}$$

Equation 2.14 The out-of-phase component of the imposed harmonic oscillation [57].

$$K_{contact} - m\omega^2 = \left[\frac{1}{\frac{f_0}{h_0} cos\delta\Big|_{coupled} - \frac{f_0}{h_0} cos\delta\Big|_{free\ space}} - \frac{1}{K_{lf}}\right]^{-1}$$

Equation 2.15 The in-phase component of the imposed harmonic oscillation [57].

where $\delta_{corrected}$ is the phase angle of the specimen, $K_{contact} - m\omega^2$ is the in-phase (elastic) component and $C_{contact}\omega$ is the out-of-phase (damping) component of the imposed harmonic oscillation. This summarizes the corrections and conditions required to mitigate issues outlined in (i).

There are also two methods that can be used to ensure the coupled system-specimen have reached steady-state harmonic motion to mitigate issues outlined in (ii). The first method is to wait for the time-dependent mechanisms of the specimen to exhaust themselves and the second is to operate the PLA at high frequencies such that the change in contact area is insignificant over the time scale in which the phase angle is measured [57]. The best metric to ensure that the specimen-system have reached steady-state is its stability over time [57].

Pile-up: The Oliver-Pharr method for nanoindentation relies on accurate measurement of the contact area, as summarized in Equation 2.7 and Equation 2.8. The trouble with determining the mechanical response of materials that exhibit time-dependence is that they tend to pile-up around the indenter tip, as shown in Figure 2.16 [50]. This leads to an underestimation of the contact area, consequently overestimating both the hardness and modulus. While there have been studies that attempt to deal with pile-up, the amount of pile-up differs for different material systems and can depend on the amount of work-hardening [37, 59-61]. There does exist a simple, experimental parameter that can be useful in determining if the amount of pile-up during indentation was significant [59]. This parameter is the ratio of the final indentation depth to the maximum indentation depth, h_f/h_{max}. Of course, this parameter relies on the indenter geometry being self-similar such that it is not dependent on depth. The limits of this parameter are between 0 and 1, where the lower limit represents fully elastic deformation and the upper fully plastic deformation. If the h_f/h_{max} ratio is less than 0.7, then pile-up around the indenter can safely be ignored. However, if the ratio is larger than 0.7, pile-up will depend on the work-hardening behavior of the material.

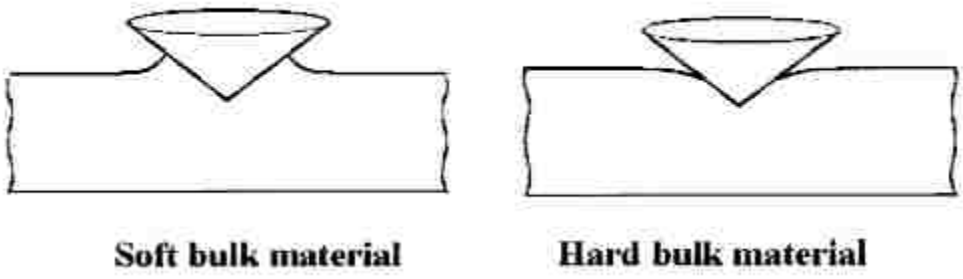

Figure 2.16 Schematic representing the difference between significant pile-up (left) and insignificant pile-up (right) around the indenter tip (Reproduced from [50] with permission from The Cambridge University Press).

2.4 Thermionic Dispenser Cathodes

Thermionic dispenser cathodes are a specific example of an application of porous materials that are used in vacuum electron devices (VEDs) as electron emitters for use in a variety of applications including cathode ray tubes, travelling wave tubes, and klystrons. Modern dispenser cathodes are composed of a porous metallic refractory metal – typically tungsten - that has been impregnated with barium oxide, calcium oxide and aluminate [62]. This is known as the "B" type cathode and is shown schematically in Figure 2.17.

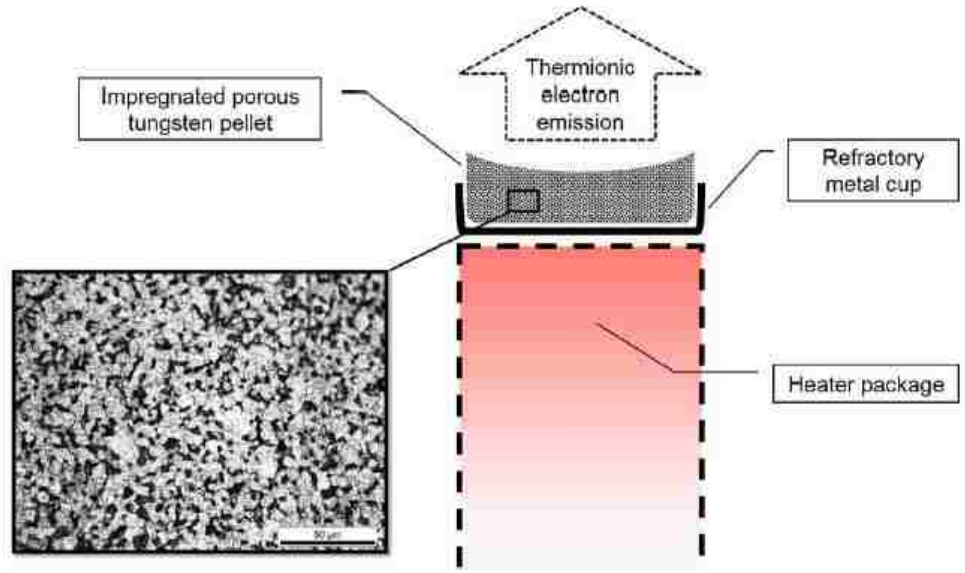

Figure 2.17 A schematic showing the components of a B-type cathode [63].

It is widely accepted that barium plays a key role in the lowering of the surface work function such that electrons can escape more easily from the cathode [64, 65]. The incorporation of calcium is thought to reduce the rate at which barium sublimates from the surface, which enhances the emission properties [66]. The predecessors to this cathode include the oxide cathode, the "L" cathode and the pressed/sintered cathode [62].

Following the development of the “B” type cathode, came the “M” type cathode and the scandate cathode [62]. The “M” type cathode was an interesting development because it consisted of the “B” type cathode coated with a material of high work function, including osmium, iridium, and ruthenium. It is completely counter-intuitive that the high work function coating acts to lower the overall work function of the material surface, but nevertheless it does. The most recent development is the scandate cathode, which has been shown to achieve higher current densities at lower temperatures than previous generations of cathodes [67-72]. This is desirable due to the high current density demands driven by applications and the lower temperature improves cathode longevity. While the traits of this cathode system are desirable, there are still issues associated with their development including uneven emission, low reproducibility, and unknown emission mechanisms.

2.4.1 Thermionic Emission

The concept of thermionic emission is relatively simple: heat up something (typically a metal) until there is a flow of charge (typically electrons) from the heated object to the vacuum level. Generally, the electrons must overcome a surface potential energy barrier that is best described as the work function. In the absence of heating there are no electrons in the Fermi distribution tail above the Fermi level. However, as the temperature increases, this causes electrons to fill in the Fermi distribution tail, which is depicted as the blue solid area in Figure 2.18. The British physicist Owen Richardson developed a mathematical formulation (shown in Equation 2.16) that described thermionic emission from hot bodies for which he was awarded the Nobel Prize in Physics in 1928.

$$J = AT^2 \exp\left(\frac{-\Phi}{k_B T}\right)$$

Equation 2.16 The Richardson-Dushman equation [73-75].

Where J is the current density, A is a constant known as the "Richardson constant", T is temperature, Φ is the electron work function and k_B is the Boltzmann constant.

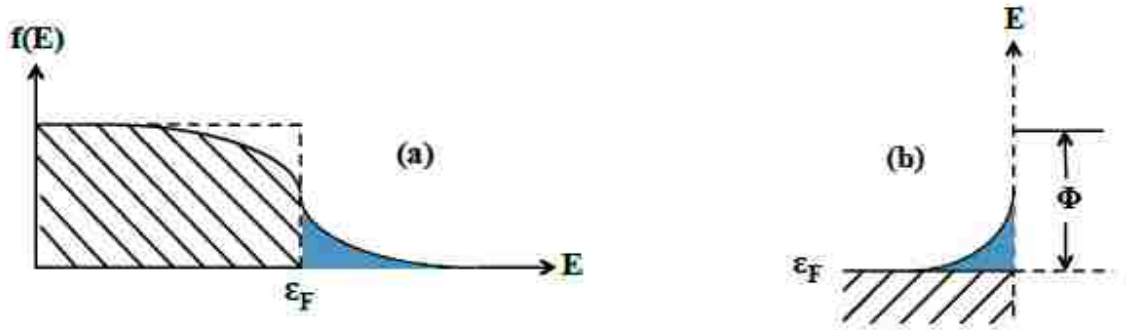

Figure 2.18 a) The area enclosed in the dotted lines represents the Fermi distribution of electrons with heating and b) shows the electron distribution (in blue) above the Fermi level while heating, where Φ is the distance between the Fermi level and the vacuum level – also referred to as the work function [76].

2.4.2 The Schottky Effect

Typically electron emission is enhanced by the application of an electric field between the hot body and an anode some distance away. This enhancement is used in electron guns to help lower the surface energy barrier impeding electron escape. Figure 2.19 shows how the Schottky effect can influence the effective work function of a material when heating. A mathematical formulation of how the Schottky effect can influence the work function is shown in Equation 2.17.

$$\Delta\Phi = e * E * z_m = \sqrt{\frac{e^3 E}{4\pi\varepsilon_0}}$$

Equation 2.17 The Schottky effect.

Where *e* is the charge of an electron, *E* is the electric field, z_m is the distance between the anode and cathode, and ε_0 is the permittivity of free space.

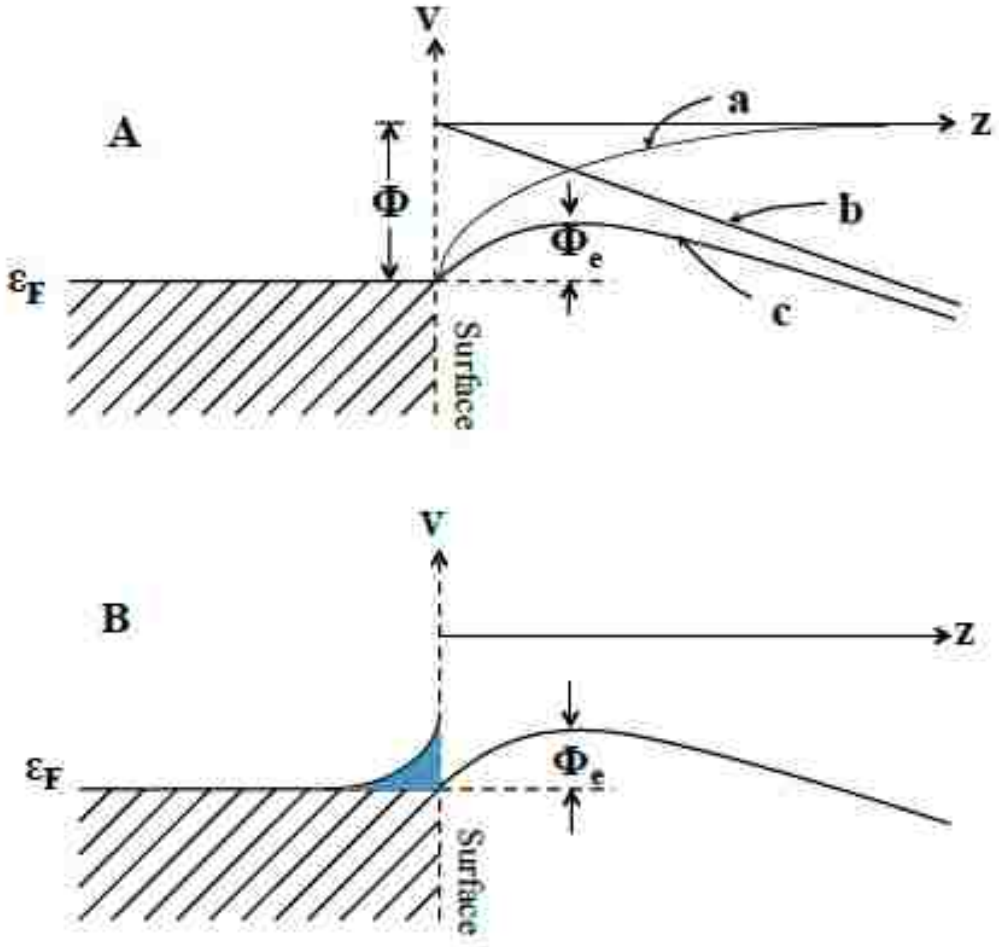

Figure 2.19 Diagram A shows how the work function is affected in a) the absence of an electric field, b) in the presence of an electric field and c) is the effective work function when an electric field is applied. Diagram B shows the electron distribution in blue in the presence of an electric field [76].

3 Experimental Methods

This section is devoted to the experimental methods and machines used throughout this dissertation and gives a brief overview of the various techniques. It is beyond the scope of this dissertation to provide a comprehensive detail on the methods used to characterize or fabricate the materials of interest and suggested reading is provided in the text.

3.1 Physical Vapor Deposition and Film Growth

Magnetron sputtering is a type of physical vapor deposition whereby atoms of a target material are ejected through bombardment of argon atoms [77]. A simplified schematic of this process is shown in Figure 3.1 [78]. The system consists of an anode (substrate) and cathode (target) opposite one another. The magnet array behind the target material allow for a higher plasma density to be created near the cathode, such that deposition is more rapid once a backing potential is applied (DC or RF). Typically, the deposition occurs under vacuum to increase the mean-free path of ejected target material, but with a significant partial pressure of argon, which acts to eject target material through bombardment. By changing the partial pressure of argon, substrate biasing, substrate temperature, deposition rate and other deposition conditions, one can change the film properties like structure, density, residual stress and others [79].

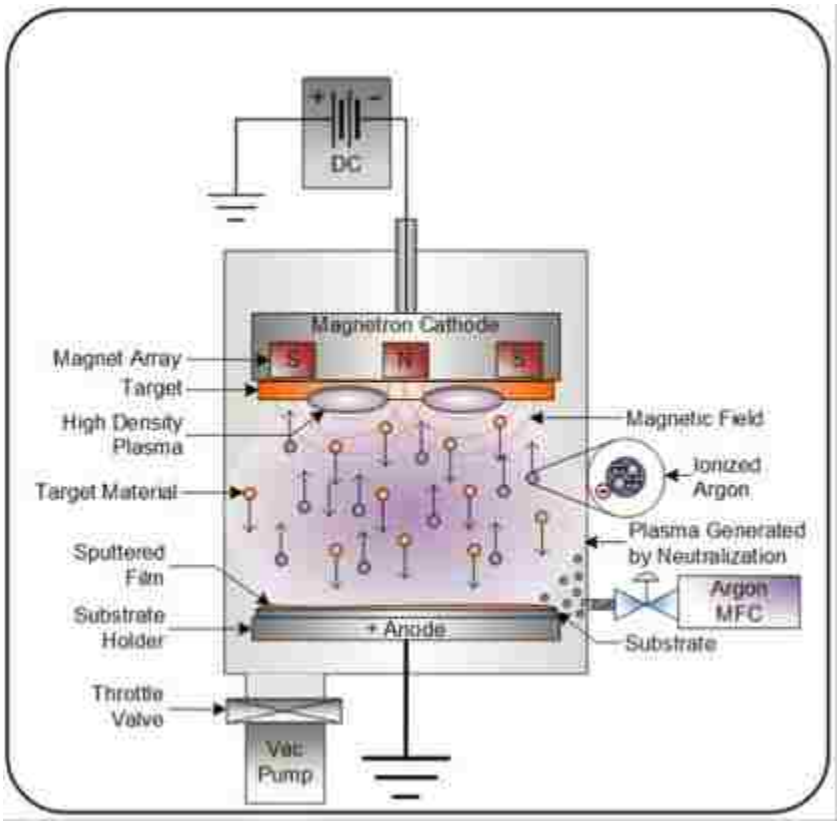

Figure 3.1 A schematic showing the mechanism of magnetron sputtering [78].

Throughout this dissertation magnetron sputtering was used to deposit films of Si-Mg, W and W-Al alloy films. Of course, the deposition conditions for each study varied slightly but the general outline of deposition parameters used is given below. Deposition was carried out inside an ATC ORION system (AJA International, Inc.) using either DC or RF power supplies. Typically, an RF supply was used for silicon due to its semiconducting nature, while a DC supply was used for metals. The base pressure of the system prior to sample loading was below 10^{-6} torr. Single crystal (001) substrates of silicon were used for deposition because of their low surface roughness. Immediately before deposition, the substrate was cleaned via substrate biasing to remove any contaminants and promote film adhesion. Interlayers of material were used to promote film adhesion. More details about the parameters used will be given in the subsequent chapters

for the film of interest. Additional reading on the technique of magnetron sputtering and the factors that influence film structure can be found elsewhere [80-83].

3.2 Dealloying

Free corrosion dealloying was used to create all the nanoporous silicon shown in this dissertation. A variety of etchants were used to etch magnesium from the silicon-magnesium precursor films and those included: distilled water, deionized water, ethanol, methanol, and isopropanol. Sometimes a final rinse in dilute acetic acid (commercial vinegar) allowed the surface oxide layer to lift off revealing an interesting structure beneath. Free corrosion dealloying using the above etchants was attempted at a variety of temperatures as well, but typically between room temperature and the freezing point of water. Preliminary experiments were performed in an ice bath, which showed promising results. However, due to the unreliable nature of the temperature stability, a water chiller was used to ensure temperature uniformity over the duration of the experiment(s). Typically, dealloying was carried out by filling glass vials with a volume of 30 mL and placing the capped vials inside the water chiller chamber for the free corrosion dealloying to take place. Since the optimum dealloying composition had to be investigated alongside the best dealloying solution, gradient samples were typically dealloyed to find the best etchant-parting limit. Typically, the parting limit hovered around 54 at.% silicon.

3.3 Characterization

Central to the ideal of understanding why any given material behaves as it does under user-defined conditions is characterization. It allows the user to observe or quantify certain qualities of a material that could be paramount to understanding intrinsic material

properties. This section describes the techniques used during the completion of this dissertation.

3.3.1 Electron Microscopy

Scanning Electron Microscopy: This is a particular type of microscopy that is virtually ubiquitous in research. A scanning electron microscope (SEM) is used in place of optical microscopy because it allows the user to detect features on the nanometer scale - depending on the type of microscope being used – and has a relatively low associated cost. Additionally, the depth of field is quite large and can give images a 3D appearance (tens of μm at 1,000x magnification or μm at 10,000x magnification) [84].

The basic principle of an SEM is reasonably simple – extract electrons from an electron gun, focus them onto the sample surface and collect secondary electrons. To reiterate, the most important attributes of an SEM are resolution and depth of field, given in Equation 3.1 and Equation 3.2.

$$d_p = \left(\frac{4i_p}{\beta\pi^2\alpha_f^2}\right)^{\frac{1}{2}}$$

Equation 3.1 Probe diameter for an SEM [84].

$$D_f = \frac{2R}{\tan\alpha}$$

Equation 3.2 Depth of field for an SEM [84].

Where d_p is the probe diameter, i_p is the probe current, β is the beam brightness, α_f is the convergence angle of the probe, R is resolution and α is the convergence angle of the objective aperture. In order to maximize resolution, the user wants to minimize the probe diameter, but there is a trade-off between depth of field and resolution.

When the electron beam strikes the surface of the sample, there is an interaction volume below the sample surface where different types of electrons are generated, shown in Figure 3.2 [84]. The Monte Carlo simulation in Figure 3.2 a) shows the electron trajectory after impacting the sample and in Figure 3.2 b) there are characteristic electrons that escape from different zones of the volume. The characteristic electrons are collected to obtain information unique to the volume from which they were ejected. An SEM typically collects secondary electrons, which emit from the top 5-50 nm of the sample surface. Generally, the more energetic electrons escape from deeper in the sample. This interaction volume will be revisited shortly in the following sections.

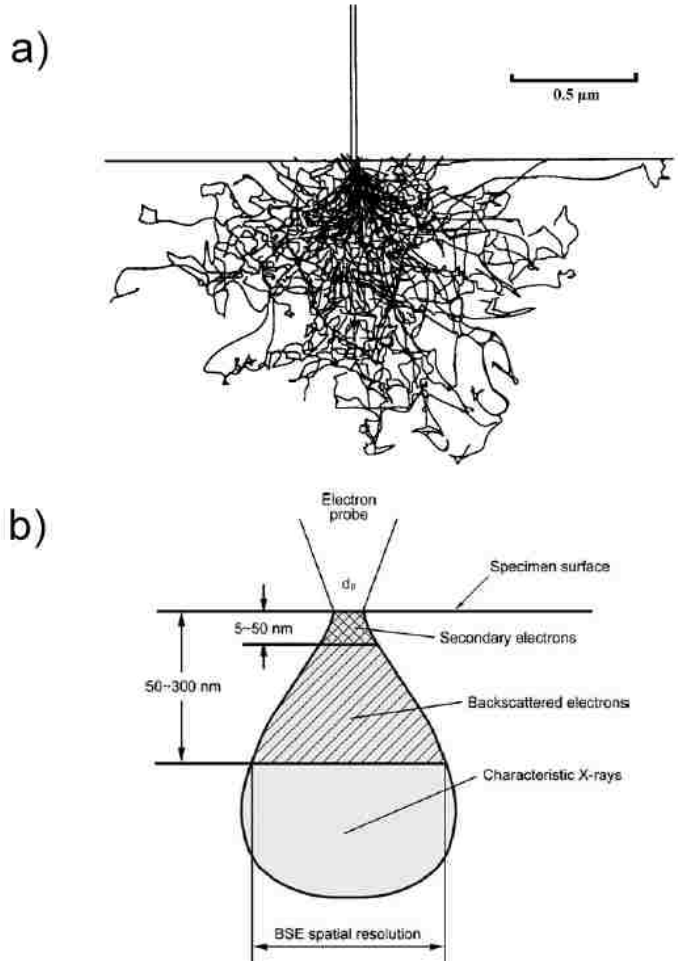

Figure 3.2 a) Monte Carlo simulation of and electron beam-sample interaction (acceleration potential = 20keV) and b) a schematic depicting depths at which characteristic electrons are generated within the interaction volume (Reproduced from [84] with permission from Wiley Books).

There were five SEMs used throughout this work: a FEI Helios Nanolab, FEI Quanta 250, Hitachi S-4300, Zeiss EVO MA10, and a Hitachi S-900.

Transmission Electron Microscopy: In many ways, the transmission electron microscope (TEM) is similar to the SEM in that they both have: an electron source, electromagnetic lenses for focusing, a sample stage and detectors for collecting signal. The TEM, however, typically uses a much higher accelerating voltage for the electron beam for two reasons: the associated wavelength of individual electrons is much smaller and it

allows them to pass through the sample [85]. A typical accelerating voltage for the TEM is 200 kV and allows the user to achieve higher resolution in accordance with Equation 3.3.

$$R = \frac{0.61\lambda}{\mu \sin \alpha}$$

Equation 3.3 Resolution equation [86].

Where λ is the wavelength, μ is the refractive index of the medium between the sample and objective lens, and α is the half-angle of the cone entering the objective lens [86].

Besides imaging, the user can also get crystal structure information about the sample through electron diffraction. In the same way that x-rays are diffracted by crystal planes in XRD, electrons can be diffracted and Bragg's Law still applies. The diffraction angle in TEM is small ($\leq 1°$) and the diffracted beam from a crystal plane (hkl) appears as a bright spot on the back focal plane of the objective lens [85]. If the beam is parallel to a crystallographic axis, the beam will diffract and form a pattern in reciprocal space that can be indexed and interpreted [85]. Further reading on obtaining diffraction patterns in the TEM can be obtained elsewhere [85, 87].

In order for the sample to be electron transparent, the thickness must be less than 100 nm and is often times thinner for material with a high atomic number [85]. This is typically the most difficult step in TEM examination. The specimens in this dissertation that were examined via TEM were extracted using a focused-ion beam (FIB) lift-out process that is shown schematically in Figure 3.3. First, a protective pad of Pt is deposited on the sample surface to protect the sample from FIB damage, then two trenches are milled, as shown in Figure 3.3 a). Then a J-cut is performed to free most of the TEM sample from

the specimen, shown by the yellow rectangles in Figure 3.3 a) that resemble the letter J. Then a manipulation rod (tungsten in this case) is welded to the sample surface/Pt protective layer, as shown in Figure 3.3 b). Then the rest of the TEM sample is cut free from the specimen, as shown in Figure 3.3 c) by the orange rectangle. The free specimen shown in Figure 3.3 d) can then be thinned via FIB milling and attached to a TEM grid of your choice for further investigation. An in-depth review of this process is given elsewhere [88, 89]. This expedites the process of thinning and is more precise than previous methods that involved a combination of mechanical and electrolytic means [85].

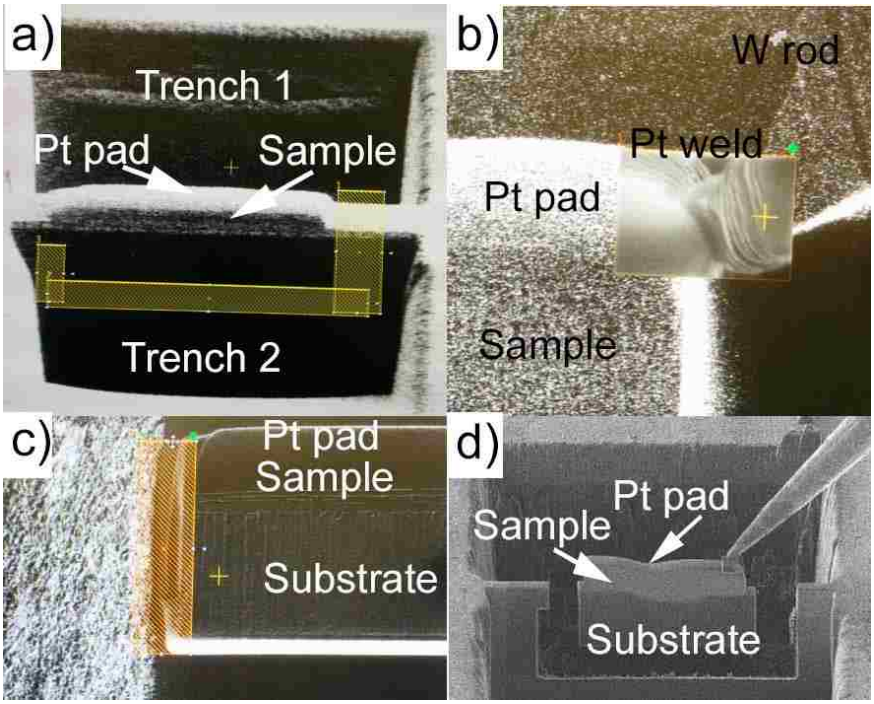

Figure 3.3 An illustration of the FIB lift-out process for a sample that will be observed in TEM. In a) a protective Pt pad is deposited to protect the sample from FIB damage, trenches are milled out in front of and behind the sample, and a J-cut is performed. In b) the manipulation rod is attached to the sample. In c) the sample is milled free from the larger specimen and d) shows the free sample ready for thinning.

3.3.2 Elemental Analysis

As a consequence of bombarding a sample surface with electrons for imaging purposes in a SEM, there are also characteristic x-rays that are emitted from the sample. After striking an atom with the electron beam of sufficient energy, a core-shell electron is liberated. This puts the atoms in a metastable state, which is quickly filled by an outer shell electron. Since energy must be conserved during this process, a characteristic X-ray is produced that is equal to the difference between the shell migration. A schematic of this process is shown in Figure 3.4. The characteristic X-ray that is emitted can be collected with a Si(Li) detector that generates electron-hole pairs to determine the energy of the incident x-ray [90]. This is known as energy dispersive spectroscopy (EDS) and was the method largely used throughout this dissertation to study sample composition. There is, however, another method that can be used to obtain sample composition that uses a single crystal to diffract and separate characteristic x-rays based on wavelength. This is known as wavelength dispersive spectroscopy (WDS), but was not used to study sample composition in this dissertation. The element from which the characteristic x-ray was emitted can be determined using Moseley's Law, shown in Equation 3.4 [90].

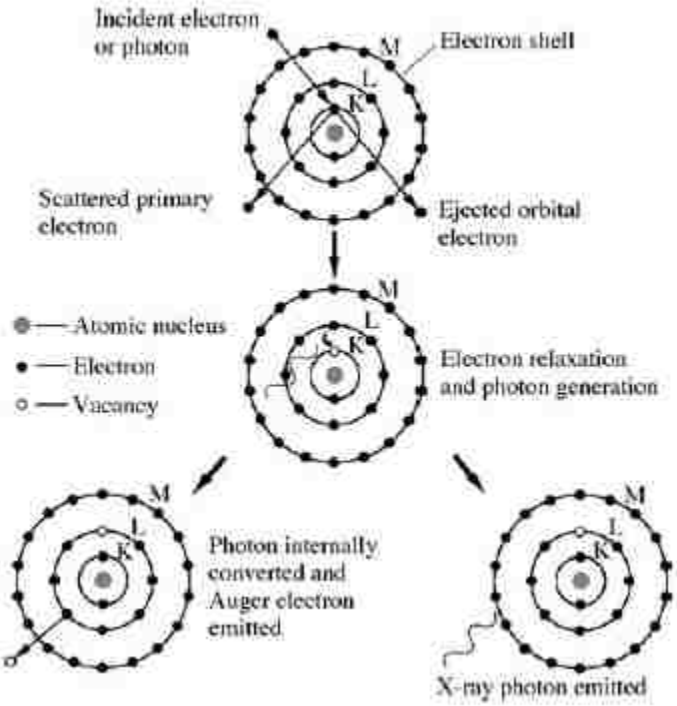

Figure 3.4 Schematic of the characteristic X-ray generation process after electron bombardment of an atom (Reproduced from [90] with permission from Wiley Books).

$$\lambda = \frac{B}{(Z-\sigma)^2}$$

Equation 3.4 Moseley's Law [90].

Where λ is the wavelength of the characteristic X-ray, B and σ are constants that depend on specific shells and Z is elemental atomic number [90]. In this work, a Bruker XFlash 5010 EDS detector attached to a Zeiss EVO MA10 SEM,

3.3.3 X-Ray Diffraction

X-ray diffraction (XRD) is a technique that is largely used to study the crystal structure of a given material. It is a relatively cheap and efficient method to identify the way in which atoms are arranged in thin films, bulk sample or even powders. It was

discovered in 1912 and has become an indispensable tool that virtually all laboratories utilize [91].

Naturally, XRD utilizes x-rays that are generated when high-speed electrons collide with a metallic target. Typically the metal target is made of copper. The wavelength of the x-ray generated in this manner can be calculated using Equation 3.5, where λ is the wavelength, V is the accelerating voltage of the electrons being collided, h is Planck's constant and e is the charge of an electron. Often times the radiation used for diffraction will be refered to as Cu Kα. The Kα wavelength is used because it has the highest intensity for the appropriate range of wavelength and the rest is filtered out.

$$\lambda = \frac{h}{eV}$$

Equation 3.5 The wavelength of radiation produced when electrons collide with a metal target [91].

The fundamental relation that governs the way in which x-rays diffract from crystal planes is given in Equation 3.6, where λ is the wavelength of the incident x-ray, d is the lattice spacing between parallel planes, and θ is the angle of incidence. The idea described by Equation 3.6 is the notion of constructive interference between incident x-rays. When there is not constructive interference, there is destructive interference and diffraction does not occur.

$$n\lambda = 2dsin\theta$$

Equation 3.6 Bragg's Law of diffraction [91].

3.3.4 Nanoindentation

A more comprehensive review of the nanoindentation techniques employed are given in section 2.3 in the background. This was done because the understanding of thin film mechanical behavior comprises a large portion of this dissertation. Here, a description of the nanoindenter used to study the mechanical behavior is given along with some specimen preparation techniques.

The nanoindenter used to characterize the mechanical behavior of the thin films in this study was equipped with an iMicro load frame and an iNano actuator (Nanomechanics). The large stiffness associated with the iMicro load frame in combination with the high sensitivity of the iNano actuator offers better sensitivity at small contact areas. The indenter sits atop a table that is isolated from vibration, which further increases accuracy at small depths.

The samples of interest are typically mounted atop the aluminum pucks via crystalbond, shown in Figure 3.5, which requires heat. A low temperature crystalbond was used that melts at approximately 50°C to ensure the samples are not oxidized during the mounting process. It is advised to not use superglue on nanoporous samples because they tend to absorb the glue before it sets and contaminate the mechanical response of the material of interest. I learned that the hard way. Once the aluminum pucks have cooled to room temperature after mounting, you may then insert the aluminum pucks into the sample tray, shown in Figure 3.6 a). The aluminum/sample cannot be placed in the sample tray willy-nilly. A procedure must be used such that the surface of the sample is approximately in the plane of indentation, as shown in.Figure 3.6 b). I find it easy to use a simple optical alignment, where you ensure the height of your sample(s) are at the same height as the

posts around the perimeter of the sample tray. Once this is accomplished, you may insert the sample tray into the nanoindenter and proceed to setup your mechanical test.

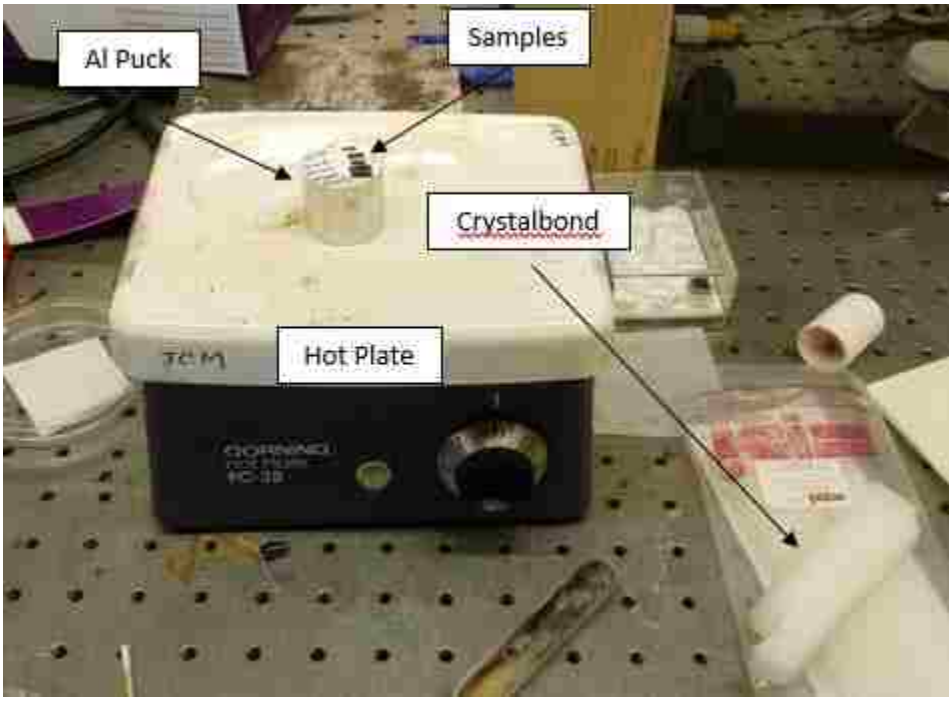

Figure 3.5 The method of mounting samples to the aluminum puck for nanoindentation.

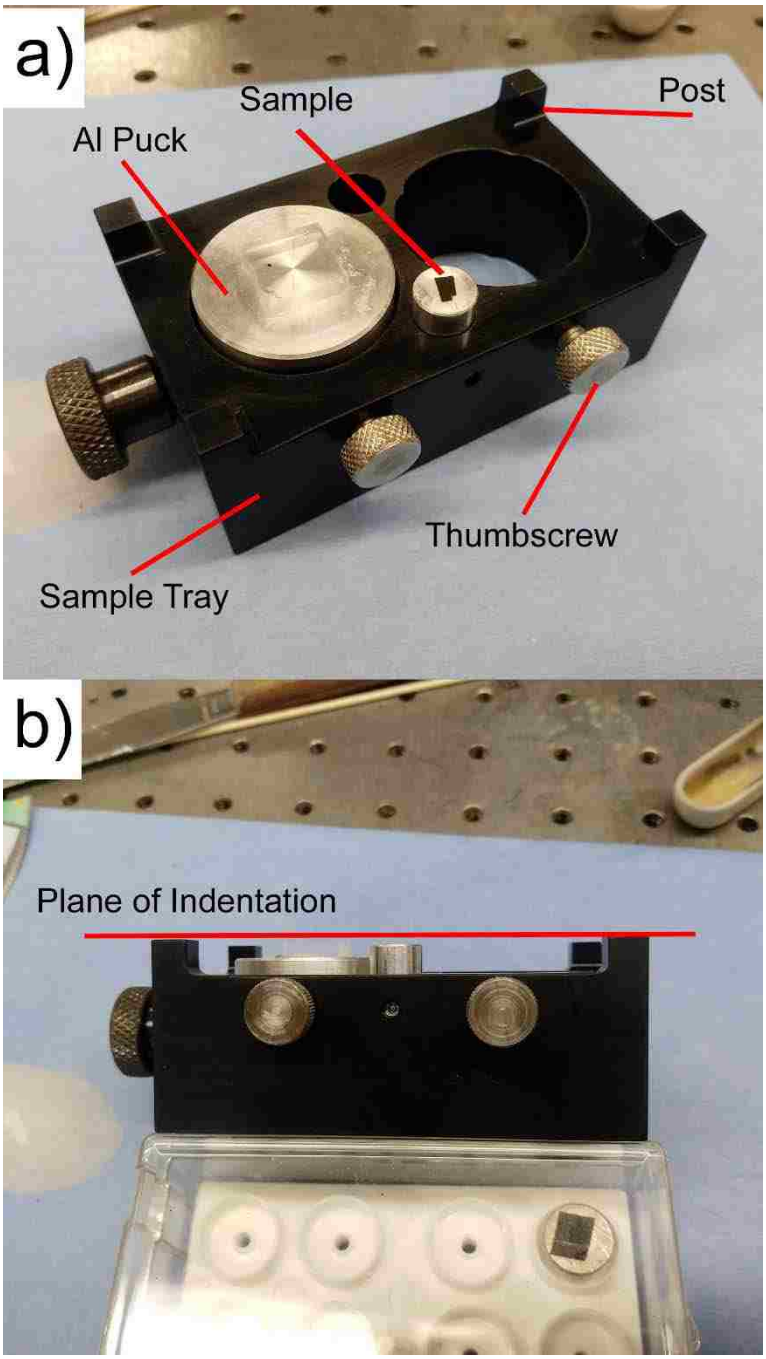

Figure 3.6 a) is the sample tray and labeled components and b) is an example of the optical method of alignment such that the surface of the sample(s) are approximately in the plane of indentation.

3.3.5 Electron Spectroscopy for Surface Analysis

This technique uses characteristic electrons emitted after liberation via the photoelectric effect for surface analysis. There are two types of electron spectroscopy: auger electron spectroscopy (AES) and x-ray photoelectron spectroscopy (XPS). A Thermo Scientific K-alpha XPS, shown in Figure 3.7, was used throughout this dissertation to study material surfaces. It is equipped with an Al Kα source for x-ray generation, ion gun for milling, and an electron flood gun for charge compensation.

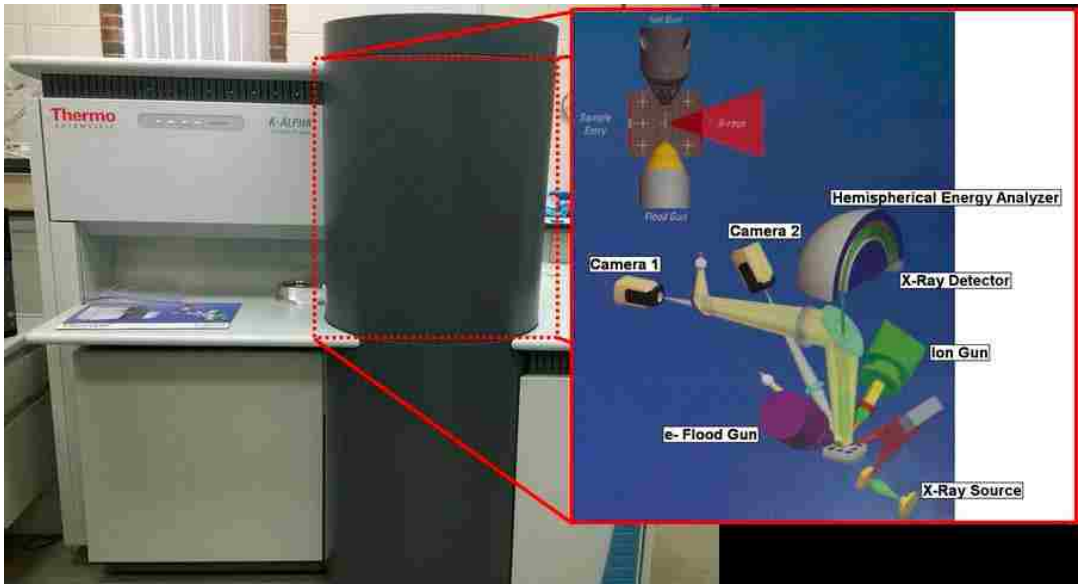

Figure 3.7 The XPS system used to study sample surfaces and an insert showing the various components of the spectrometer.

XPS uses low energy photons to liberate electron from the near-surface of the sample (10 nm or less), shown in Figure 3.8 [92]. When an incident photon has sufficient energy (hv) to liberate an inner shell electron, it is ejected with a kinetic energy, E_K. By knowing the kinetic energy of the liberated electron, one can calculate the binding energy of the photoelectron, E_B, through Equation 3.7 [92].

$$E_B = h\nu - E_K - \phi$$

Equation 3.7 XPS binding energy equation [92].

Where φ is the work function, h is Planck's constant and ν is the frequency. The binding energies of elements have characteristic values, but have the added advantage that shifts in binding energy can relay information about the chemical state of the element of interest. In general, a withdrawal of valence electron charge will increase the binding energy and addition of valence electron charge will decrease the binding energy [92].

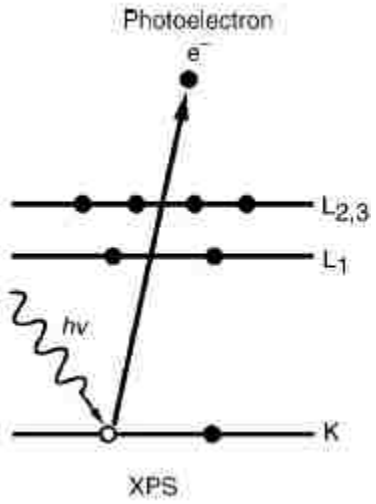

Figure 3.8 The emission of a 1s photoelectron using XPS (Reproduced from [92] with permission from Wiley Books).

3.4 The Cathode Characterization Chamber

The cathode characterization chamber, affectionately referred to as C^3, is a unique system that was designed as a group effort and that I assembled. An image of the entire system is shown in Figure 3.9. A schematic of the main vacuum chamber can be found in Appendix B. C^3 is equipped with a Kelvin probe, a residual gas analyzer, two photoemission systems and a heating stage. The main chamber is pumped with an ion

pump, but a turbo pump backed by a rotary vane pump pumps the load lock for sample transfer. The heating stage is affixed to an xyz manual manipulation stage for optimum sample positioning. A schematic of the system is shown in Figure 3.10.

Figure 3.9 The cathode characterization chamber and associated electronics.

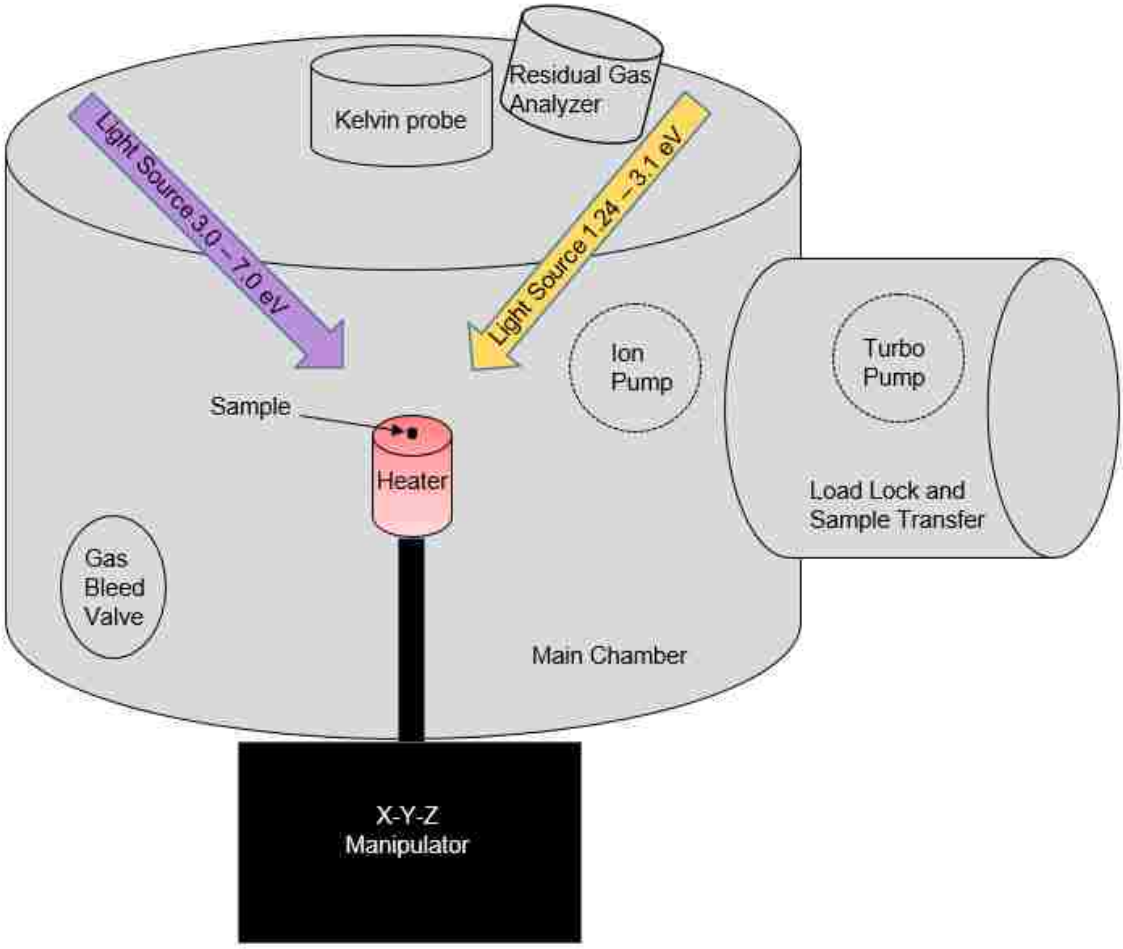

Figure 3.10 A schematic of the cathode characterization chamber and capabilities.

3.4.1 Heating Capabilities

The first iteration of a heating stage (button heater) was actually a placeholder for a heating stage that was to be delivered from Thermic Edge because they had major setbacks in the design of the original heating stage functionality. The button heater is shown in Figure 3.11 a) heating a cathode pellet. A carrier made of stainless steel was fashioned to hold the cathode pellet during heating with the button heater. The final design of the heating stage was done in collaboration with 3M Ceradyne, Inc., shown in Figure 3.11 b). The heating stage sled was designed to accommodate 6 cylindrical samples with a diameter of ~3 mm and a height $\geq$ 2 mm. The heating is performed by running a high current through

a tungsten-rhenium wire that has been surrounded by alumina potting inside the heater body. The high current is supplied to the heater through a UHV electrical feedthrough flange such that the current is isolated from the vacuum chamber – a necessary condition for taking contact potential difference measurements while heating. The samples, however, are in electrical contact with the vacuum chamber, and this is connected to ground via the Kelvin probe DCU.

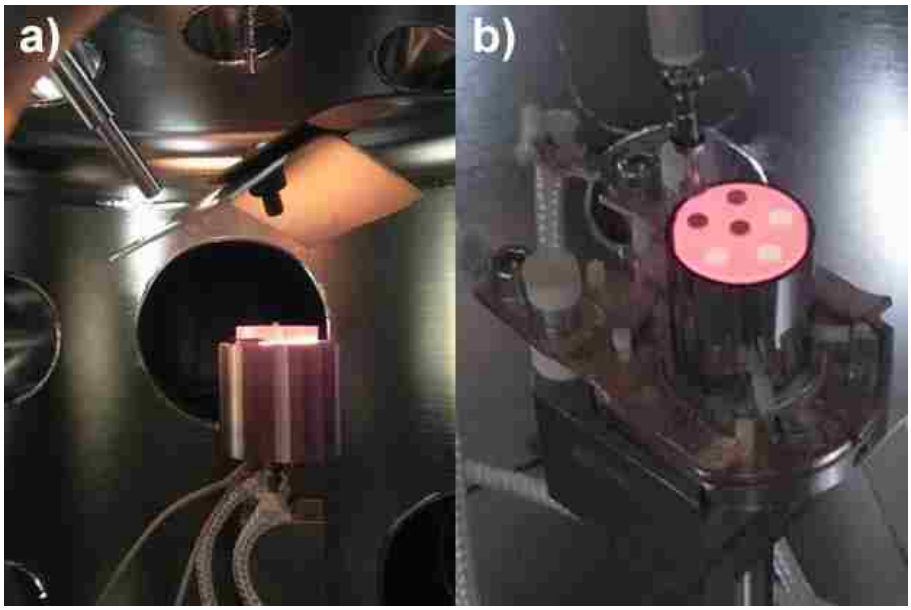

Figure 3.11 a) A button heater was the first iteration of a cathode heating stage, but was temperature limited and b) is a heater sled that was designed and developed by 3M Ceradyne, Inc., which is the final version of a cathode heating stage.

Care must be taken such that the maximum filament temperature of the heater sled is not exceeded. The maximum filament temperature of the tungsten-rhenium wire used in the heater sled cannot exceed 1720 °C. This can be determined through the relation in Equation 3.8. A table of experimental values are given in Table 3.1 for the heater sled obtained by 3M Ceradyne, Inc. in approaching the maximum filament temperature.

$$T_{fil} = \left(\frac{V_{fil}}{I_{fil}R_C}\right)^{\alpha} * 298.15 - 273.15$$

Equation 3.8 Filament temperature equation [93].

Where T_{fil} is the filament temperature, V_{fil} is the voltage measured across the filament, I_{fil} is the current traveling through the filament, α is a material specific parameter (α = 1/0.94 for tungsten-rhenium), and R_C is the cold resistance of the filament at room temperature. This is a calibration curve of sorts to determine what voltage and current can be applied to the filament to obtain a given cavity temperature, where the filament temperature in Table 3.1 is modeled by Equation 3.8. The cavity temperature was measured via disappearing filament optical pyrometry.

Table 3.1 Experimental data provided by 3M Ceradyne, Inc. in approaching the maximum filament temperature.

V_{fil}	I_{fil}	T_{cavity}	T_{fil}
4.0	4.440	897	1010
4.5	4.723	959	1090
5.0	4.991	1017	1160
5.5	5.261	1065	1228
6.0	5.524	1113	1292
6.5	5.576	1154	1351
7.0	6.019	1199	1407
7.5	6.257	1236	1464
8.0	6.487	1269	1516
8.5	6.697	1299	1572
9.0	6.913	1335	1622
9.5	7.121	1366	1671

3.4.2 Kelvin Probe, Work Function and Photoemission

There are several methods to obtain the work function of a material and they generally fall into two categories: indirect and direct. The use of a Kelvin probe (indirect) and photoemission (direct) are the two methods used in this dissertation to obtain work function information.

The working principle of the Kelvin probe is simple: form a parallel plate capacitor with two conductors, provide an electronic path in an external circuit between the two

conductors, and use a backing potential to note where the electric field between the two conductors vanishes [94]. A schematic of this process is depicted in Figure 3.12. If two dissimilar metals form a parallel plate capacitor and are not electrically isolated, their Fermi levels will align resulting in a flow of electrons from the material with a smaller work function to the material with a higher work function. A potential gradient (V_{CPD}) is setup resulting in an electric field between the two plates, shown in Figure 3.12 b). A "backing" potential (V_b) can be used to determine the point where the electric field vanishes. At this unique point, the difference in work function between the two plates ($\Delta\Phi_{AB}$) is equal, and opposite, to the backing potential. In other words, $V_{CPD} = -\Delta\Phi_{AB}$ [94]. By knowing the work function of one of the conductors in the capacitor (the Kelvin probe tip, Φ_A) and the backing potential needed to cancel out the electric field, it becomes a simple algebraic problem to determine the work function of the material in question (Φ_B), shown in Equation 3.9.

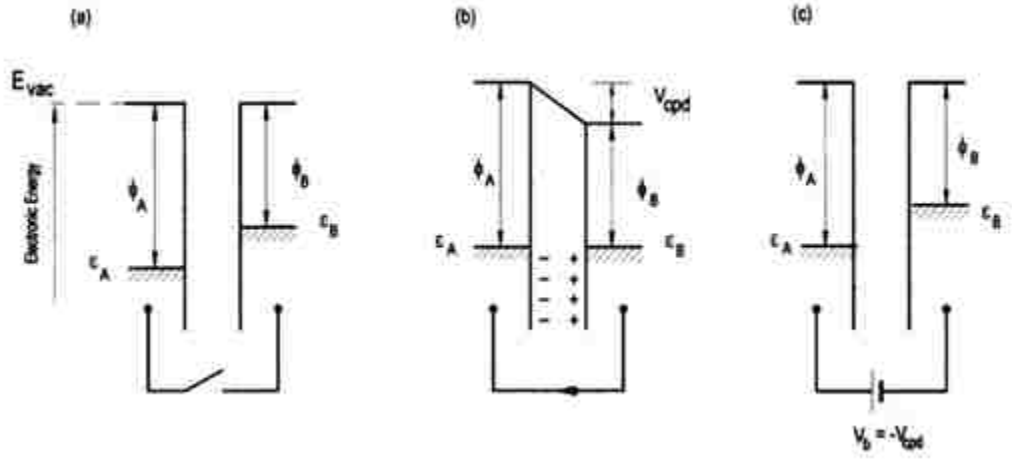

Figure 3.12 Schematic of the Kelvin method. In a) two dissimilar materials form a parallel plate capacitor. In b) the materials form an external circuit via electrical contact and in c) a backing potential eliminates the electric field between the two plates (Reproduced from [94] with permission from the American Institute of Physics).

$$\Phi_A = \Phi_B + V_{CPD}$$

Equation 3.9 Sample work function determination via the Kelvin method [94].

The disadvantages of using the Kelvin probe is that it relies on assumptions made for the work function of the reference tip, and its stability under the experimental conditions. These assumptions can be mitigated by using the photoelectric effect [95]. The system we have for measuring absolute work function still utilizes the Kelvin probe tip in conjunction with a light source (quartz Tungsten-Halogen or deuterium). In this arrangement, the Kelvin probe tip acts as a current collector for liberated electrons. Two light sources are necessary because they each have different photon wavelengths, and therefore energies. The quartz Tungsten-Halogen lamp and associated spectrometer can output variable wavelengths between 400 and 1000 nm (E_{photon}: 3.1-1.24 eV) [95]. The deuterium source (DUV) emits ultraviolet radiation with photon energies between 3.0-7.0 eV [95]. The combination of these two sources allow us to access the appropriate range for both an unactivated and activated cathode for absolute work function characterization. The photoelectron emission and collection is a 4-step process outlined in Figure 3.13 and described below [95]:

1) Incident photons are absorbed and an electron is emitted, provided the energy of the photon is greater than or equal to the work function of the material. After the electron is ejected from the surface, there is an image force (IF) between the emitted electron and the positively charged surface that extends to approximately 30 nm. At this point, the electron is subject to external electric fields and atmospheric conditions.

2) An electron cloud can be formed under ambient pressure conditions through the collision of the electron and large molecules like N_2, O_2, and H_2O. While kinetic information is lost, charge is conserved. This is not a condition of concern when experiments are carried out in vacuum.

3) The electron/ion is accelerated toward the positively biased Kelvin probe tip. The field gradient is typically on the order of 10 V/mm.

4) The electron/ion current is recorded as a function of photon energy and expected to increase according to the Fowler relation, $(E_{photon} - \Phi_M)^{1/2}$ [96].

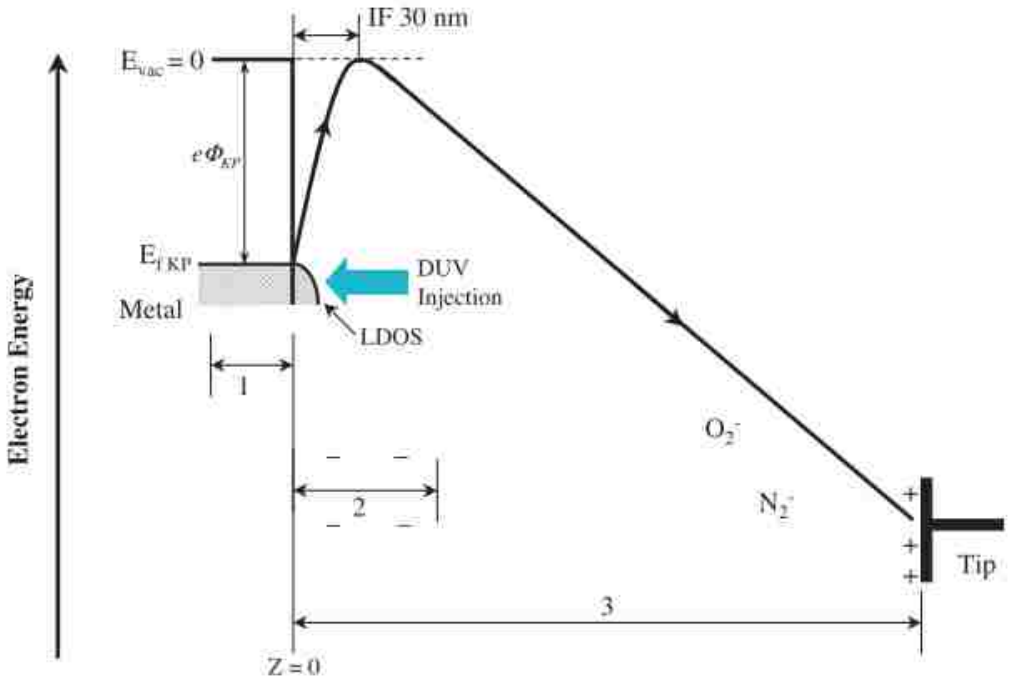

Figure 3.13 An illustration of the photoemission and collection process (Reproduced from [95] with permission from Elsevier).

4 The Fabrication and Characterization of Bimodal Nanoporous Si-Mg

4.1 Introduction

The first experiments to produce porous silicon used hydrofluoric acid (HF) and were discovered by accident when attempts to electropolish had failed [12]. Decades of development lead to engineering applications in waveguides, sensing and biosensing technology, drug delivery, and energy storage systems due to the inherent physical and chemical properties of the material [19, 97-102]. There are several techniques to produce porous silicon, but the most established technique utilizes HF and alcohol (ethanol or methanol) to etch a silicon wafer [102-104]. There are a wide range or pore sizes/shapes that can be obtained by tuning etching parameters [105, 106]. A significant disadvantage to using this technique stems from the highly toxic and corrosive nature of the etchant – HF – that requires special care for transportation and disposal.

Silicon is an attractive material in energy storage devices because of its ability to absorb large amounts of lithium, for use in lithium-ion batteries [107]. The drawback in the storing of the lithium, however, is that the silicon must expand by up to 300% in order to accommodate the lithium. This tends to result in catastrophic failure, as silicon is a known brittle material, when thin films of silicon are subjected to battery cycling [108]. As a result, methods to circumvent the catastrophic failure have been the subject of intense study. The pioneering work by Ostlund et al. showed that by creating nano-structured silicon, one can mitigate brittle failure through the confinement of dislocations [1, 109]. This has lead to an increase in the study to create novel techniques for the production of

nano-structured silicon [28, 29, 110, 111]. Nanoporous materials are attractive because of their small ligament sizes and high surface-area-to-volume ratio.

Dealloying is a common technique to produce nanoporous materials with ligaments tens of nm in size [7, 8, 10, 112, 113]. Chemical dealloying is among the earliest techniques to produce nanoporous materials dating back to ancient times, and still used today. This method is often used to create nanoporous structures of noble metals, but the pioneering work by Wang et al. showed that the use of binary alloys containing Mg can be dealloyed to create nanoporous structures not limited to noble metals [33, 114]. The results from Wang were the motivation for the current chemical dealloying procedure.

A more recent discovery is the creation of dealloyed materials that exhibit a hierarchal (multimodal) structure [23-25]. Materials fabricated in this way offer unique advantages for engineering applications that stem from the different ligament classes and chemical activity of the system. For example, the larger ligament class can promote mass transport, while the smaller ligament class can increase chemical activity [26, 27]. These attributes have already shown great promise in lithium-ion battery applications in the creation of bimodal nanoporous silicon and micro-nano porous Si-Ag [28-30].

It has been observed that introducing electrically conducting materials into the matrix of porous silicon can be an effective method to help improve electrochemical performance [28]. Strategically modifying the crystal structure of the matrix has also been shown to improve cycling behavior, specifically in making amorphous thin films or nanowires [115-118]. The focus of this study is the facile manufacture of bimodal nanoporous silicon with retained magnesium through distilled water dealloying of sputter-deposited thin films that have a final thickness of at least 1μm, where the by-products are

environmentally benign. Fundamentally, this is an interesting material system whose structure and chemical composition hold great promise for future applications in lithium-ion batteries.

4.2 Experimental

4.2.1 Materials

The targets of silicon (99.999% purity), magnesium (99.95% purity), and Cr (99.95% purity) were purchased from AJA International, Inc. Silicon wafers were purchased from Virginia Semiconductor and were (001)-oriented phosphorus doped with a thickness of 368 μm. Ethanol (95%) was purchased from Fisher Scientific. Distilled and deionized water were used in the majority of the dealloying experiments. A water chiller from was used in the majority of dealloying experiments, but preliminary experiments were conducted in an ice bath kept in a walk-in refrigerator kept at 40°F.

4.2.2 Film Deposition Parameters

Alloy films of Si-Mg were deposited in a magnetron chamber (ORION system, AJA International, Inc.) from silicon and magnesium targets onto a single crystal silicon wafer and copper foils. Interlayers of Cr or Si were used to promote adhesion. The working pressure for deposition was 2.5 mtorr in an atmosphere of argon. The base pressure before deposition was less than 5×10^{-7} torr. Prior to deposition, a corona discharge was used to clean the substrates in an atmosphere of argon at a pressure of 25 mtorr. This was done by applying a substrate bias of 35 watts RF for 1.5 minutes. Afterwards, a 10 nm interlayer of either Si or Cr was used to promote adhesion between the substrate and film. Finally, the Si-Mg film was deposited using one of two deposition techniques: gradient or uniform composition.

4.2.3 Composition Gradient

A common technique for determining the parting limit for a binary alloy system is to create a composition gradient such that the ratio of the two elements have small, but recognizable changes from one sample to the next [119, 120]. The substrate carrier in the sputtering machine has a diameter of about 3 inches that can used to create the composition gradient by co-sputtering from diametrically opposed targets. Substrates of silicon and copper were broken and aligned linearly across the substrate carrier, along the axis that bisects the silicon and magnesium targets. In this way, the precursor composition can be associated with a given microstructure after dealloying. The composition gradient that can be achieved across a diameter of 3 inches depends on a number of deposition parameters, the most important of which is the relative deposition rates between the two targets. The substrate dimensions of each sample that comprised the gradient had sufficiently small dimensions to ensure that the as-deposited composition remained relatively constant across each piece.

4.2.4 Uniform Composition

Once the parting limit has been obtained through the gradient composition experiments, films of uniform composition can be deposited. This is achieved by sputtering from targets that are not necessarily diametrically opposed onto a rotating substrate. The rotation compensates for any discrepancies in target placement such that a uniform film is grown. It is desirable to create films of uniform composition because they tend to dealloy more uniformly without cracking [119, 120].

4.2.5 Optimization

Several attempts were made to reduce the dealloying rate and involved the use of a variety of solvents including: isopropyl alcohol, methanol, ethanol, distilled and deionized water. There was not a significant difference in microstructure between the distilled and deionized water, but the use of those solvents at reduced temperatures yielded the best bi-continuous microstructures. However, sample yield was always quite low even though the experimental variables were kept constant from one experiment to the next. In order to increase sample yield, other attempts were made that involved purging the water with nitrogen, agitation of the dealloying solution, and changing the deposition parameters, but none of those techniques helped increase sample yield.

4.2.6 Vacuum Annealing

All vacuum annealing experiments were carried out in the sputtering chamber at base pressures below 5×10^{-7} torr. The samples were loaded on the backside of the substrate carrier, facing the quartz lamps the sit about 1 cm from the substrate carrier. Annealing was carried out at a temperature of 500°C for 2 hours and allowed to cool overnight. The heating rate was 10°C min^{-1}.

4.2.7 Free Corrosion Dealloying

The preliminary attempts were guided by scientific principles and hypotheses for processing steps that would make the dealloyed films more reproducible, more uniform, and/or less oxidized. All samples in this study were dealloyed through free corrosion, without the use of a potentiostat. All samples were dealloyed in vials that could hold volumes up to 30 mL. The best method to produce nanoporous films with the characteristic bi-continuous structure was through a two-step process where the films were inserted into

vials that had been pre-heated to 50°C, leaving them there for about 30 minutes and then transferring the vials to the water chiller (Thermo Electron Corporation, Neslab RTE 7), kept at 0.5°C for the remainder of the dealloying time. Skipping the first step, would also yield nanoporous films with a bi-continuous structure, but seemed to have a lower sample yield. Our hypothesis is that putting the films in the 50°C water first allowed the samples to begin dealloying and once that process had started, it needed to be slowed down to prevent cracking and delamination. Typically, the total time for dealloying was between 48 and 72 hours, which ensured that the film had been dealloyed throughout the thickness. Once dealloyed, the films appeared light yellow, black or dark gray to the naked eye.

4.2.8 Characterization

EDS measurements of as-deposited films were performed indide a Zeiss EVO MA 10 equipped with a Bruker EDS, while EDS mapping was performed inside a FEI Quanta 250 FEG equipped with an Oxford EDS system. Chemical mapping through the film thickness (using a liftout lamella) was acquired over a period of 2 hours, with drift correction settings applied such that counts were maximixed from the EDS detector for the thin sample. Scanning electron microscope (SEM) images were taken with a Hitachi S-4300 cold-cathode field emission microscope and a FEI Helios Nanolab 660 field emission microscope. Sample preparation for transmission electron microscopy (TEM) was performed inside a focused ion beam-scanning electron microscope (FIB-SEM, FEI Helios Nanolab 660) using a Ga^+ ion source for milling. Information about the crystal structure was obtained through the use of a JEOL 2010F TEM. Surface analysis was carried out inside a Thermo Scientific K-Alpha x-ray photoelectron spectrometer (XPS), which utilized a monochromatic Al-Kα x-ray source with a spot size of 400 μm. In addition to

using an electron flood gun during XPS analysis to prevent charging, all spectra were calibrated to the known value of 285 eV for adventitious carbon. All XPS spectra were fit with mixed Gaussian-Lorentzian curve fitting software. X-ray diffraction (XRD) experiments were performed with a Siemens D500 Krystalloflex Diffractometer. Samples were scanned from 20° to 80° (2θ) in 0.01° steps at 0.5° min^{-1}.

4.3 Results and Discussion

4.3.1 Preliminary Attempts to Create Nanoporous Silicon

As mentioned previously, it is desirable to fabricate nanoporous silicon nominally 1 μm to understand the mechanical behavior via nanoindentation to avoid the substrate effect. Attempts at dealloying Si-Mg precursor material approximately 500 nm thick, under the same conditions that yielded nanoporous silicon for films that were less than 200 nm thick, failed. The thicker films appeared to suffer from severe cracking and delamination, which is characteristic of an etching process that occurs too rapidly [121]. A simple method to slow down the rate at which the reaction takes place is to lower the temperature, as the dissolution rate given in Equation 2.3 depends on temperature. The first attempts to slow down dealloying were performed in an ice bath. Gradient samples after dealloying that were 500 nm thick are shown in Figure 4.1. Table 4.1 shows that the parting limit range for this system is between 46 and 61 at. % Si, which differs slightly from the observations by Jiang et al [34]. Nevertheless, using water near its freezing point seems to work very well at producing nanoporosity without cracking and delamination. This is presumably because the dissolution of the magnesium was occurring too fast at temperatures of 50°C and reducing the temperature is a simple method to slow down the reaction. These results appear promising for scaling up to 1 μm thick films.

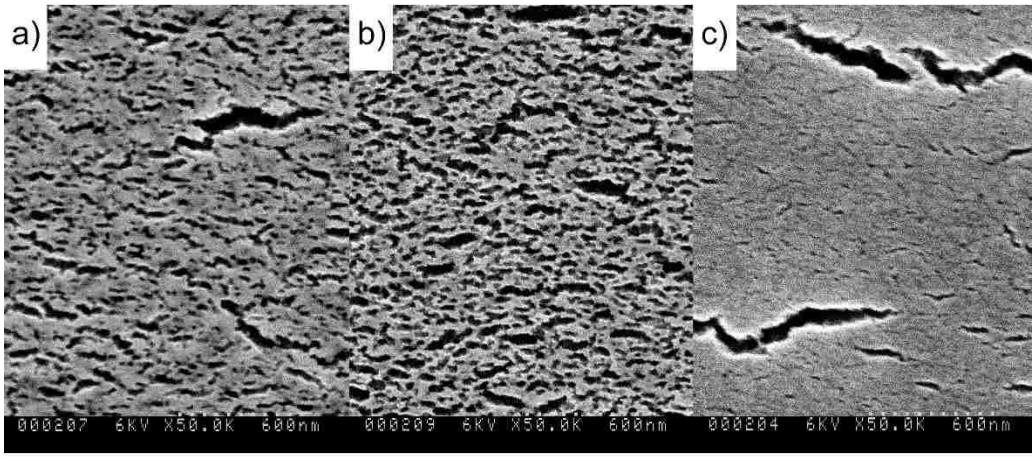

Figure 4.1 As-dealloyed 500nm gradient samples of nanoporous Si dealloyed using an ice bath. a) is sample 2, b) is sample 3 and c) is sample 4.

Table 4.1 The chemical composition of the 500 nm Si-Mg film before and after dealloying, obtained with EDS on the Zeiss.

	As-deposited		As-dealloyed	
	Si (at. %)	Mg (at. %)	Si (at. %)	Mg (at. %)
Sample 2	61	49	84	16
Sample 3	48	52	93	7
Sample 4	46	54	98	2

A gradient of one micron thickness was sputtered in a similar manner as the 500 nm thick gradient, except the deposition time was increased. The films were then dealloyed in an ice bath and the resulting microstructures are displayed in Figure 4.2. The precursor compositions for the one micron gradient films are displayed in Table 4.2. It was interesting that the films deposited on the copper foils did not dealloy, like the films that were only 500 nm thick. This made it difficult to obtain as-dealloyed compositions. This is because

the nanoporous silicon films were supported by silicon substrates and EDS cannot distinguish between a silicon film and a silicon substrate. It appears that the film with the best bi-continuous structure was sample 5, which had a parting limit of approximately 54 at.% silicon.

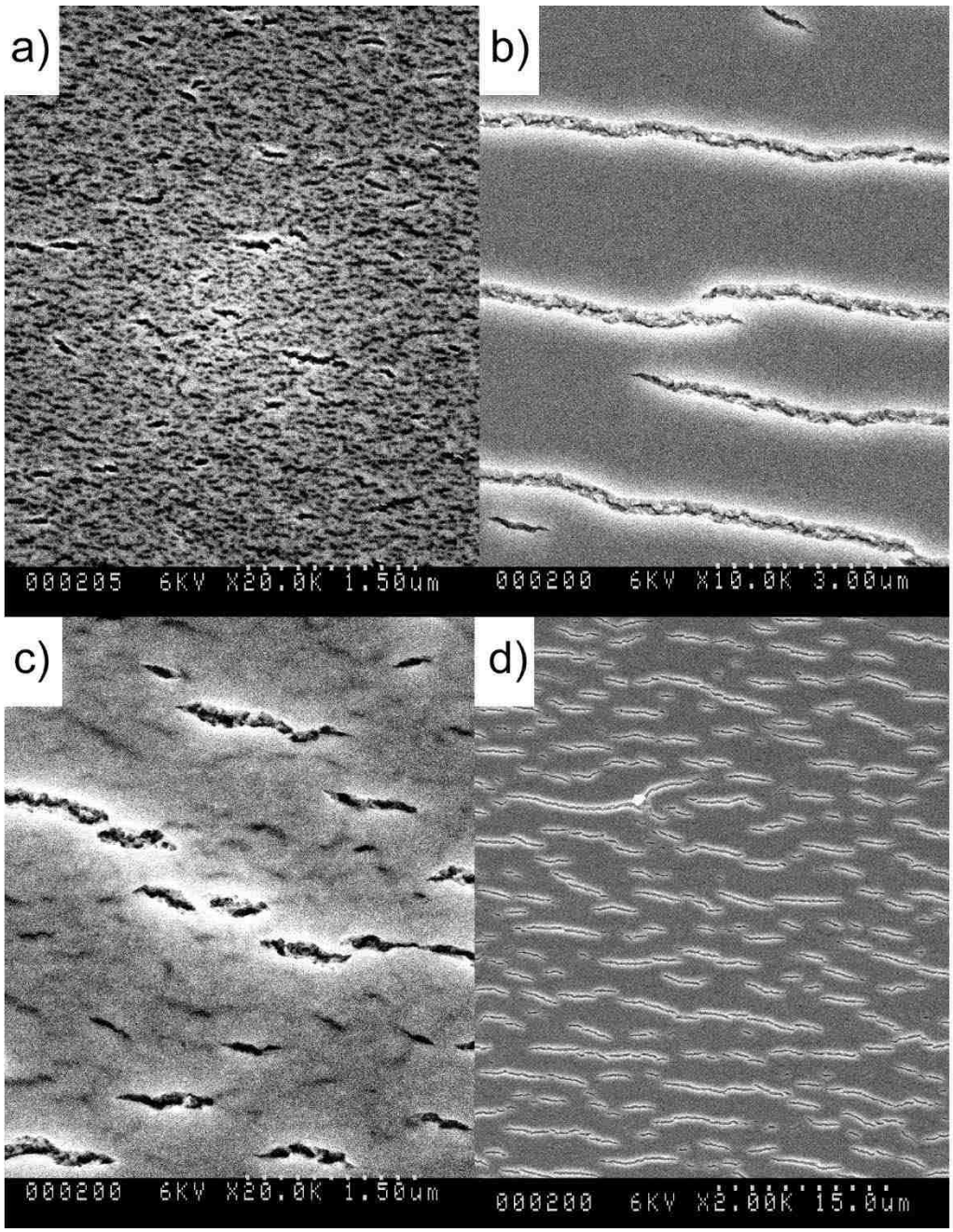

Figure 4.2 As-dealloyed gradient planar-view images of the 1 μm thick films. a) is sample 5, b) is sample 6, c) is sample 7 and d) is sample 8 for composition reference in Table 4.2. It would appear the sample 5 exhibits the best bi-continuous structure of all the films.

Table 4.2 The chemical composition of the 1 μm thick precursor films. The optimum parting limit for the Si-Mg system appear to be 54 at.% silicon, corresponding to sample 5.

	As-deposited	
	Si (at.%)	Mg (at.%)
Sample 5	54	46
Sample 6	52	48
Sample 7	50	50
Sample 8	46	54

The results obtained by simply cooling the water were promising, and exhibited a desirable microstructure. The next logical step in this process would have been to begin making uniform composition films of Si-Mg, based on the parting limit studies performed on the gradient films, and dealloying them. Since reasonably good results were obtained quickly by simply decreasing the temperature of the dealloying water, it was decided to explore other avenues for dealloying the Si-Mg system to see what structures could be obtained. The other avenues for dealloying included dealloying in methanol, isopropanol, and ethanol in various concentrations. The logic in choosing these solvents stemmed partially from their previous use to create porous silicon through HF etching [19]. In that process, the alcohol was used as a wetting agent to promote pore infiltration of HF etchant. Beyond that, the freezing point of those alcohols are less than that of water, which could be used to lower the freezing point of a water-alcohol solution such that the dealloying process could take place at temperatures lower than 0°C. The most remarkable results from

this study are outlined in Figure 4.3, with an outline of the dealloying conditions in Table 4.3.

A natural starting point for dealloying in alcohol, was to use similar dealloying conditions discovered to work well when dealloying in water. Tests 1-4 in Table 4.3 were performed in accordance with the procedure developed for dealloying in water, but did not yield a color change in the sample surface – a common indicator to determine if dealloying had taken place. Tests 5 and 6 exhibited some color change on the samples with low precursor compositions of Si. The films in tests 7-9 exhibited slight color changes. Upon further inspection, it appeared that there was a needle-like surface layer that lifted off after a quick rinse in vinegar. The films appeared totally black afterwards. We presume the surface layer was $Mg(OH)_2$, but cannot be sure. Further analysis with XPS would be required. The structures shown in Figure 4.3 are those that were underneath the surface layer. Regardless of the type of alcohol, all structures resembled plates, rather than the bi-continuous structure produced from dealloying in water. The plate-like structures were very good visible light absorbers. It was surprising how black the films were after the vinegar rinse. This may be a good indicator of the applications of these films in solar cell technology where silicon is typically used in the conversion of photon energy to electrical energy. It should be noted that all the films in the alcohol dealloying study were gradient films, and that the films that produced the best results in tests 7-9 were from the same deposition.

Table 4.3 A summary of alcohol dealloying conditions.

Test Identifier (#)	Gradient Composition (at. % Si)	Dealloying Solution (vol.%)	Dealloying Time (hrs)	Dealloying Temperature (°C)
1	51-60	Ethanol (100)	48	50 for 30 min, then 0.5.
2	51-60	Isopropanol (100)	48	50 for 30 min, then 0.5.
3	51-60	Isopropanol (50)	48	0.5
4	42-61	Ethanol (50)	48	0.5
5	42-61	Isopropanol (50)	24	23
6	42-61	Ethanol (50)	24	23
7	36	Isopropanol (50)	24	23
8	36	Ethanol (50)	24	23
9	36	Methanol (50)	24	23

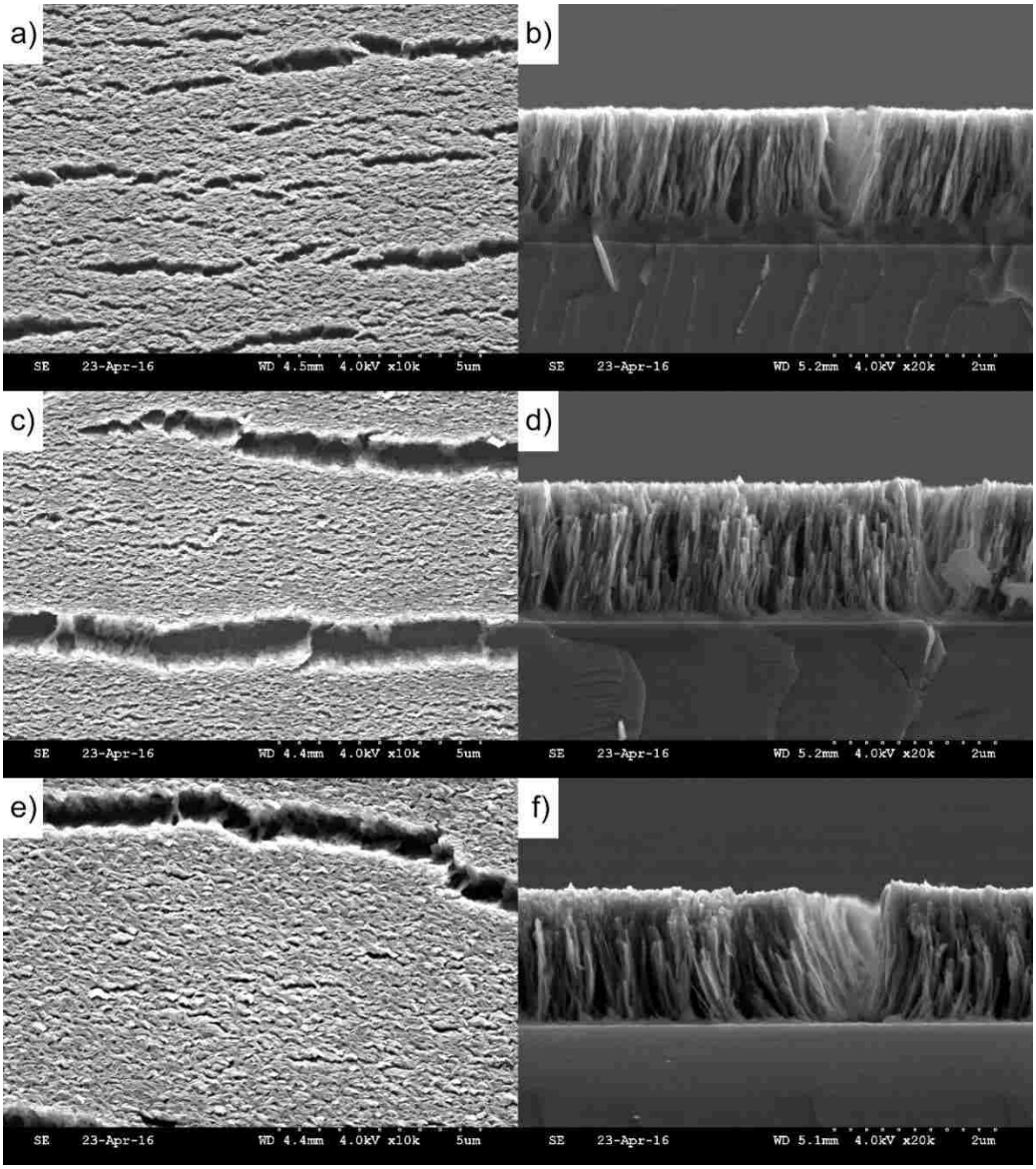

Figure 4.3 A representation of the best structures obtained in the alcohol dealloying study. All the films have a similar plate-like structure. a) and b) correspond to test 7, c) and d) to test 8, and e) and f) to test 9 in Table 4.3.

4.3.2 Preliminary Attempts to Create Nanoporous Silicon Micro-Pillars

The testing of small volumes of materials is desirable in instances where bulk testing is not possible because of processing limitations or because of material inhomogeneity that exists on a very small scale. Probing such small volumes to obtain mechanical information can be a challenging endeavor. Nanoindentation is a technique that

has been developed and improved immensely in recent years such that it can achieve sub-nanometer displacement resolution and nano-Newton force resolution [122]. Micro-pillar compression testing is another form of mechanical testing that can be used to investigate the mechanical behavior of small volumes of materials that are difficult to manufacture on a bulk scale, with the added advantage that one can observe deformation mechanisms with in-situ electron microscopy [123]. The fabrication of micro-pillars can be challenging and there are many geometrical aspects that must be taken into account in the creation of micro-pillars including: fillet radius and aspect ratio that can significantly influence the results [124].

At the outset, we considered milling a pillar out of material that had already been dealloyed. The preliminary results in Figure 4.4 give an overview of how the nanoporous structure reacted with the Ga^{+} ion beam. Figure 4.4 a) shows the as-dealloyed nanoporous structure before ion bombardment and Figure 4.4 b) shows coarsening of the nanoporous ligaments with mild exposure to the ion beam. After near complete removal of the nanoporous material, as shown in Figure 4.4 c) and Figure 4.4 d) there is a significant amount of material redeposition that has occurred at the interface between the milled and non-milled areas. Since we were trying to fabricate micro-pillars with a diameter on the order of 500 nm, if there is a significant amount of material redoposition, it will influence the mechanical behavior in ways that are not representative of the true material behavior.

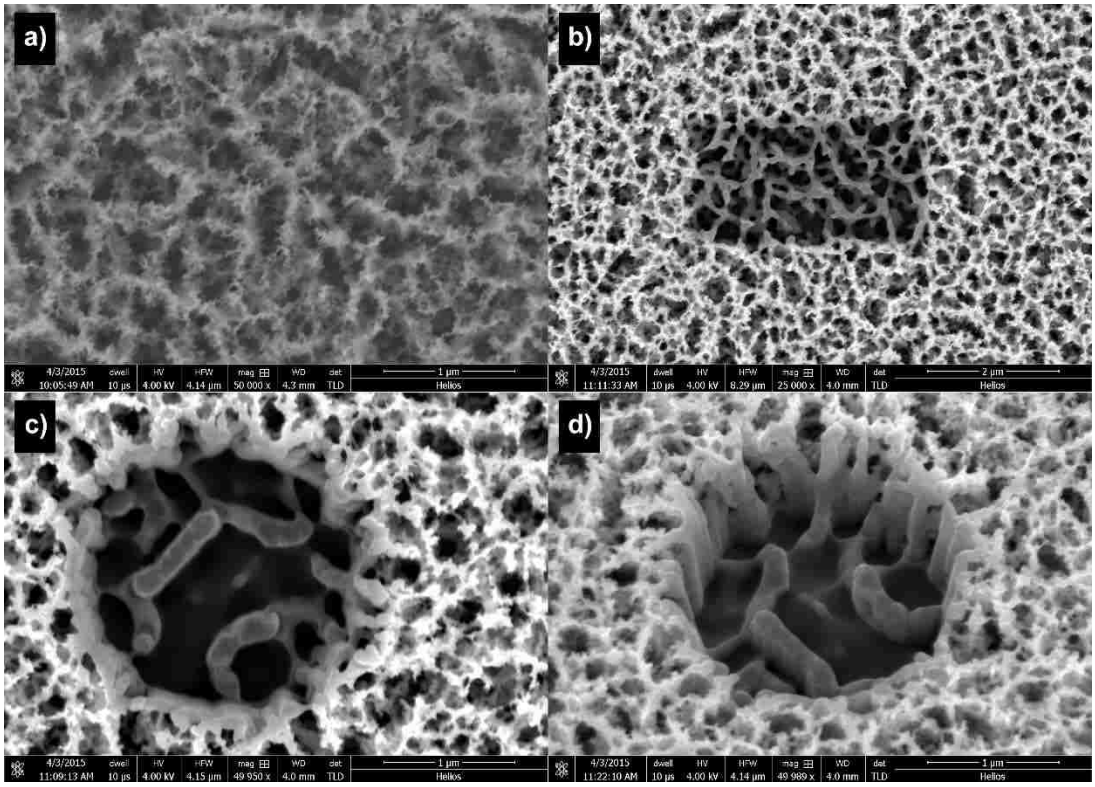

Figure 4.4 This image shows the effect of milling a nanoporous structure with a Ga^+ ion beam. a) represents the as-dealloyed structure. b) shows coarsening of the ligaments after a brief ion etch. c) shows significant coarsening of the nanoporous structure and the formation of a thick recast layer after ion milling. d) is the same image as shown in c) except viewed at 30° from plane normal.

Since the nanoporous silicon could not be milled without significant damage to the surrounding nanoporous structure, attempts were made to mill out the pillars and trenches *apriori* to avoid any redeposition that could influence the mechanical behavior. The trenches were made because these were intended to be compressed in-situ with a TEM to observe deformation mechanisms. Figure 4.5 a) shows the final dealloyed material that was obtained only after the milling steps. Carbon paint has apparently adhered to the lower half of the silicon wafer and covered some of the regions of interest after attaching the sample to the TEM specimen holder. The red squares in Figure 4.5 a) are representative of the areas depicted at higher magnifications in b), c) and d). In Figure 4.5 b), it is evident that

very little dealloying occurred near the regions that were ion milled. This is presumably the result of Ga^+ implantation in the surrounding areas that has impeded the dealloying process. Figure 4.5 c) shows a dealloyed region away from the ion milled areas and corresponding to the brighter areas near the middle of the film. The darker areas are undealloyed. Finally, Figure 4.5 d) shows a representative undealloyed micro-pillar that was also affected by the Ga^+ implantation. As a result, nanoporous silicon films were created on large planar surfaces and subsequently tested via nanoindentation.

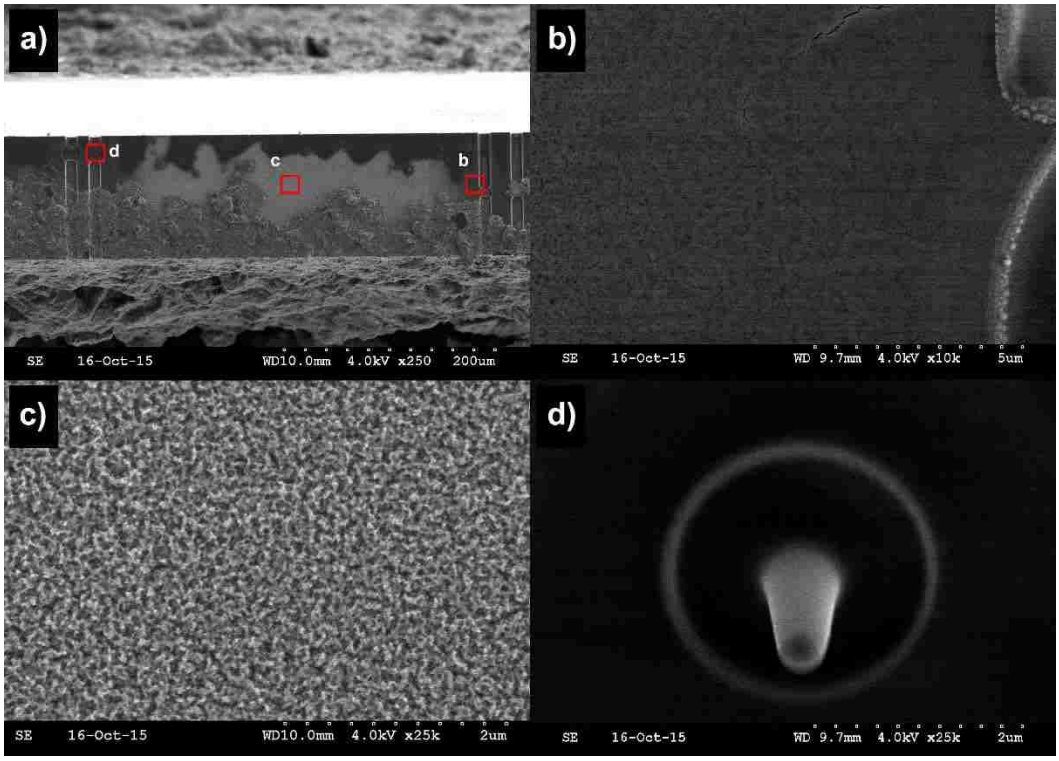

Figure 4.5 a) The as-deposited Si-Mg precursor film that was deposited on the edge of a silicon wafer, milled with the FIB and then dealloyed. The red squares and indicators show the regions where b), c) and d) were taken from the dealloyed film. b) shows that the film was not dealloyed near Ga^+ milled regions. c) corresponds to the bright regions in a) that were further from the Ga^+ milled regions that did dealloy. Finally, d) shows a representative micro-pillar that did not dealloy.

4.3.3 Identification of Parting Limit Range for Dealloying in Water

The gradient used in the alcohol dealloying study (shown in Figure 4.3) was sputtered under the same conditions as the gradient used for dealloying in water (shown in Figure 4.6) for comparison. The water dealloying results pictured in Figure 4.6 were obtained in a more controlled manner through the use of a water chiller that kept the water at exactly 0.5°C. EDS was performed on the precursor samples and verified that the parting limit range is between 51 and 54 at% Si (see Figure 4.6 c) and Figure 4.6 d)). Below 51 at.% Si significant cracking and delamination occurs, as is expected when the relative rate of Mg dissolution to Si adatom surface diffusion is too high. Above 54 at% Si (see Figure 4.6 a) and Figure 4.6 b)) dealloying occurs locally at the surface, but slows to an eventual halt as Si adatom surface diffusion forms a passivating layer to prevent further Mg dissolution. This is shown in Figure 4.6 b), where the dealloyed film meets the undealloyed film. Figure 4.6 e) and Figure 4.6 f) shown signs of cracking and delamination of the film from the substrate, as is common in the preparation of gradient films [120]. The gradient sample that exhibited the best bi-continuous structure is pictured in Figure 4.6 d), which was then used as a guide to create uniform composition samples for dealloying.

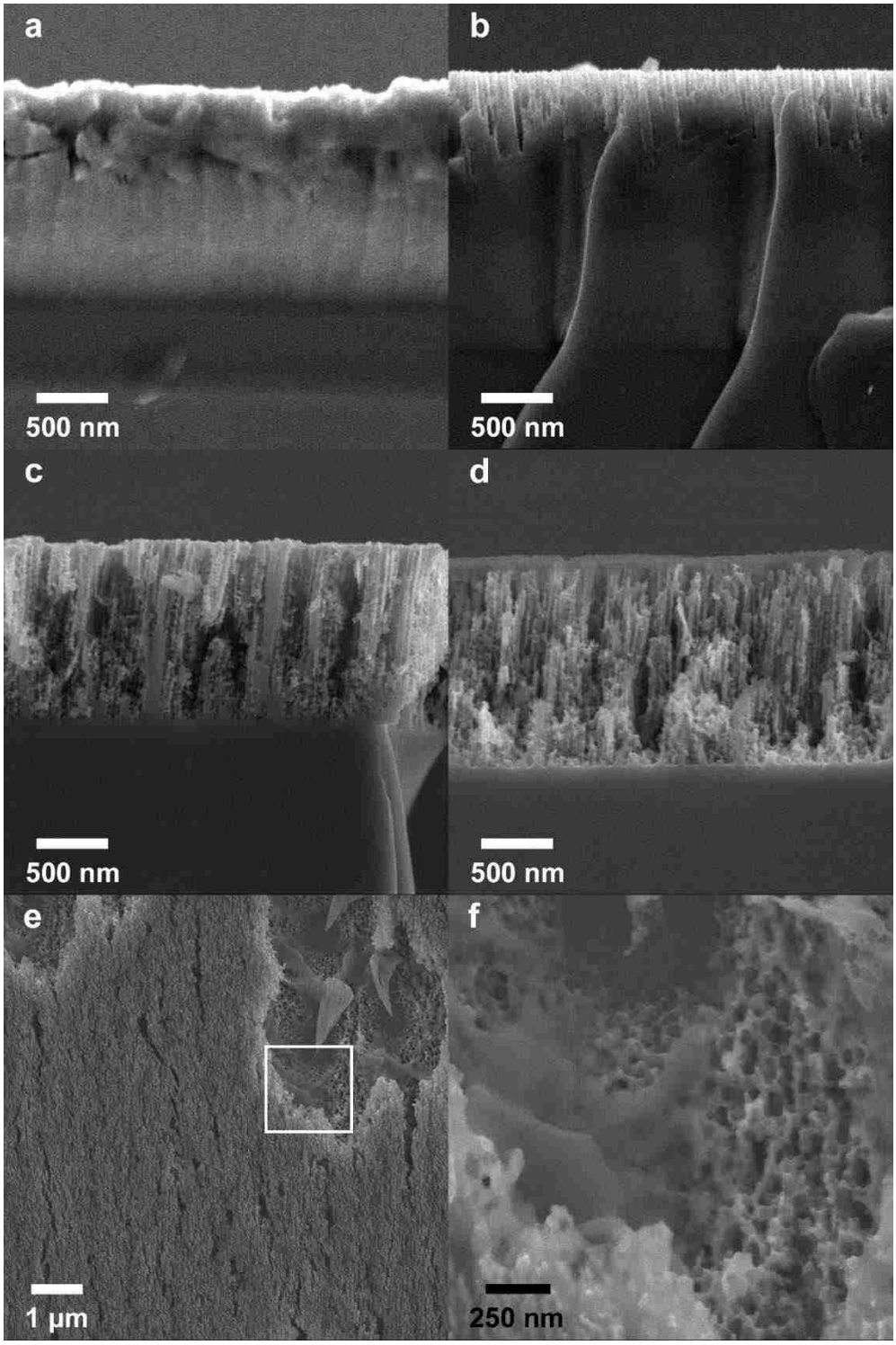

Figure 4.6 Gradient samples of Si-Mg were dealloyed in distilled water. The SEM micrographs represents the dealloyed structures that correspond to precursor compositions spanning a range between 51-58 at.% Si, and were used as a guide to determine the optimum parting limit for dealloying this metal-semiconductor alloy system.

a) Precursor composition was 58 at.% Si and upon water immersion there was little or no observable corrosion. b) Precursor composition was 56 at.% Si and dealloying appeared to occur locally at the surface but quickly halted due to Si passivation. c) Precursor composition was 54 at.% Si and dealloying appears to have penetrated to the substrate, but still shows signs of undealloyed regions. d) Precursor composition was 51 at.% Si and the film is fully dealloyed, exhibiting open porosity and fully bi-continuous network of ligaments and pores. e) A planar-view image of the film shown in c) that displays signs of cracking a partial delamination. f) A magnified image of the boxed area in e) to show the microstructure of the underlying film as well as a barren region where the film was completely delaminated [125].

4.3.4 Hierarchal Ligament Structure

Films of uniform composition were deposited using the parting limit range obtained with the gradient film deposition. Planar-view and cross-section micrographs of the nanoporous film after dealloying are shown in Figure 4.7. It was interesting to observe that most of the dealloyed films had an intermittent surface layer that obscured the underlying nanoporous film, shown in Figure 4.7 b). The surface layer had a characteristic thickness less than 100 nm and appeared to be slightly porous. The nanoporous film was not completely obscured, as shown in the planar-view image in Figure 4.7 a). The structure displays large, open porosity with a hierarchal ligament structure. ImageJ software was used to measure the ligaments and it became apparent that there were two ligament classes present, with one having an average diameter of 83 ± 18 nm and the other 19 ± 5 nm. There were sixty ligaments measured in total with the distribution split between the two ligament classes.

The cross-section image shown in Figure 4.7 c), reveals that the structure of the nanoporous film is inhomogeneous. There is a dense layer present at the surface that sharply transitions to large, open porosity with a hierarchal ligament size that extends to at least half the film thickness and gradually becomes denser when approaching the silicon substrate (shown by the inset in Figure 4.7 c). There did not appear to be a significant

difference in the dealloyed structure, regardless of the presence or absence or the surface layer. A surface layer has been observed to occur in other dealloyed systems, but could not be sufficiently explained [126]. In the work by Pd-Ni sytem, the surface layer was observed to peel off with extended dealloying.

The authors observed the film thickness to contract by a large margin during the dealloying process, by comparing the precursor film thickness to the as-dealloyed film thickness. This phenomenon has been documented in the dealloying of other material systems and is quite commonplace [33, 112, 127]. The nanoporous Si-Mg film contracted by approximately 31%, which resulted in a final thickness of 1070 nm after dealloying. In other material system where the film contracted by similar margins, a large amount of cracking was observed [112]. The nanoporous Si-Mg films showed no signs of cracking after dealloying, which stands as a testament to the materials ability to withstand large strains without catastrophic failure. This implies that the material could be a good candidate in lithium-ion battery applications where resilience to large strains is paramount.

Materials that exhibit a hierarchal structure can be created using numerous methods that involve dealloying [23, 27, 128]. The mechanism that creates the different classes of ligaments is best described as local heterogeneities that exist throughout the material that have different local dissolution and surface adatom diffusion kinetics [23, 27, 128]. Song et al. describe this process in the dealloying of a two-phase Cu-Al alloy, where the two phases behave differently to the chemical etchant [27]. The work by Detsi et al. use a complex dealloying-plating-annealing-dealloying approach to create multimodal nanoporous Au [23]. In both examples, the mechanism leading to the hierarchal structure is the result of different dealloying behavior of local heterogeneities. Here, the authors

present a facile method that employs magnetron sputtering-dealloying of a Si-Mg film to create a hierarchal structure.

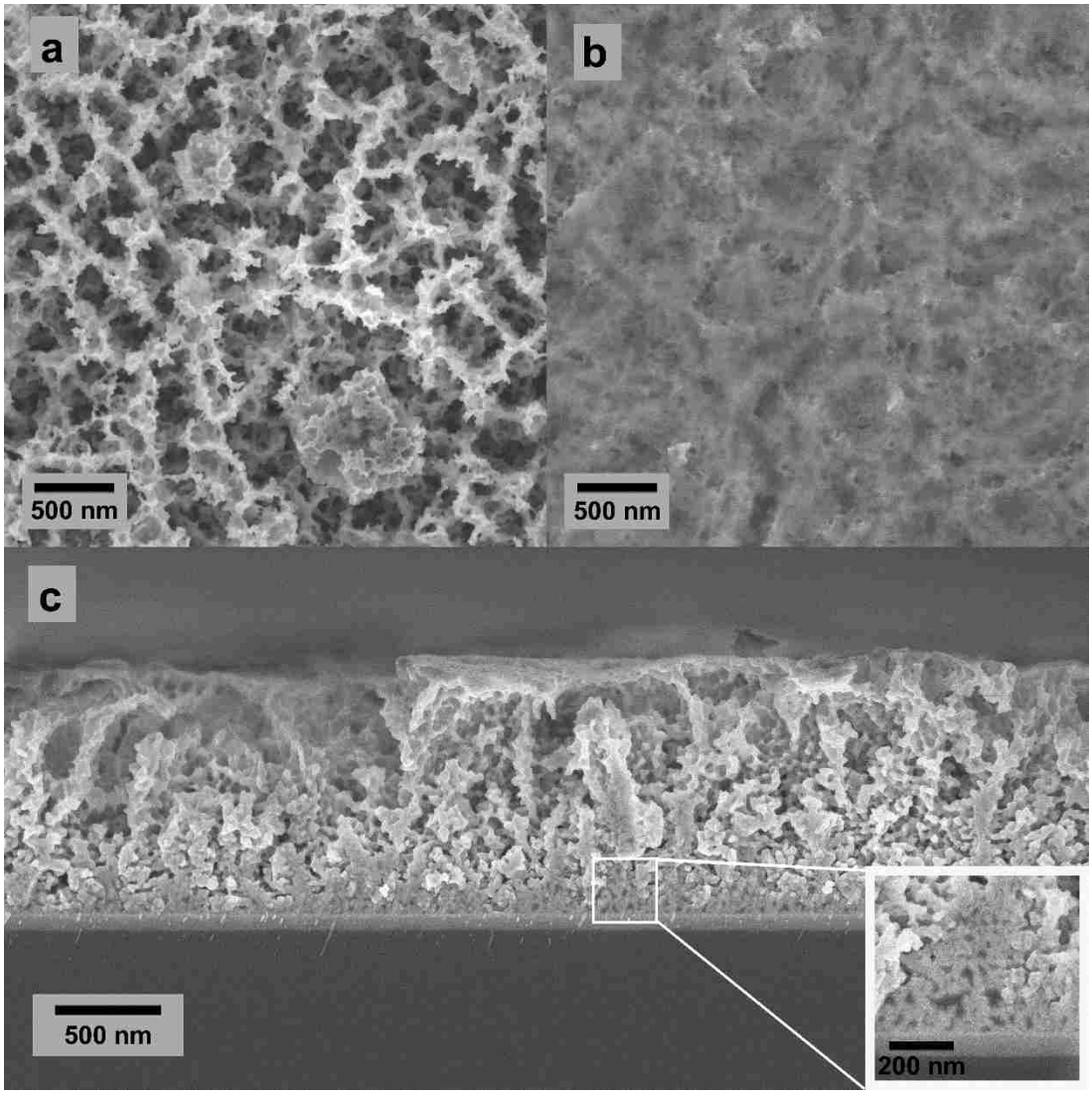

Figure 4.7 SEM micrographs of the uniform composition films dealloyed in distilled water. a) Depicts the bimodal nature of the nanoporous film underneath the b) surface layer that partially obscures the film. A cleaved cross-section is shown in c) of the as-dealloyed film, showing the inhomogeneity's that exist throughout the film thickness. The inset shows a higher magnification image of the structure nearer the substrate, where the porosity is much denser [125].

4.3.5 Precursor Film Structure

It is instructive to look to the binary phase diagram of the Si-Mg system – shown in Figure 4.8 - to determine the phases one might expect to be present in the film at the composition of interest, $Mg_{47}Si_{53}$ [129]. At that composition, one might expect to observe Mg_2Si with the fluorite structure and diamond cubic silicon (dc-Si). However, magnetron sputtering is a non-equilibrium process that does not necessarily crystallize in a manner one might expect based on equilibrium conditions. Indeed, XRD scans of the precursor film do not show that either dc-Si or Mg_2Si exist.

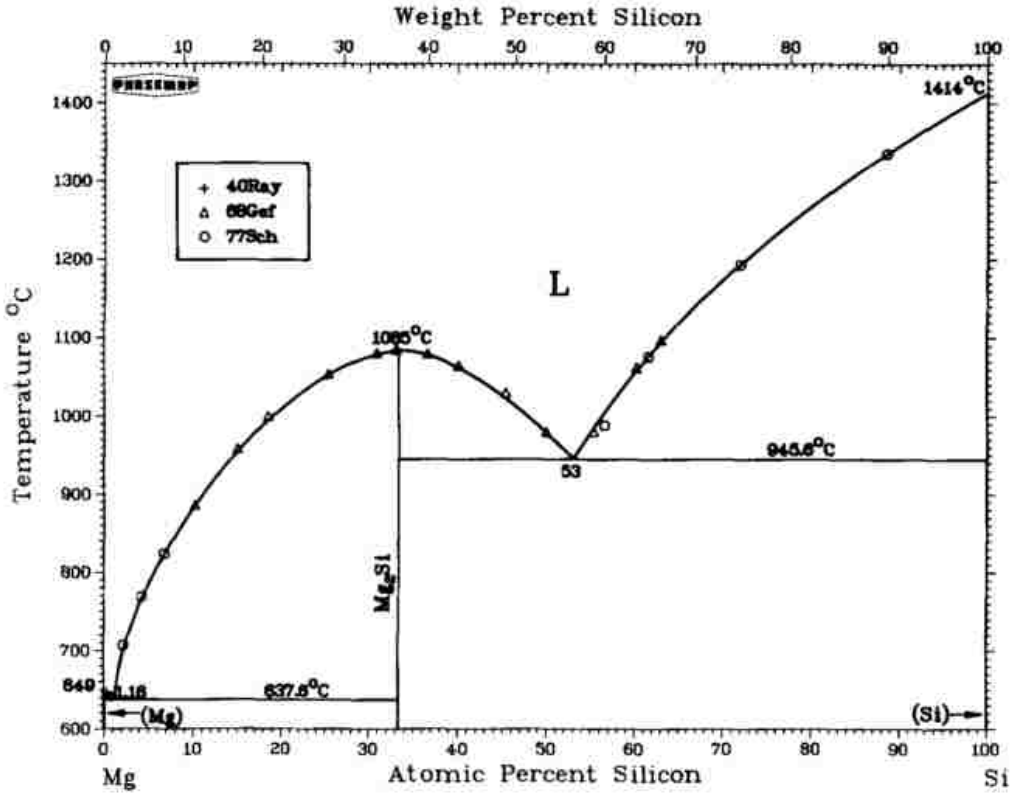

Figure 4.8 The Si-Mg phase diagram (Reproduced from [129] with permission from Springer Nature).

An XRD scan of the precursor film is observed in Figure 4.9. The large bump at approximately 23° is characteristic of an amorphous structure, which can only be explained

as the film structure. There do not appear to be any other remarkable features that can be attributed to the film. While the film appears to be largely amorphous, it is entirely possible – and even likely – that local heterogeneities that exist throughout the film thickness [130]. We are of the opinion that these are likely local concentrations of magnesium. This type of phase separation would provide a mechanism to explain the hierarchal structure of the films described previously. However, it would require a carefully prepared TEM specimen to observe the true nature of the as-deposited film throughout the thickness. The other peaks in the XRD scan at 69° and ≈ 33° are from the silicon substrate upon which the Si-Mg film was deposited. The small bump at 69° is commonly observed in diffraction experiments involving (001)-oriented Si wafers and represents diffraction from the (004) planes of the wafer. The broad bump at 33°, which was unexpected, can be explained by the forbidden reflection from the (002) planes of the Si wafer. This is a documented phenomenon that can sometimes occur and known as *Umweganregung* [131].

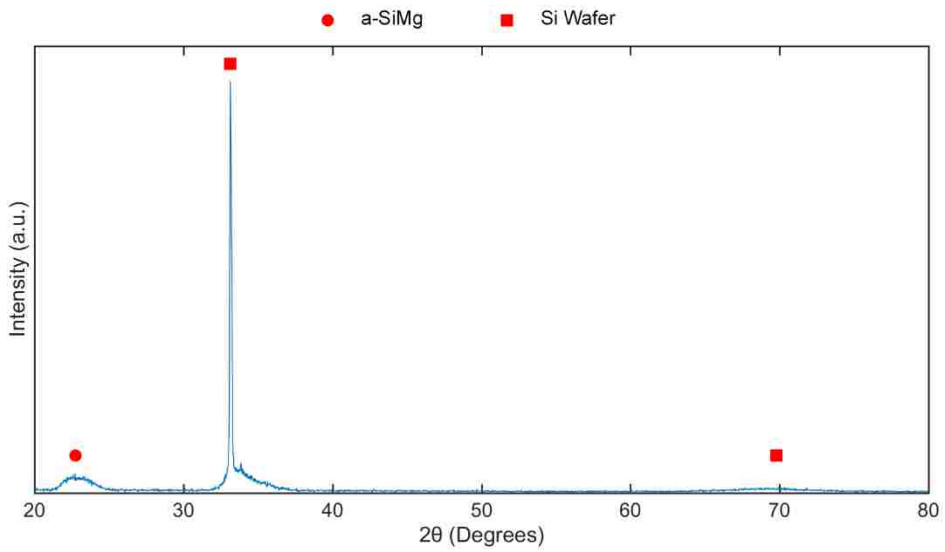

Figure 4.9 This is an XRD scan of the precursor Si-Mg film before dealloying. It was deposited on a (001)-oriented single crystal silicon wafer. The precursor appears to be amorphous (a-SiMg) [125].

4.3.6 Surface Analysis

XPS analysis was performed on films with and without the surface layer, to investigate the composition and bonding state of the elements in the near-surface region of the respective films; the results are summarized in Figure 4.10. The film that was topped by a thin surface layer appears to be composed of a sub-oxide of silicon along with magnesium oxide in the following stoichiometry: SiO_x ($x \leq 2$) and MgO, as deduced from the binding energy and shape of the peaks observed at 102.8 eV and 1303.7 eV, respectively [132-134]. In contrast, the film without the surface layer contained elemental silicon (labeled "Si" in Figure 4.10 d) and corresponding to the elemental Si-Si peak identified by the XPS software and consistent with the NIST database of XPS peak energies) in addition to SiO_x ($x \leq 2$) and MgO, as determined by the peaks at binding energies of 99.1 eV, 102.6 eV, and 1304.0 eV, respectively [132-134]. It is noted that the peak in Figure 4.3 with label "SiO_x" corresponds to Si that has been oxidized, and again is

consistent with the NIST database of XPS peak energies for various oxides of Si. The relative peak areas from the XPS scans were used to determine the chemical composition of the films, as depicted in Table 4.4. The film with the surface layer appears to have no elemental Si at the surface, and it has more retained Mg in the form of MgO.

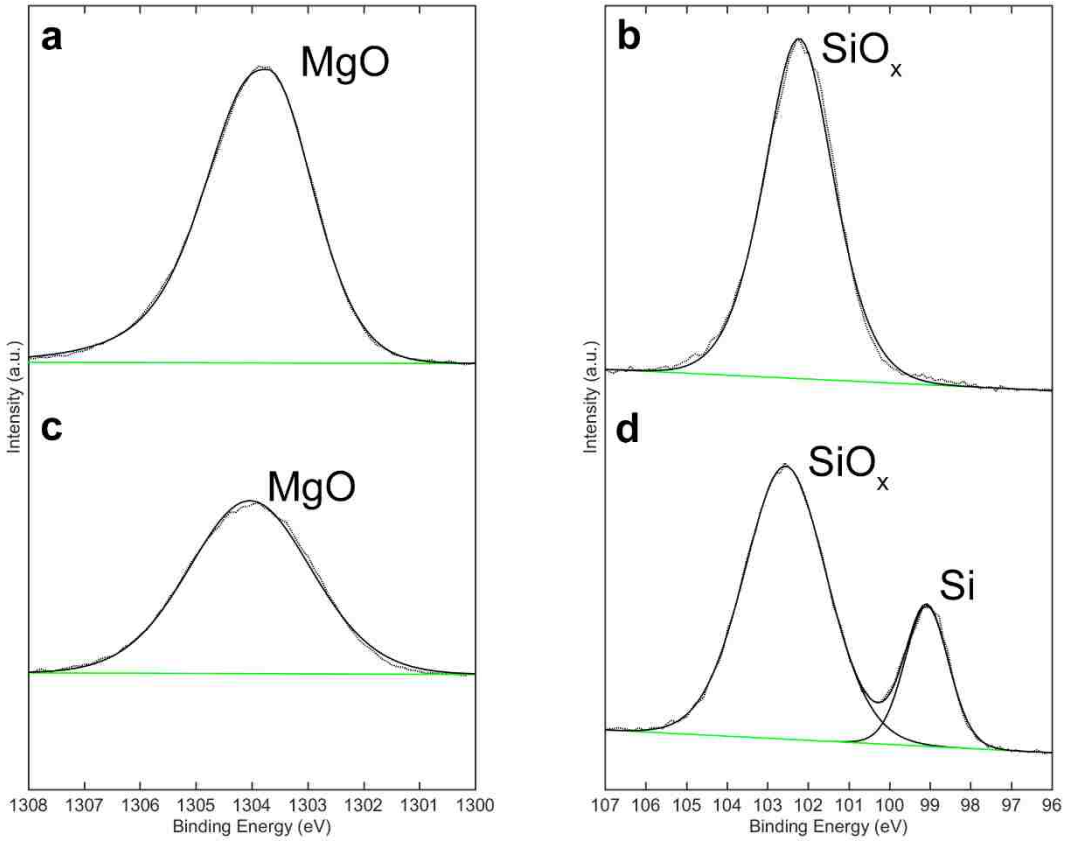

Figure 4.10 A surface analysis of the as-dealloyed films using XPS. Scans corresponding to the binding energy of Mg 1s and Si 2p were observed. Scans a) and b) are from the sample with a surface layer, while scans c) and d) are of the sample without the surface layer. The sample with the surface layer is observed to be composed primarily of oxides, where the sample without a surface layer shows some amount of elemental silicon [125].

Table 4.4 Relative amounts of each phase in the surface layer of np-Si samples, as determined from the integrated area under each corresponding peak of the XPS scans in Figure 4.10 [125].

Np-Si Film Type	SiO_x (at%)	Si (at%)	MgO (at%)
With surface layer	59.4	0	40.6
Without surface layer	56.9	15.6	27.5

4.3.7 TEM Investigation of Film Structure and Composition

Electron-transparent samples for TEM investigation were carefully prepared in the Helios FIB-SEM using focused ion beam milling. Two lamellae were prepared in this manner. The first was an as-dealloyed film that had no surface layer and the second was a vacuum annealed specimen that included the surface layer. The high-resolution TEM image in Figure 4.11 a) shows a ligament of silicon where Pt nanocrystals were deposited during the liftout process, resulting in decoration of the amorphous silicon ligament. Selected area electron diffraction (SAED) of the as-dealloyed sample, depicted in Figure 4.11 b), revealed diffuse scattering indicative of an amorphous matrix along with a number of faint diffraction spots attributed to fcc-Pt (these diffraction spots are, therefore, artifacts arising from the lamella preparation process, and are not inherent to np-Si). The lattice fringes in Figure 4.11 a correspond to the (111) planes of fcc-Pt. ImageJ was used to determine the fringe spacing by using the line profile function, which plots pixel grayscale along the length of the ling and allows measurement of the spacing of lattice fringes. Ten consecutive fringes were measured and averaged for the best results, confirming the observation of (111) planes in fcc-Pt.

SAED of the annealed sample was performed in the upper film region, as well as near the substrate, to investigate differences manifested through the thickness of the film. The high-resolution TEM image in Figure 4.11 c) along with the SAED pattern in Figure 4.11 d) was acquired near the substrate. The ligament in Figure 4.11 c) shows Si nanocrystals that formed during annealing, with an inset of the (111) lattice fringes for dc-Si. These fringes were measured with ImageJ in the same manner mentioned previously. Figure 4.11 c) and Figure 4.11 d) reveal that annealing had partially crystalized the sample, forming nanocrystalline dc-Si, with no appreciable amount of Mg present near the substrate. The bright field image in Figure 4.11 e) shows the area near the substrate where the high-resolution TEM image in Figure 4.11 c) was taken. Figure 4.11 f), which does not have a corresponding TEM image, indicates that both crystalline Si and MgO are present near the mid-height of the film.

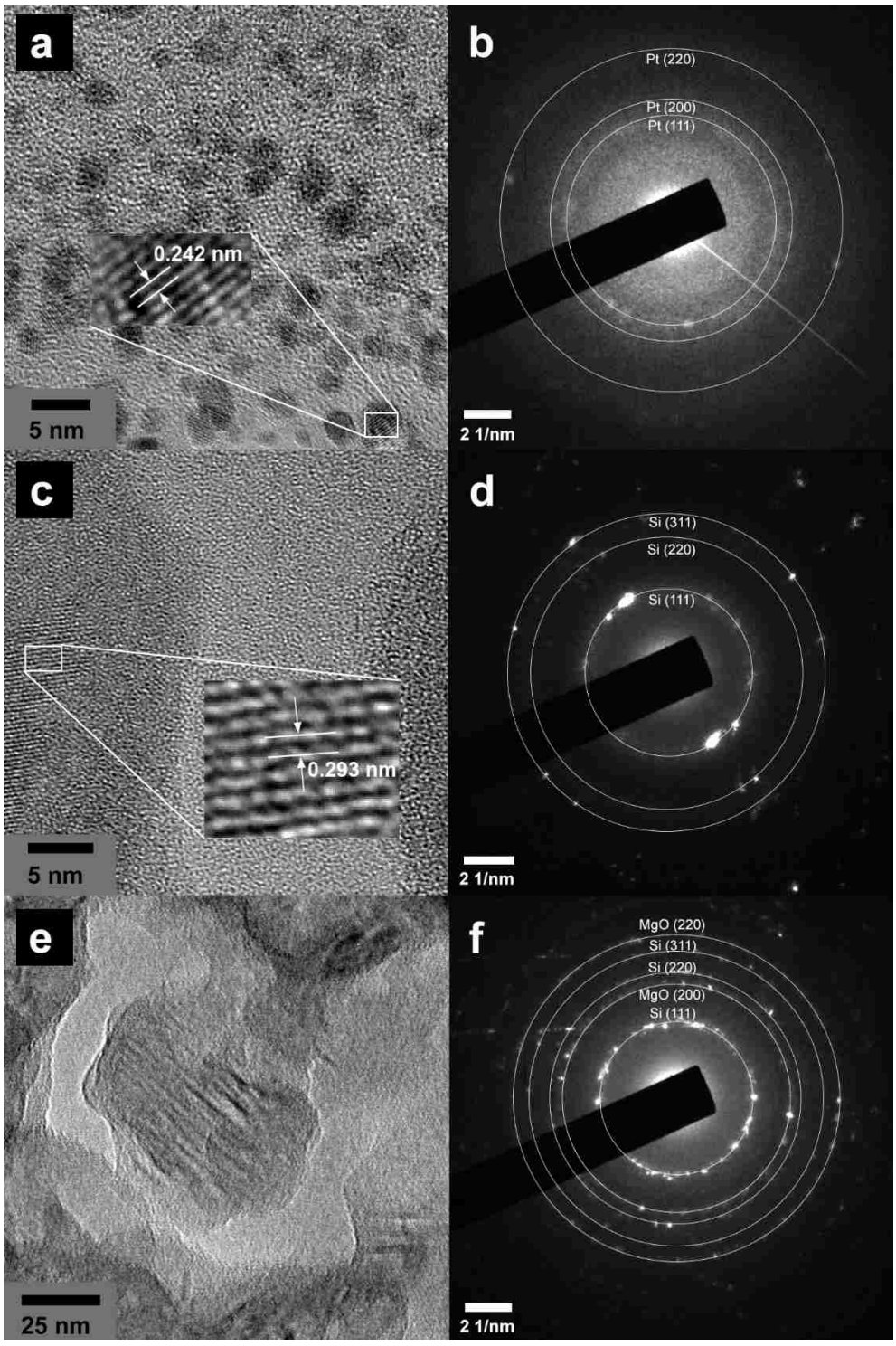

Figure 4.11 TEM micrographs a, c, e) and selected area electron diffraction patterns b, d, f) of both as-dealloyed and dealloyed/vacuum-annealed samples were obtained to investigate structural changes during processing. a) and b) show the amorphous nature of the as-dealloyed films. c-f) correspond to the vacuum annealed

counterpart. c-e) were obtained at a location near the substrate, while f) was recorded at the mid-height of the film [125].

The EDS mapping results from Figure 4.12, which are later quantified in Figure 4.13 corroborate this result by showing that no appreciable amount of Mg is detected within 200 nm of the substrate. This makes sense because the smallest available TEM aperture corresponds to a sample region of ≈ 100 nm diameter, which is small enough to obtain a diffraction pattern near the substrate, from np-Si with no detectable level of Mg. The general area described in the current paper as the "upper film region" applies to those regions at least 200 nm above the substrate. The electron diffraction results in Figure 4.11 f) (from the mid-height of the film, or upper film region) support the XPS results, which indicate that the surface is composed of MgO and elemental Si. The diffuse scattering observed in TEM diffraction mode is most likely the result of an amorphous sub-oxide of silicon convoluted with amorphous elemental Si and Mg. The presence of diffraction rings from MgO in Figure 4.11 f) corroborates the results from EDS mapping, which show that Mg is retained in the upper region of the film (see Figure 4.12). However, it is likely that some of the residual Mg acts as a dopant in the silicon matrix. Doping the silicon in this manner actually makes it a suitable candidate for lithium-ion battery application by providing an electron conducting pathway [28-30]. Moreover, the amorphous nature of the as-dealloyed material makes it more attractive for lithium-ion battery applications due to the enhanced cycling behavior reported in the literature [115-118].

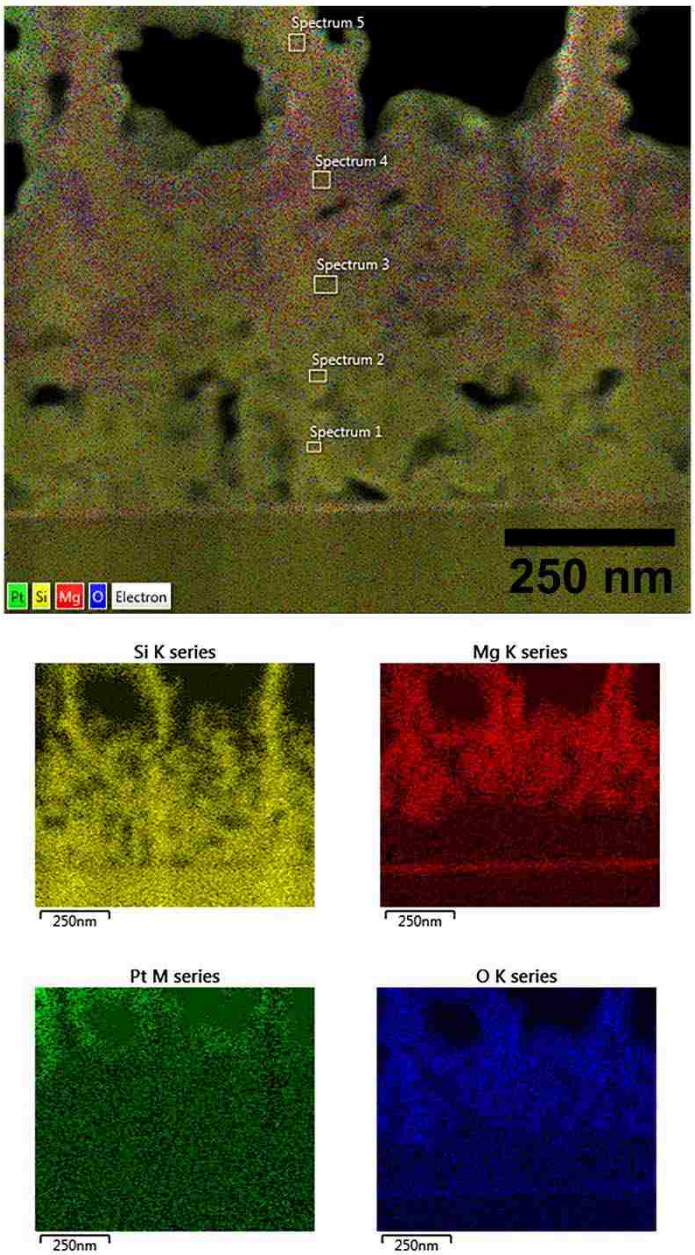

Figure 4.12 EDS chemical maps indicating qualitative distribution of various elements through the film thickness. More Mg is retained in the bulk of the film and near the surface, but not near the substrate. Pt is also observed to penetrate into the sample, as a result of the liftout process used for preparation of the TEM sample (a protective pad of Pt was used here) [125].

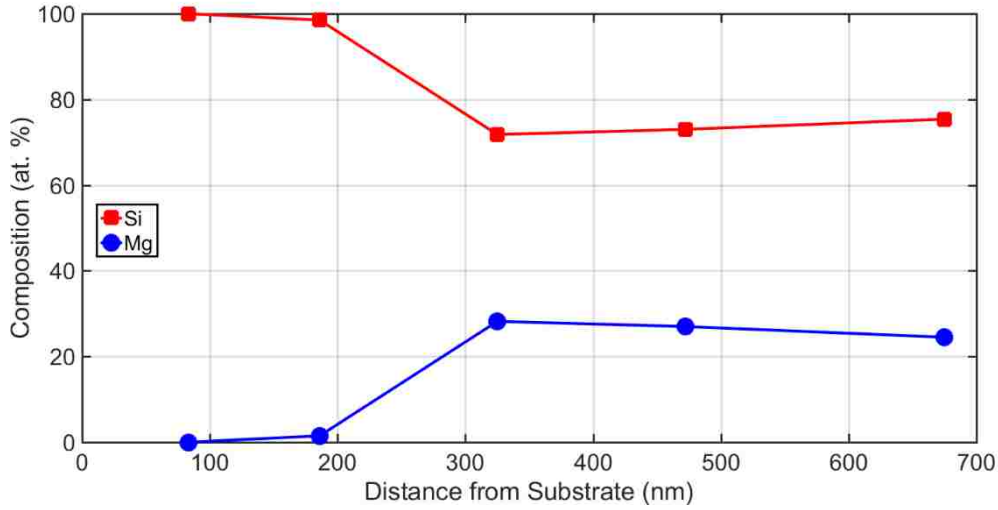

Figure 4.13 Quantitative EDS analysis was performed at discrete intervals through the film thickness, corresponding to markers on the EDS map in Figure 4.12. This provides a quantitative measure of composition variation through the film thickness. The values toward the right of this plot should match the XPS compositional analysis in Table 4.4, if the film composition is the same from 700 nm to the surface of the film. The EDS and XPS values do indeed match, which would be expected since the same sample (with no surface layer) was analyzed using both techniques [125].

4.3.8 Discussion of Corrosion Behavior

The surface analysis results described above appear, initially, to be in stark contrast to the work done by Taheri et al., where an ingot of Mg was corroded in water through the use of an electrochemical cell [135]. They report the formation of a layered structure consisting of a thin MgO-rich inner layer topped with a $Mg(OH)_2$-rich outer layer. Interestingly, the surface layer produced by the films in the present study has a thickness (≈ 100 nm) similar to that observed by Taheri and coworkers. Additionally, the MgO-rich inner layer produced in the electrochemical cell is noticeably more porous than the exterior $Mg(OH)_2$, which appears to corroborate the results in the present study. It is curious, however, that $Mg(OH)_2$ is not present in any appreciably amount in the present study. Based on the Pourbaix diagram, one would expect the overall corrosion reaction of magnesium with water to be [136]:

Equation 4.1 Magnesium-water corrosion reaction.

$$Mg + 2H_2O \rightarrow Mg(OH)_2 + H_2$$

Equation 4.2 Magnesium-water partial reaction 1.

$$Mg \rightarrow Mg^{2+} + 2e^-$$

Equation 4.3 Magnesium-water partial reaction 2.

$$2H_2O + 2e^- \rightarrow H_2 + 2(OH)^-$$

Equation 4.4 Magnesium-water partial reaction 3.

$$Mg^{2+} + 2(OH)^- \rightarrow Mg(OH)_2$$

The authors are of the opinion that $Mg(OH)_2$ never forms. In other words, the local pH at the solid-electrolyte interface never reaches equilibrium pH for the formation of $Mg(OH)_2$ to occur, which corresponds to a local pH of approximately 11 [133, 135, 136]. Also, it is unlikely that $Mg(OH)_2$ forms and then decomposes in MgO and H_2O, because the free energy change corresponding to this decomposition is too great [136]. Additionally, $Mg(OH)_2$ is generally regarded as a more passivating layer than MgO [136]. As a result, dealloying would be unlikely to continue in the presence of such a passivating layer. The structure of $Mg(OH)_2$ tends to exhibit a platelet-like morphology, but this was not observed on the film surface [135]. The XPS and TEM data, along with plan-view SEM images, all support the claim that there is no appreciable amount of $Mg(OH)_2$ in the dealloyed films.

It is also worth noting that the structure displayed in the gradient films (Figure 4.6) appears to be more structurally homogeneous than is observed in the non-gradient film in Figure 4.7. This is interesting because non-gradient films typically retain the nanoporous

structure evidenced in the gradient sample, without cracking and delamination that are omnipresent in gradient films [120]. A possible explanation for this anomalous behavior could involve the existence of regions, where Mg dissolution is limited in the non-gradient film. The genesis of these regions in the non-gradient film likely originates from the small parting limit range characteristic of this semiconductor-metal alloy system, combined with the absence of cracks and delaminated regions. Since the parting limit range for this alloy system spans only a few atomic percent, it suggests that small perturbations in composition could affect the dealloying behavior of the film. In this case, the perturbations may result in cracking and partial delamination of the gradient films. Since the dealloyed non-gradient film does not crack or delaminate, this leads to regions of limited Mg dissolution that slightly alter the structure from what is observed in the as-dealloyed gradient films.

4.4 Conclusions

Precursor films of Si-Mg with a composition between 51 and 54 at% Si were dealloyed via free corrosion in distilled water to produce crack-free, bimodal np-Si films with retained Mg. Nominally, these films contact by 31% during dealloying, with a final thickness of approximately 1 μm and with a hierarchal structure of ligament sizes; the larger ligaments have an average width of 83 nm and the smaller ligaments have an average width of 19 nm. TEM of the as-dealloyed np-Si shows it to be amorphous, but the ligaments readily form nanocrystals of Si and MgO (embedded in an amorphous matrix) during vacuum annealing. EDS mapping combined with XPS surface analysis revealed three distinct chemical composition regions in the non-gradient film, where the Mg content generally increases through the film thickness (with increasing thickness from the substrate). XPS surface analysis combined with TEM revealed that the films with a denser

surface layer contained the most residual Mg in the form of MgO, with no appreciable amount of $Mg(OH)_2$. The bimodal nature of these films combined with the amorphous structure make np-Si an attractive materials for lithium-ion battery applications. The different classes of ligaments can be used to promote mass-transport and heighten activity, while the amorpous nature and small size act to fortify the structural integrity of the ligaments against Li cycling. Moreover, the residual Mg concentration in the films would likely promote pathways for electron conduction, while the simple dealloying technique and non-hazardous waste make this an attractive process for scalable production.

While the majority of the characterization in this effort was devoted to the Si-Mg precursor samples dealloyed in distilled water, the gradient samples dealloyed in alcohol solutions were equally interesting. The original motivation for using alcohol-water solvents was because of the wetting properties of alcohol and it's low freezing point. The structure obtained with the alcohol was not the desired bi-continuous morphology, but rather plate-like. Using concentrations of alcohol of about 50 volume percent water and dealloyed at room temperature, followed by a vinegar rinse appeared to yield the darkest films. This is a facile technique to create black silicon that could easily be scaled for mass production and used in the harvest of solar energy.

5 Investigating the Mechanical Behavior of Bimodal Nanoporous Si-Mg

5.1 Introduction

Nanoindentation is an efficient method for probing small volumes of material, with dimensions on the order of 1 μm, to obtain mechanical properties that can inform engineering applications [35-37]. Since the inception of the first commercially available indentation apparatus in the 1980's, progress has been rapid and the technique has evolved significantly, with one of the most notable milestones being the advent of the continuous stiffness measurement (CSM) technique and the additional changes that stem from it [37, 39]. The continuous improvement that has been sustained over these past few decades has largely been the result of experimental research on materials that are well-behaved elastic-plastic solids, as is the case for fused silica, for example. Nevertheless, thin, porous materials that exhibit time-dependence are among the most challenging materials to characterize with nanoindentation, but strategically modifying indentation techniques and careful interpretation of data can be used to extract pertinent mechanical information [37, 54, 55, 57, 58, 60, 137-139].

The motivation for this study comes from a combination of preliminary data observed by Jiang *et al*. and from lithium-ion battery research [34, 108, 116, 140-142]. While silicon is an attractive anode material for lithium-ion batteries due to its high charge capacity, it also suffers from cracking and pulverization during cycling [108]. By increasing the surface-area-to-volume ratio, it is possible for silicon to undergo a brittle-to-ductile transition [1]. Creating nanoporous silicon (np Si) is an effective method to

increase the surface-area-to-volume ratio and may mitigate brittle failure. Jiang *et al*. performed *in situ* nanoindentation of np Si films ~100 nm thickness in the transmission electron microscope These films were produced in a similar manner to those made by Maxwell *et al*., which are the subject of the current study [34, 119]. The results from Jiang *et al*. indicate that np-Si can recover large deformations after indentation, but that study was performed on films that are too thin to be accurately characterized with nanoindentation. As such, the thicker nanoporous silicon-magnesium (np Si-Mg) films produced by Maxwell *et al*. are better suited to nanoindentation [119]. In the current study, a modified CSM technique was used to investigate the damping characteristics of np Si-Mg films in the frequency domain via phase angle measurements [54, 57]. These results were interpreted alongside data collected in the time domain, to facilitate modeling the deformation behavior of np Si-Mg films.

5.2 Experimental

5.2.1 Film Fabrication

The films indented in this study were deposited with a magnetron sputtering deposition system (ORION system, AJA International, Inc.) from targets of silicon (99.999% purity) and magnesium (99.95% purity) in an argon atmosphere with a pressure of 2.5 mtorr. The base pressure of the system before deposition was less than $5x10^{-7}$ torr. Before deposition, the single crystal (001)-oriented silicon substrate (Virginia Semiconductor) was cleaned by applying a substrate bias (35 W) in an argon atmosphere with a pressure of 25 mtorr, followed by the deposition of a 10 nm thick silicon interlayer to promote adhesion. The interlayer was deposited in an argon atmosphere at a pressure of 2.5 mtorr.

5.2.2 Free Corrosion Dealloying

The samples indented in this study were dealloyed in 30 mL vials filled with distilled water that were pre-heated to 50°C. The samples were kept in the 50°C water for 30 minutes and then transferred to a water chiller kept at 0.5°C for the remainder of the dealloying time. The total time required for dealloying throughout the film thickness was between 48 and 72 hours.

5.2.3 Vacuum Annealing

The heat-treated samples were vacuum annealed at 500°C for 2 hours and let cool overnight in the vacuum chamber. The base pressure of the system prior to annealing was less than $5x10^{-7}$ torr and the heating rate was $10°Cmin^{-1}$. The vacuum annealing was performed inside the magnetron sputtering chamber with dual quartz lamps positioned approximately 1 cm above the substrate carrier.

5.2.4 Sample Preparation

The indentation apparatus used was equipped with an iMicro load frame and an iNano actuator (Nanomechanics) because of the large stiffness associated with the load frame and sensitivity of the actuator. Standard samples of PMMA (polymethyl methacrylate, cut to size: 14.5 x 14.5 x 6.1 mm, McMaster Carr) and fused silica (standard reference block: 12.9 x 12.9 x 3.5 mm, Nanomechanics) were used to show the reference calibration for the phase angle was correct and that the measured dynamic response was dominated by the specimen. The fused silica arrived attached to an aluminum puck, but the PMMA and other samples were mounted with a thin layer of Crystal Bond (SPI Spullies). The samples were carefully pressed to ensure excess air and adhesive was removed before completely dry. The diamond Berkovich (Microstar Tech) tip area function was calibrated

on the fused silica sample [39]. Indentation experiments contained a minimum of sixteen indents in a 4 x 4 array where the distance between adjacent indents was at least 30 times the maximum indentation depth.

5.2.5 Nanoindentation Testing

Nanoporous samples with a thickness of 1 μm were created to safely ignore the substrate effect when indenting up to 10% of the film thickness (100 nm), when using the Berkovich tip [46, 50]. A modified CSM technique is used in this study where the indenter is held at a prescribed load after reaching a depth of 80 nm. A hold period of 60 seconds was used to allow the sample's response to the dynamic oscillation of 2 nm to reach steady-state. The best metric to determine the measured phase angle accuracy is it's stability over time, which is why this hold period was chosen. However, only data from the last 5 seconds were averaged. It should be noted that the data collected in Figure 5.1 were obtained at indentation depths of approximately 2400 and 600 nm for PMMA and fused silica, respectively. The hold period occurred at such a large depth for PMMA because it is well known that a processing effect near the surface can give rise to an overestimated phase angle value at depths less than approximately 1500 nm [57]. The authors are aware that instrument effects are likely exacerbated at small contact areas, but the system used in this study utilizes state-of-the-art electronics designed to test materials at low loads/depths. Moreover, every effort to work within the constraints of the thin, porous, time-dependent materials being tested were carefully considered.

5.3 Results and Discussion

5.3.1 Proof of Concept

The modified CSM technique used here was first described by Herbert *et al*., and leverages the ability to achieve steady-state harmonic motion – a necessary condition to accurately determine specimen damping [57]. Additionally, the specimen must dominate the measured phase angle response. This condition exists when Equation 5.1 and Equation 5.2 are satisfied. Finally, measurements to correct the reference phase angle are established using Equation 5.3 - Equation 5.5, to account for shifts in the displacement electronics [57, 58]. The close agreement between measured and corrected phase angle values of well-known materials (polymethyl methacrylate, PMMA; and fused silica) were interpreted as corroboration of experimental accuracy.

$$\left.\frac{f_0}{h_0}\right|_{coupled} \gg \left.\frac{f_0}{h_0}\right|_{free\ space}$$

Equation 5.1 Inequality showing that the specimen dominates the measured phase angle response, not the actuator [57].

$$K_{lf} \gg K_{contact}$$

Equation 5.2 Inequality showing that the damping of the load frame is insignificant compared to that of the specimen [57].

$$\delta_{corrected} = \tan^{-1}\left(\frac{C_{contact}\omega}{K_{contact} - m\omega^2}\right)$$

Equation 5.3 The corrected phase angle that subtracts the contributions from the instrument's actuator and physical damping from the load frame [57].

$$C_{contact}\omega = \frac{f_0}{h_0} sin\delta\Big|_{coupled} - \frac{f_0}{h_0} sin\delta\Big|_{free\ space}$$

Equation 5.4 The out-of-phase component of the imposed harmonic oscillation [57].

$$K_{contact} - m\omega^2 = \left[\frac{1}{\frac{f_0}{h_0} cos\delta\Big|_{coupled} - \frac{f_0}{h_0} cos\delta\Big|_{free\ space}} - \frac{1}{K_{lf}}\right]^{-1}$$

Equation 5.5 The in-phase component of the imposed harmonic oscillation [57].

Where $f_0/h_0|_{coupled}$ is the apparent power of the actuator and specimen, $f_0/h_0|_{free\ space}$ is the apparent power of the actuator hanging in free space, K_{lf} represents the stiffness of the load frame (taken to be $1.59*10^6$ N/m) [143], $K_{contact}$ is the stiffness of the contact between the indenter tip and sample, $\delta_{corrected}$ represents the phase angle of the sample, $C_{contact}\omega^2$ represents the lag and $K_{contact} - m\omega^2$ represents the in-phase components of the imposed oscillation required for the CSM technique. This summarizes the framework that will give credence to the phase angle data obtained for the nanoporous samples of interest.

The validation experiments, shown in Figure 5.1, were performed on fused silica and PMMA because both materials exhibit well-known phase angle behavior. The true phase angle values for fused silica and PMMA, when measured at room temperature and 45 Hz, are quoted in the literature as 0° and 3.4°, respectively [57, 144, 145]. Each phase angle value falls well within the range of one standard deviation about the average experimental phase angle at 45 Hz. Moreover, measured and corrected values are nearly identical when plotted as a function of frequency, indicating the reference phase angle is accurate. This demonstrates that the modified CSM technique can achieve steady-state harmonic motion, that the measured phase angle is not influenced by shifts resulting from

the displacement electronics, and that the phase angle of the specimen dominates the response. It is also observed in Figure 5.1 that the average phase angle value for fused silica is closer to the true value at frequencies higher than 45 Hz. This likely results from the nanoindenter's ability to better achieve steady-state harmonic motion when the change in contact area is insignificant over the time scale of the measurement [57]. For this reason, the results for np Si-Mg thin films tested in this study are reported at frequencies of 70 Hz.

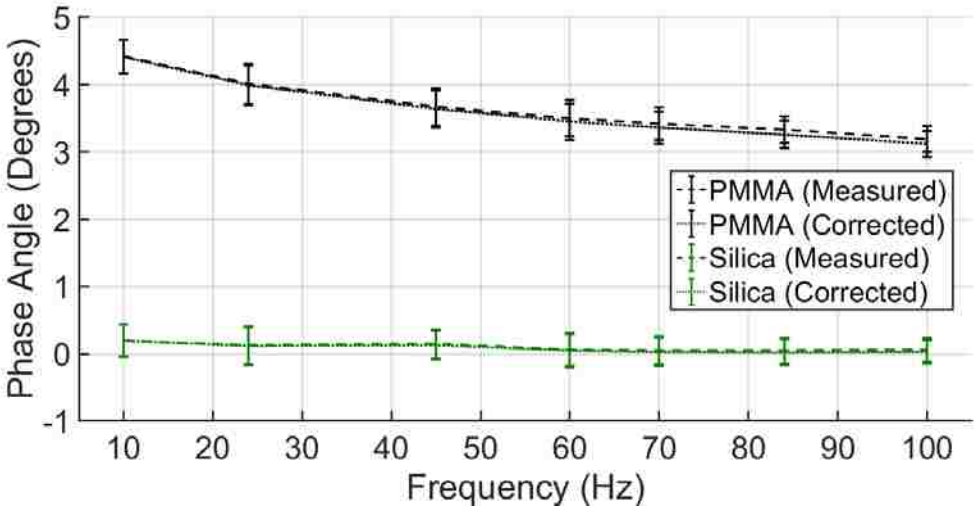

Figure 5.1 Proof-of-concept plot showing measured and corrected values for both a known linear elastic solid (fused silica) and a known linear viscoelastic solid (PMMA). This demonstrates that the reference phase calibration built into the software accounts for shifts associated with displacement electronics.

5.3.2 Time-Dependence in the Time Domain

Representative load-depth curves of PMMA, np Si-Mg, and silica are shown in Figure 5.2. The key features of these plots are circled at the summit and base of the curves. The plateau near the top of each load-depth curve represents material creep during a 60-second hold period. Of course, material creep is convoluted with transient drift effects [54]. [54] Instrument drift was measured after nearly complete unloading, denoted by circled regions near the base of the curves. The extent to which the known viscoelastic solid

PMMA creeps during the 60-second hold period is approximately 22 nm, and a similar 22 nm recovery is also observed at the base of the curve after unloading (Figure 5.2a). It is imperative to compare the values obtained on PMMA to those for the known linear elastic solid fused silica, to determine how much of the 22 nm displacement can be attributed to transient drift effects, which in this case is 3-5 nm (as indicated by the circled region near the base of the curve in Figure 5.2c). Similarly, np Si-Mg sample creep was ~11 nm during the 60-second hold period (Figure 5.2b), and transient drift was assumed to account for 3-5 nm. These experiments were performed under identical conditions and indicate that np Si-Mg and PMMA exhibit some level of time-dependence, unlike fused silica. Moreover, PMMA appears to have a slightly greater time-dependence than np Si-Mg. It is noted that PMMA recovers almost the entire 22 nm displacement (from the creep period) during subsequent measurement of drift near the base of the curve, whereas np Si-Mg shows negligible recovery. Since PMMA is a known viscoelastic solid, it stands to reason that it would recover fully at low loads. The observation that np Si-Mg does not exhibit significant recovery implies that its time-dependence stems largely from plasticity. Therefore, an appropriate model to describe the mechanical behavior of np Si-Mg should incorporate both time-dependent plasticity and viscoelasticity, as in the viscous-elastic-plastic (VEP) model developed by Oyen [56, 146, 147]. However, further investigations would be required to understand the mechanism(s) of deformation.

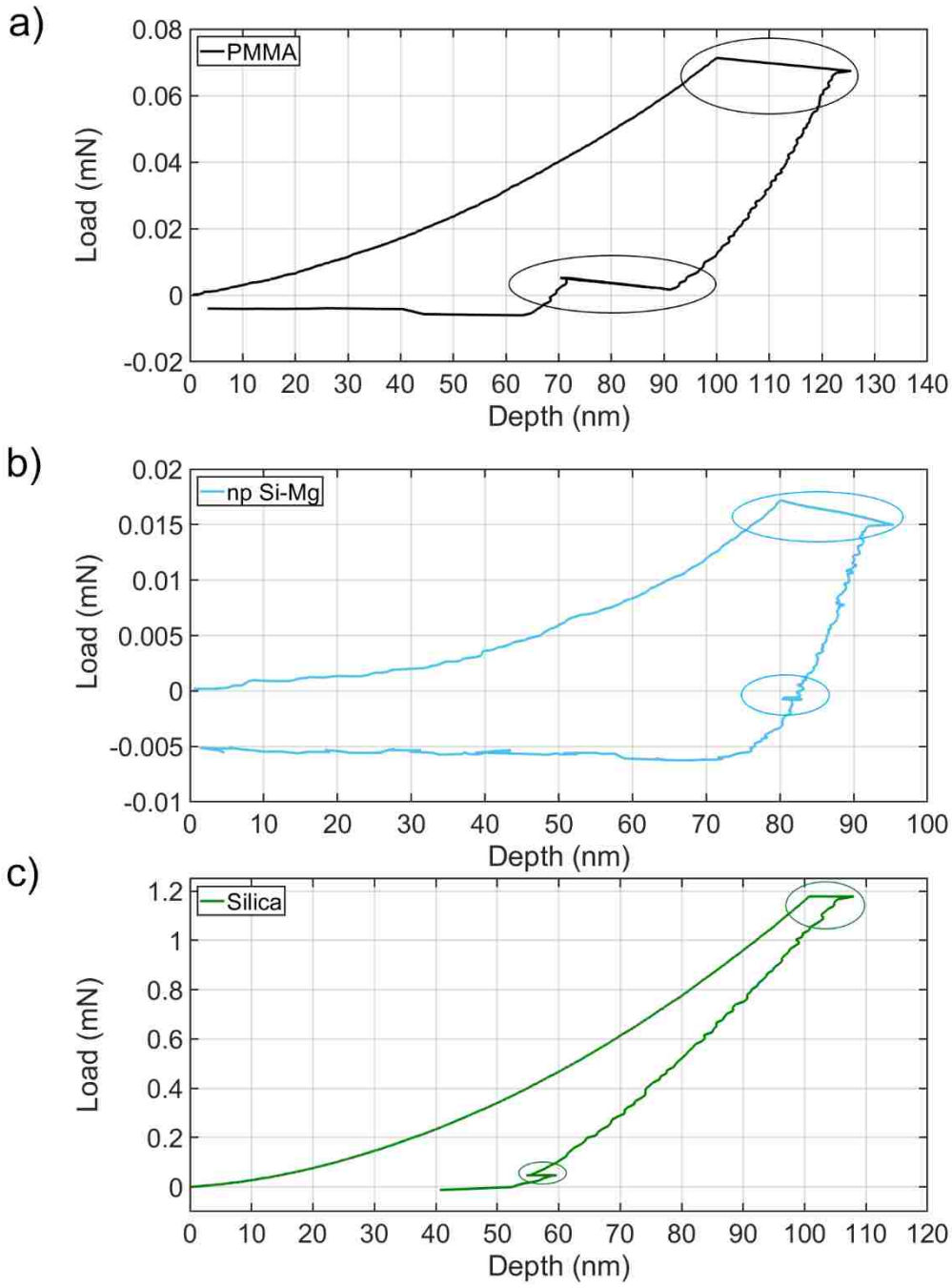

Figure 5.2 Mechanical response of reference materials and np Si-Mg, measured in the time domain. The response of (a) PMMA is compared to that of (b) np Si-Mg and (c) fused silica at similar depths and under the same experimental conditions, such that transient effects are comparable between tests. PMMA and np Si-Mg exhibit time-dependence, while fused silica does not.

5.3.3 Time-Dependence in the Frequency Domain

There are two domains in which a nanoindentation experiment can be performed, namely the time domain and the frequency domain, each with inherent advantages and disadvantages [54]. Thermal drift is a major obstacle to testing in the time domain – as in the case of creep. However, a major advantage to operating in the frequency domain is that sample stiffness and damping are unaffected by transient effects – as in the case of the modified CSM technique. As such, the phase angle values reported in Table 5.1 are true quantitative measurements of damping capacity for the materials tested. The quantitative results in Table 5.1 corroborate the qualitative results in Figure 5.2, and indicate that PMMA exhibits more damping than np Si-Mg.

The ratios of $\frac{f_0}{h_0}\Big|_{coupled}$ to $\frac{f_0}{h_0}\Big|_{free\ space}$ and K_{lf} to $K_{contact}$ are shown in Table 5.1 for the np Si-Mg tested in this study, and show that Equation 5.1 and Equation 5.2 hold true in each case. These conditions must be satisfied if the instrument's contribution to the measured phase angle is to be neglected [57]. The percent difference between $\delta_{measured}$ and $\delta_{corrected}$ is also shown in Table 5.1. The results for PMMA and fused silica support the results shown in Figure 5.1. There is a larger percentage difference between the measured and corrected values for the np Si-Mg samples because the depth (and consequently the contact area) at which the phase angle measurements were obtained are smaller. This underscores the importance of correcting for shifts in displacement electronics as the contact dimensions approach zero and Equation 5.3 - Equation 5.5 are used [57].

Table 5.1 Relevant values in the calculation of energy dissipated by the materials tested at a frequency of 70 Hz. The damping capacity of np Si-Mg lies between that of fused silica and PMMA.

	Fused Silica	PMMA	As-dealloyed np Si-Mg	Dealloyed/annealed np Si-Mg
$\frac{\frac{f_0}{h_0}\Big\vert_{coupled}}{\frac{f_0}{h_0}\Big\vert_{free\ space}}$	1000	453	23.7	25.5
$\frac{K_{lf}}{K_{contact}}$	9.81	22.9	552	571
$\delta \pm \sigma$	0.0 ± 0.2	3.3 ± 0.2	1.9 ± 0.5	2.6 ± 1.4
$\frac{(\delta_{measured} - \delta_{corrected})}{\delta_{measured} - \delta_{corrected}/2}$	≈ 0%	1.8%	36%	18%

5.3.4 Elastic Modulus and Hardness of Nanoporous Si

Representative load-displacement curves, reduced modulus (E_r) and hardness of the np Si-Mg films are shown in Figure 5.3. It is well-known that modulus and hardness data obtained on materials that exhibit time dependence are subject to error due to pile-up around the indenter [37]. Conveniently, there exists an easily obtainable experimental parameter that can be used to estimate the extent to which pile-up affects the contact area, namely the ratio h_f/h_{max} [37]. Here, h_f represents the final indentation depth and h_{max} represents the depth at peak load. A material with h_f/h_{max} ratio near unity exhibits completely plastic behavior, and materials near zero are fully elastic. In terms of contact area, however, materials with a ratio >0.7 could be subject to underestimating the contact

area due to pile-up. The load-displacement curves in Figure 5.3 a) indicate h_f/h_{max} ratios of 0.80 and 0.86 for as-dealloyed and annealed np Si-Mg, respectively. Depending on the amount of work-hardening, the contact area is likely underestimated slightly. This indicates that the modulus and hardness values reported in Figure 5.3 b) and Figure 5.3 c) could be somewhat overestimated. It should be noted, however, that this ratio is normally applied to solid materials, i.e. non-porous. The mechanism leading to an inflated ratio is typically explained as pile-up around the indenter tip, in the context of solid materials. For porous materials, however, the mechanism is more likely densification than pile-up, as this is a well-documented phenomenon to occur during indentation of porous materials [41, 46, 50, 148, 149]. Nevertheless, the effect on the modulus and hardness are the same as it would be if the contact area were underestimated; modulus and hardness are slightly overestimated.

There is a well-defined plateau in E_r values for both as-dealloyed and annealed np Si-Mg films, but there is greater variability in E_r of the annealed sample. Average values for E_r are 5.78 GPa and 11.87 GPa for as-dealloyed and annealed np Si-Mg, respectively. Typically, the modulus of the film dominates the elastic response of the film-substrate system at depths less than 10% of the film thickness, corresponding to ~100 nm in this case, after which the modulus approaches that of the substrate [46, 50]. This is confirmed by a gradual increase in modulus at depths larger than 100 nm, shown in Figure 5.3 b). The microstructure of the np Si-Mg films were described previously by Maxwell *et al*. and show that nanocrystals form after vacuum annealing [125]. This could make annealed samples more heterogeneous throughout the film thickness and explain the higher variability of E_r. Moreover, localized nanocrystals act to increase the average stiffness

response on unloading [150]. The increased modulus of the annealed film is not the result of film densification upon annealing. The as-dealloyed film does contract by about 11% after annealing, which corresponds to an increase in relative density and influences the modulus per the Gibson and Ashby relation [45, 151]. This increase in modulus that results from the increase in relative density dwarfs in comparison to the measured increase in reduced modulus, indicating this is a true material property and not the result of a slight relative density increase. Moreover, if the film had contracted considerably, one would observe the onset of a substrate effect for the annealed film at much lower values than observed for the as-dealloyed film. The hardness values of the two samples, however, plateau at depths greater than 100 nm. The authors report the hardness to be 167 MPa and 250 MPa for as-dealloyed and annealed np Si-Mg, respectively. Hardness measurements of soft films on hard substrates are accurate at depths up to 50% of the film thickness [46, 148]. The hardness values here are accurate and constant up to the point of maximum indentation depth (300 nm), which is less than half the film thickness.

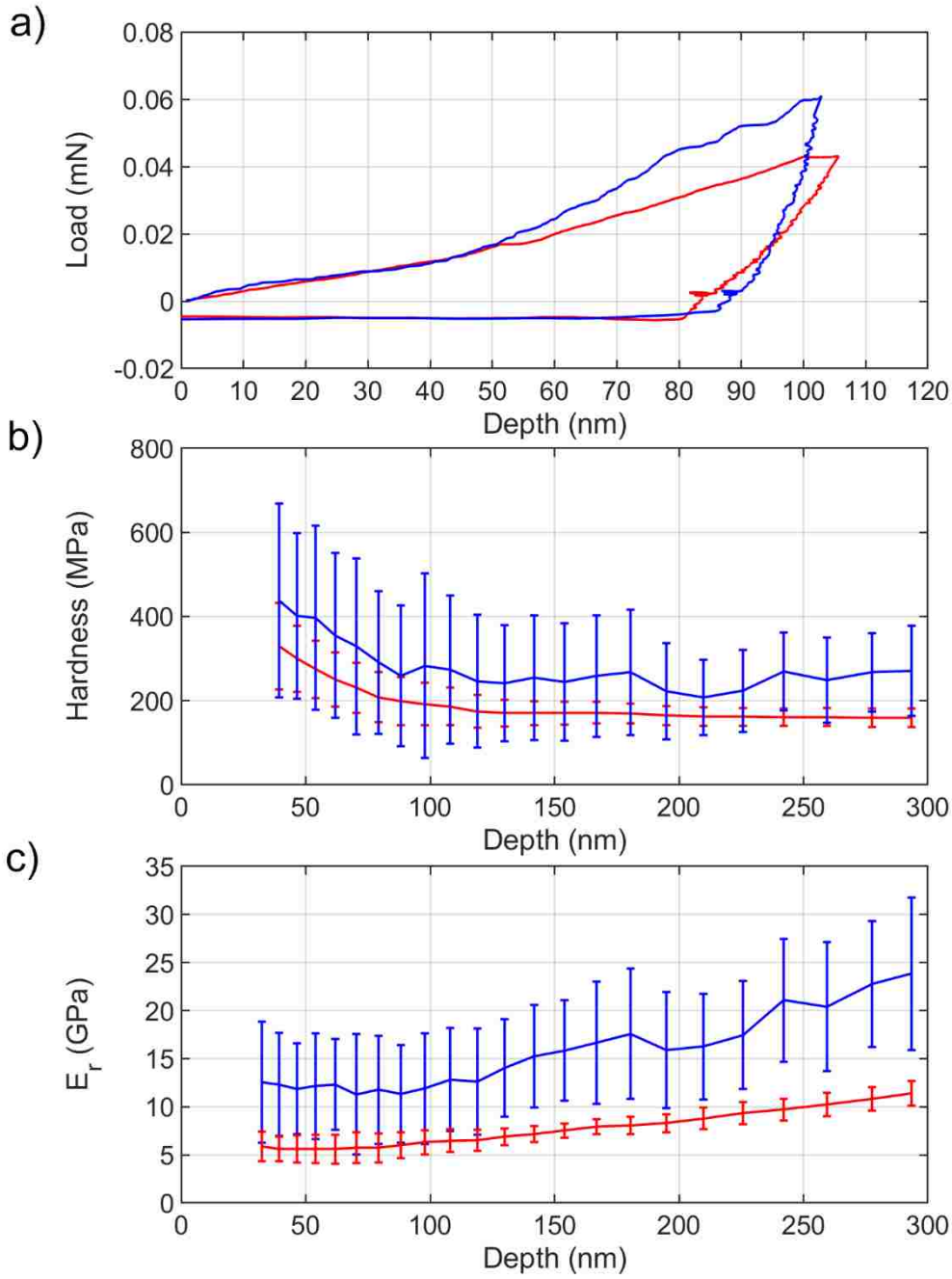

Figure 5.3 The load-displacement curves in a) show that both the annealed (blue) and as-dealloyed (red) films exhibit significant plasticity as determined by the h_f/h_{max} ratio. The hardness in b) and the reduced modulus in c) were obtained using the CSM technique. There is a plateau in the reduced modulus at depths less than 100 nm, that reflects the material modulus of the np Si-Mg films. After the 100 nm mark, the reduced modulus values begin to inflate, indicating the presence of the silicon substrate. The hardness shows plateaus at depths greater than 100 nm, which is reasonable for a soft film on a hard substrate.

5.4 Conclusions

This study has addressed the mechanical response of nanoporous Si-Mg films, which were fabricated using free-corrosion dealloying and which represent an intriguing form of silicon that may find use as an anode material in lithium-ion batteries. The porous thin film samples, in both the as-dealloyed and annealed states, were designed to have a final thickness of ~ 1 μm, such that the substrate effect could be avoided during mechanical characterization in both the time and frequency domains. The as-dealloyed and annealed samples were investigated using a modified continuous stiffness measurement technique that optimized the ability to achieve steady-state harmonic motion, such that accurate phase angle measurements were obtained; the as-dealloyed and annealed samples exhibit distinct phase angle measurements of 1.9° and 2.6°, respectively. Observations made in the time domain suggest that the time-dependence of nanoporous Si-Mg stems largely from plasticity. The reduced modulus values of as-dealloyed and annealed samples were investigated using the continuous stiffness measurement technique and had corresponding values of 5.78 and 11.87 GPa, respectively. Similarly, the hardness of as-dealloyed and annealed samples were 167 MPa and 250 MPa, respectively.

6 A Fundamental Study of W-Al Alloying

6.1 Introduction

Tungsten is a refractory metal that boasts a melting point of approximately 3400°C and has a wide range of industrial applications including radiation shields, filaments, welding, counter weights, and electrochromics [152-157]. Alloying elements with tungsten can be used to tailor the material for specific applications like machining or wear resistance [158]. As such, alloying aluminum with tungsten can improve the mechanical behavior and corrosion resistance or be used as a more benign alternative to beryllium-tungsten coatings in nuclear fusion devices [159-162].

There are a variety of techniques in the literature to produce W-Al alloys including: ball milling, physical vapor deposition, high-current pulsed electron beam irradiation and electrodeposition [161, 163-165]. Typically, the alloying of W-Al is carried out using non-equilibrium processes because the two metals have dissimilar melting points, thereby making it difficult to create through traditional melting or arc melting. In other words, non-equilibrium processes are advantageous because they allow researchers to study the single phase solid solution of W-Al alloys that the equilibrium phase diagram would otherwise preclude [166].

It is well known that predicting the lattice change of a solid solution purely from the linear relation - commonly known as Vegard's law – is often found to be in error [167-170]. In 1966, King published an article that shows Vegard's law is only applicable for small concentrations of solute atoms in a metallic solid solution of binary alloys [171]. The findings of the report show that for metallic solid solutions, there exists a concentration

above which the linear trend is no longer applicable, c_{max}. This departure from linearity was postulated to be the result of significant charge transfer to/from the solute atom upon alloying. Vegard's law was discovered to apply for ionic salts where the electronic environment remained unaltered when one atom was replaced with another of equivalent charge [170, 171]. In binary metallic systems, it is seldom observed that the electronic environment is preserved after significant alloying has occurred [171-173].

The publications on W-Al alloying in the literature typically investigate the corrosion behavior and/or the mechanical properties in alloys where aluminum is the major constituent [160, 161, 163-165, 174-180]. The current study focuses on the physical vapor deposition of W-Al at small concentrations of Al, ranging from 0 – 14.5 at.% Al. Small changes in lattice parameter are characterized in x-ray diffraction (XRD) as aluminum is added to the tungsten matrix and does not change as one might expect based on Vegard's Law. This is discussed at length in the context of density functional theory (DFT) calculations, x-ray photoelectron spectroscopy (XPS) binding energy shifts, Bader analysis, and changes in electron work function (EWF). To the authors knowledge, this composition range of W-Al alloys has yet to be investigated.

6.2 Experimental Details

6.2.1 Film Deposition

Gradient films of W-Al were co-deposited via magnetron sputtering (ORION system, AJA International, Inc.) onto (001)-oriented, phosphorus doped single crystal silicon wafers (Virginia Semiconductor). Prior to deposition of the W-Al film, a thin layer of tantalum was deposited to promote adhesion between the film and substrate. All depositions were carried out in an atmosphere of argon. The W-Al gradient film was

deposited at a pressure of 6.0 x 10^{-1} Pa (4.5 x 10^{-3} torr). The base pressure of the sputtering system before film deposition was 1.3 x 10^{-5} Pa (1 x 10^{-7} torr). A film of tungsten was also sputtered under the same conditions as stated above to act as a reference material. The W-Al films were deposited on rectangular silicon stubs of approximately 1 cm x 1.5 cm. The stubs were aligned side-by-side across the substrate carrier for deposition. The tungsten and aluminum targets were diametrically opposed and the substrate carrier was not rotating, such that a composition gradient was achieved. Eight silicon stubs were used in total for the gradient.

6.2.2 Characterization

Energy dispersive spectroscopy (EDS) measurements of the as-deposited gradient films were performed in an FEI Quanta 250 FEG SEM equipped with an Oxford Instruments EDS system (X-MaxN 50 mm^2 detector).

XRD experiments were performed with a Bruker D8 AXS Discover equipped with a semi-automatic z-height stage for precision sample positioning. Samples were scanned from 30° to 90° (2θ) in 0.02° steps at 1°/minute. Additionally, in order to obtain smoother peaks for precise location of those peak positions, certain angular ranges were scanned more slowly: from 35° to 50° (2θ) and 70° to 90° (2θ) in 0.02° steps at 0.5°/minute. The positions of the diffracted peaks in the XRD scans were determined using commercial software (EVA) provided by Bruker. It should be noted that none of the XRD scans were smoothed during the data analysis process.

Surface analysis of the gradient samples was completed with a Thermo Scientific K-Alpha XPS, equipped with a monochromatic Al-Kα X-ray source with a spot size of 400 μm. The base pressure of the XPS was 1 x 10^{-7} Pa (7.5 x 10^{-10} torr). All spectra were

calibrated against an energy value of 285 eV for adventitious carbon. All XPS peaks were fit with mixed Gaussian-Lorentzian curve fitting software with “smart” backgrounds. XPS energy resolution is 0.1 eV.

The EWF of the deposited films was measured using a Kelvin probe (KP Technology, Ltd.) that utilizes the contact potential difference (CPD) to obtain EWF values. The CPD method vibrates a metallic tip of known work function value in close proximity to another, dissimilar material surface, and determines the relative work function difference between the two materials. The EWF of the unknown material surface is calculated according to: $eV_{cpd} = e(\Phi_{KP} - \Phi_M)$ [94]. V_{cpd} is the contact potential difference between the two materials, Φ_{KP} is the work function of the Kelvin probe tip, Φ_M is the work function of the unknown material, and e is the charge of an electron. The experiments were performed in a vacuum chamber at pressures lower than 6.7×10^{-5} Pa (5×10^{-7} torr). At least 100 EWF measurements were obtained and averaged for each sample. This resulted in a standard deviation of ~10 meV for each measured EWF value.

The indentation experiments were performed with an iMicro load frame in conjunction with an iNano actuator (Nanomechanics, Oak Ridge, TN). Calibration of the Berkovich tip (Microstar Tech, Huntsville, TX) area function was carried out on a manufacturer provided fused silica reference block. The samples of interest were mounted to aluminum pucks with Crystal Bond (SPI Supplies, West Chester, PA). Sixteen indents were performed on each sample in a 4 x 4 array where the distance between adjacent indents was at least 30 times the indentation depth. Since the films were all on the order of 100 nm in thickness, a substrate deconvolution test method was used to obtain the elastic modulus of the W-Al films [36].

6.2.3 Computational Methods

All computational results reported here were calculated based on density functional theory (DFT), performed using the Vienna *Ab initio* Simulation Package (VASP) [181]. The pseudo-potentials used are Perdew-Burke-Ernzerhof (PBE) formalism of the generalized gradient approximation (GGA) [182] with electronic configurations of W ($5p^6$ $6s^2$ $5d^4$), and Al ($3s^2$ $3p^1$). For structure and energy calculations, a *k*-point mesh of about 30 x 30 x 30, or equivalent, for BCC W, was used for density of states (DOS) calculations. The plane-wave cutoff energy of 420 eV was used to achieve numerical convergence of 1 meV/atom in energy. The valence charges of W and Al ions were calculated using the Bader charge analysis method [183]. The calculated diffraction pattern was obtained through the VESTA program [184] for structures from DFT calculations.

6.3 Results and Discussion

6.3.1 Preliminary Results

The motivation for studying the W-Al system with small concentrations of aluminum dissolved in the tungsten matrix arose from investigations that were first performed on a scandate cathode of excellent emission behavior. Initially, I had performed XPS scans of the scandate cathode and in interpreting those scans found that the binding energy associated with elemental tungsten to have peak values lower than what one would expect. The peaks typically observed when scanning for tungsten are the 4f 7/2 and 4f 5/2 peaks, sometimes referred to as a doublet. After charge correcting by using the value of 285 eV for adventitious carbon, the W 4f 7/2 peak appeared at 30.78 eV and the W 4f 5/2 peak at 32.88 eV, as shown in Figure 6.1 a). When comparing to the NIST database, which has an extensive list for various reports of different materials, the lowest value reported for

the W 4f 7/2 peak and W 4f 5/2 peak was 30.90 eV and 33.00 eV, respectively. The shift is not extreme, but it is enough to be significant. When performing the XPS scan on the scandate cathode, I also scanned for Ba, Sc, Al and O; all of which had reasonable peak binding energy values. It was not until later, when my colleague had performed a cross-section on the scandate cathode with the FIB and performed an EDS line scan that we were able to further interpret these results.

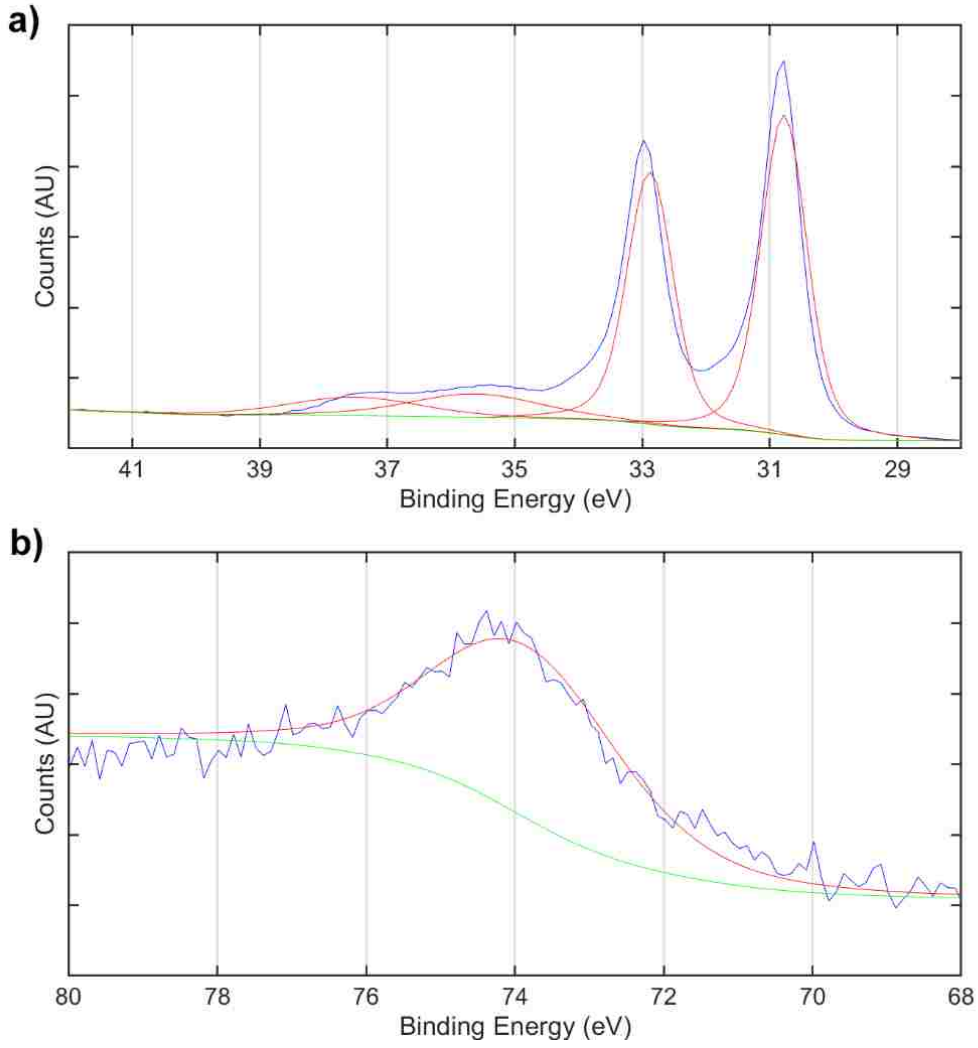

Figure 6.1 These are XPS scans of a scandate cathode that exhibited excellent emission behavior. The scans were charge corrected for adventitious carbon to a value of 285 eV. The blue lines represent the raw data, the red lines represent the respective peak fits, and the green line represents the background. a) is the scan range for W4f binding energy and b) is the scan range for Al2p binding energy.

My colleague had obtained a milled cross-section of a representative tungsten grain from the scandate cathode, as shown in Figure 6.2. The circular region attached to the solid white line in Figure 6.2 a) shows where the EDS line scan began, which occurred outside the representative tungsten grain. The 300 nm mark and greater in Figure 6.2 c) corresponds to the region on the inside of the representative tungsten grain. It is easy to see

where the tungsten grain begins in Figure 6.2 b) because it looks very bright since this was a backscatter electron image. In general, elements with high atomic number will appear bright, so it gives a qualitative map of elemental atomic number. The important thing to note here is that there appears to be a significant amount of aluminum inside the tungsten grain. This was an unexpected result, but seems to indicate that the tungsten is actually alloyed with aluminum.

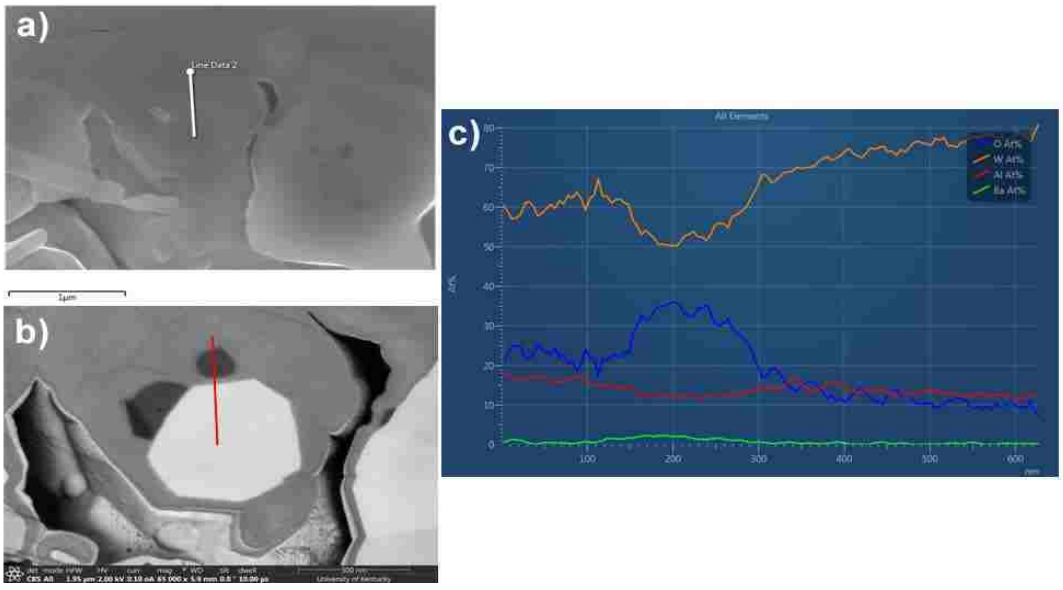

Figure 6.2 a) and b) represent milled cross-sections of a scandate cathode of excellent emission behavior, while c) corresponds to the chemical composition obtained from the marked EDS line scan. The 0 nm starting point in c) corresponds to the circular region that attaches to the straight line in a). a) is a secondary electron micrograph whereas b) is a backscatter image.

At first it was difficult to interpret the XPS binding energy shifting of the W 4f 7/2 and W 4f5/2 to lower values without further characterization. After seeing the EDS line scan results in Figure 6.2, it implies that the tungsten could be alloyed with aluminum in concentrations up to 15 at.%-Al. If the tungsten and aluminum were to create a homogeneous solid solution, it could explain why the binding energy of tungsten appeared to be lower than expected. That was the motivation for studying the W-Al thin film system.

Moreover, the creation of W-Al thin films provides an opportunity to isolate a component of the scandate cathode and study it individually.

6.3.2 Crystal Structure and Atomic Volume

The compositions of the eight W-Al gradient films were determined using EDS, and ranged from 1.4 to 14.5 at.% Al. The crystal structure at each location of the gradient film is inferred from the XRD patterns in Figure 6.3. In Figure 6.3 a), it is observed that all gradient films are single phase, despite the different crystal structures of pure tungsten (BCC) versus pure aluminum (face-centered cubic, FCC). Based on the W-Al equilibrium phase diagram (shown in Figure 6.4), the single-phase BCC region should extend to only a few at.% Al at 300 K [166]. However, using a non-equilibrium film deposition technique in the current study resulted in a single-phase BCC structure that was observed to extend from pure tungsten to at least 14.5 at.% Al, forming a supersaturated solid solution of Al in W.

High-resolution XRD scans of the W-Al gradient films and the pure tungsten film are shown in Figure 6.3 b) and Figure 6.3 c). In Figure 6.3 b), diffraction from the (011) planes are observed to occur at approximately 40°. However, diffraction from the (112) and (022) planes occur at approximately 73° and 87°, respectively in Figure 6.3 c). In each of the subplots of Figure 6.3, the XRD scans have been arranged in ascending order according to the aluminum content within each film. It should be noted that the scan associated with the pure tungsten film only appears in Figure 6.3 b) and Figure 6.3 c).

As seen in the high-resolution XRD scans of Figure 6.3 b) and Figure 6.3 c), the peak positions in the various films shift as a function of Al content. It was observed that as Al content increases, the diffraction peaks shift to higher values of 2θ. The shift is small

when comparing adjacent films in the gradient, but the overall shift across the composition range is significant and a clear trend is exhibited in Figure 6.5.

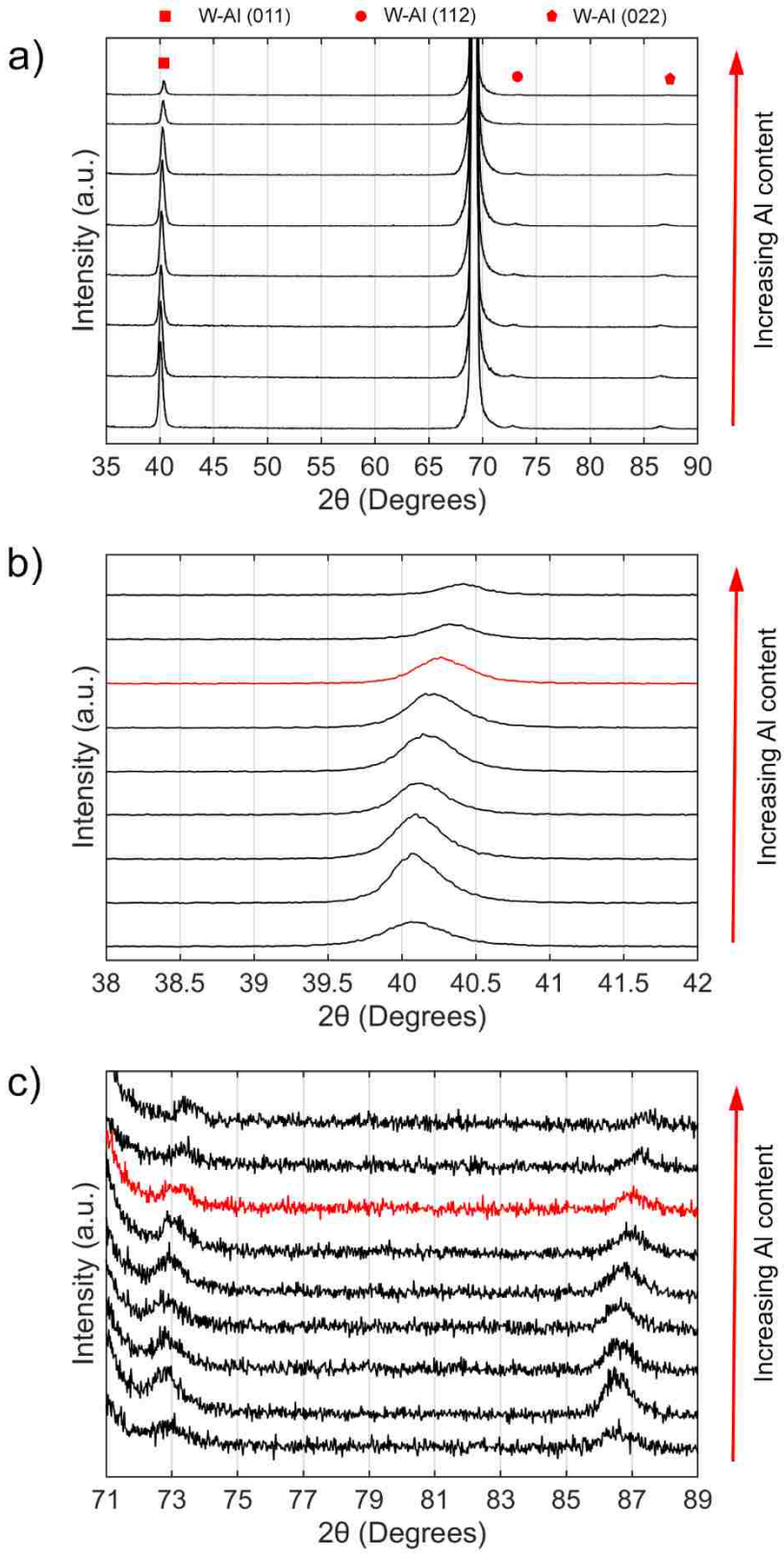
a)
W-Al (011)
W-Al (112)
W-Al (022)
Intensity (a.u.)
35 40 45 50 55 60 65 70 75 80 85 90
2θ (Degrees)
Increasing Al content
b)
Intensity (a.u.)
38 38.5 39 39.5 40 40.5 41 41.5 42
2θ (Degrees)
Increasing Al content
c)
Intensity (a.u.)
71 73 75 77 79 81 83 85 87 89
2θ (Degrees)
Increasing Al content

Figure 6.3 XRD scans of the gradient and pure tungsten films. a) Diffraction scans of the eight W-Al gradient films. All films exhibit a single-phase BCC structure. b) and c) are high-resolution scans of the W-Al gradient films, as well as the pure W film for reference, over shorter angular ranges. The large peak at approximately 69° 2θ in a) is from the Si wafer that serves as the film substrate. The XRD scan in b) and c) that is plotted in red represents the scan that corresponds to c_{max}, as determined in the current study and discussed in more detail below.

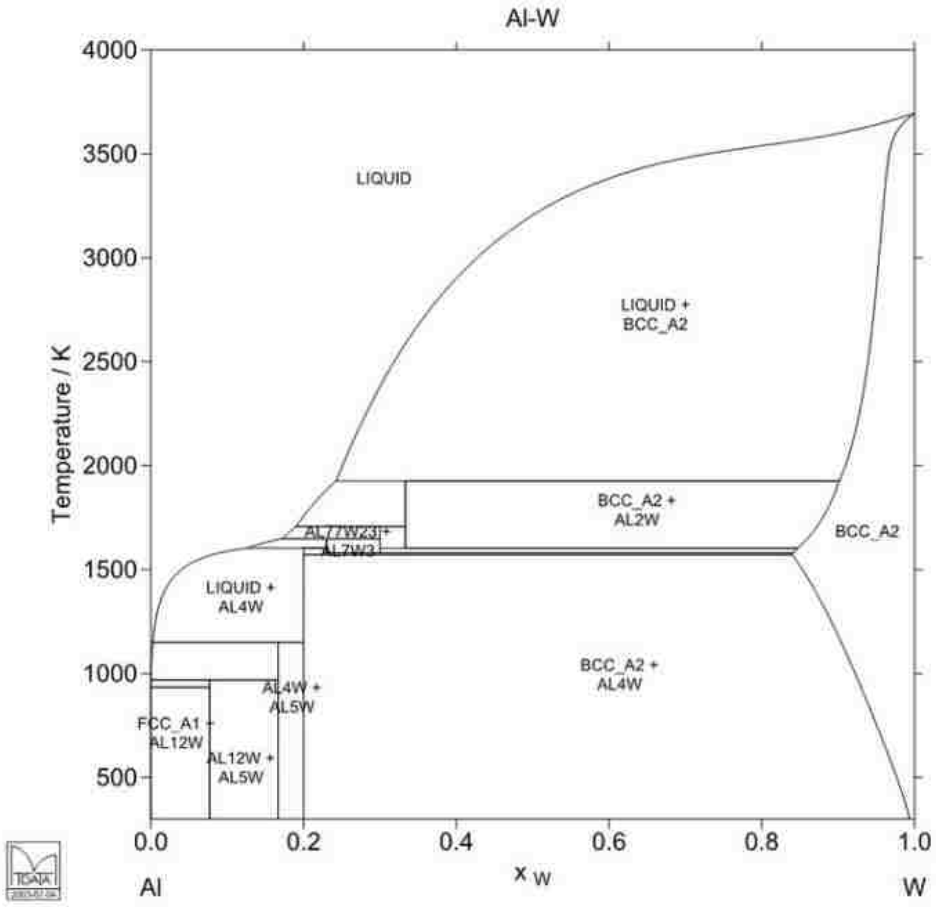

Figure 6.4 The W-Al phase diagram [166].

The atomic volume, Ω, is defined as the mean volume per atom [171]. For a given alloy, this is the volume of the unit cell divided by the number of atoms per unit cell. It was observed by King that when plotting Ω as a function of atomic concentration of solute atoms, the trend varies linearly up to a limiting concentration (c_{max}) before departing from linearity, particularly for binary metallic systems. The linear portion typically corresponds

to Vegard's Law. However, when the linear portion varies significantly from Vegard's Law, that is taken as evidence that the electronic environment of the solute atom has not been preserved upon alloying [171]. Moreover, deviations from linearity are taken as evidence that the electronic environment of the solvent atom has been perturbed.

In Figure 6.5, the atomic volume of each sputter-deposited film is plotted as a function of Al content, $\Omega(c_{Al})$. For comparison, the values of $\Omega(c_{Al})$ as calculated by DFT are also included. These calculated values are in good agreement with the experimentally determined values over the range of film compositions, with a maximum difference of ~1.5% for the highest Al content. The atomic volume is seen to decrease as Al content increases. This result is counter-intuitive when considered from the perspective of Vegard's Law, where the solute and solvent atoms are treated as spheres [185]. This is because aluminum has a larger metallic radius than tungsten, as described below.

It is well known that the atomic radius of an atom depends on the coordination number. Atoms with a coordination number of 8, 6 and 4 will have an atomic radius that is approximately 3, 4 and 12% smaller than for atoms a coordination number of 12 [186]. For an appropriate comparison of the atomic radii between aluminum and tungsten, the coordination number should be 8 since the structure being studied is BCC. The atomic radius for tungsten (coordination=8) is 137 pm and the atomic radius for aluminum (coordination=8) is 139 pm.

King surveyed 469 metallic solid solutions using precise lattice parameter data in the literature and discovered that when the solute atom was smaller than the solvent atom, the atomic volume change was always opposite to what one would expect based on Vegard's Law. Similarly, when the solute atom was larger than the solvent atom, the sign

of the atomic volume change was opposite to what one would expect for about half of the metallic solid solutions. In the W-Al alloy system, the solute atom is larger than the solvent atom, and the atomic volume decreases with increasing Al content, i.e. the trend is inconsistent with Vegard's Law. As discussed below, this is attributed to hybridization between the W-5d and Al-3p orbitals, which also results in charge transfer.

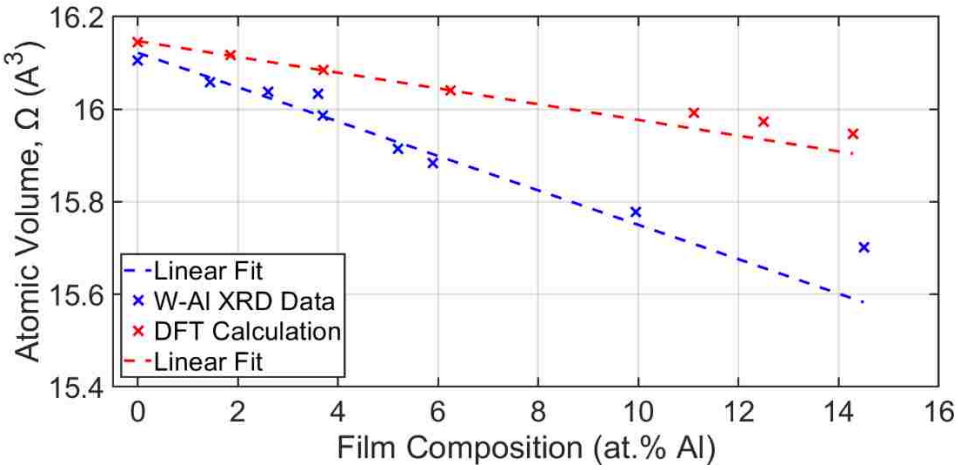

Figure 6.5 Atomic volume of each W-Al alloy, plotted against film composition. The experimental data (obtained with XRD) and the theoretical data (from DFT calculation) are in good agreement. There are two remarkable features in the plot: 1) the rate of change in the plot is linear up to a concentration of approximately 6 at.% Al, and 2) the slope of each plot is negative. This implies that Vegard's Law does not describe the observed changes in atomic volume. Instead, these result from complex charge transfer and orbital hybridization.

6.3.3 Modifications in Electronic State with Alloying Additions of Al

Partial density of states (pDOS) plots for the W-5d and the Al-3p orbitals are shown in Figure 6.6 with various concentrations of Al solute. It is instructive to use the pDOS plots, as well as the Bader charge analysis, to support the conclusions drawn from the atomic volume plot. The pDOS plots in Figure 6.6 show that there is significant overlap between the valence orbitals of both tungsten and aluminum across the entire composition range studied. A Bader charge analysis was performed to compute the energetically most

stable electron configuration for the resulting alloys [183, 187]. Based on the Bader charge analysis, shown in , it is apparent that the electronic environment of the aluminum (solute) atoms is not preseserved upon alloying. This is taken as direct evidence to support the results shown in Figure 6.5 where the atomic volume drastically differs from what is predicted based on Vegard's Law. Moreover, the electronic environment of the tungsten (solvent) atoms is significantly altered above c_{max}, which corresponds to a gain in electrons for an average W atom of approximately 0.183. In short, electrons are transferred from Al atoms to W atoms across the entire alloying range of interest.

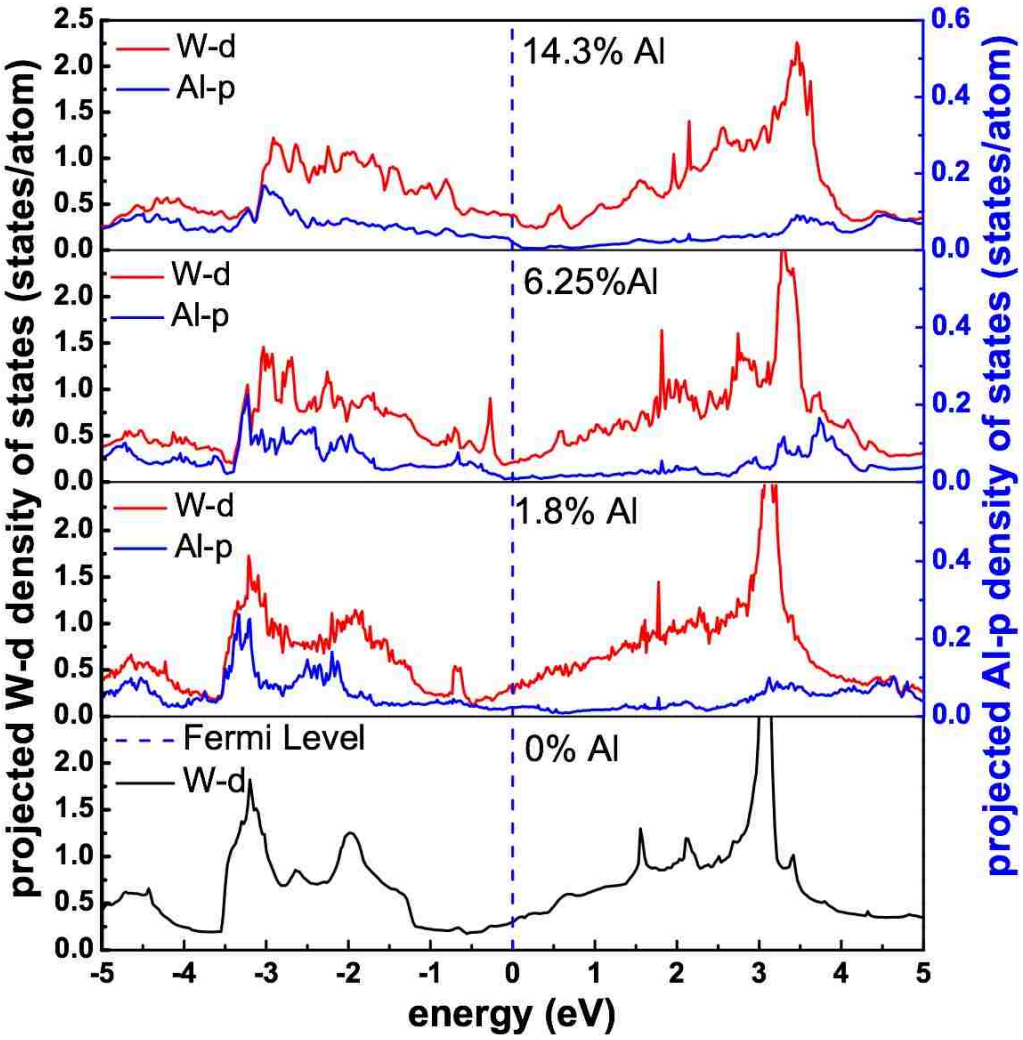

Figure 6.6 pDOS plots for the W 5d and Al 3p orbitals of both tungsten and aluminum, covering a composition range where Al content varies from 0 to 14.3 at.%. For all Al concentrations computed here, the W 5d and Al 3p orbitals overlap. The Fermi level is indicated by the dotted line at 0 eV.

Table 6.1 This table represents the numerical results from the Bader analysis that was used to show that charge is being transferred between the W-5d and Al-3p valence orbitals.

Film Composition (at. % Al)	W Valence Charge Gain (e-/atom)	Al Valence Charge Loss (e-/atom)
0	0	N/A
1.85	-0.0489	1.67
3.70	-0.0988	1.65
6.25	-0.183	1.76
11.1	-0.320	1.64
12.5	-0.364	1.64
14.3	-0.428	1.65

It is known that BE shifts of core electrons can be related to physical differences in the atoms under investigation [188-191]. The physical difference most often credited with BE shifts of core electrons stems from charge transfer, which results in differences in charge density on the atoms under investigation [188-191]. The Bader analysis shows that charge is being transferred from the Al-3p valence orbital to the W-5d valence orbital and one would expect that as the charge density on an average tungsten atom gets larger with alloying additions of aluminum, that the core level BE of tungsten would decrease [190, 191]. This is shown in Figure 6.7, where the W-4f core level BE decreases with increasing charge density in the tungsten valence. This BE shift can therefore be thought of as a result of charge density differences that results from charge being transferred from the aluminum valence to the tungsten valence upon alloying. This has foundations in simple electrostatics

and can be thought of as the energy required to create a core hole inside a conducting spherical shell [190]. In other words, it is easier to remove an electron from the inside of the charged spherical shell the greater the negative charge on the surface of the sphere.

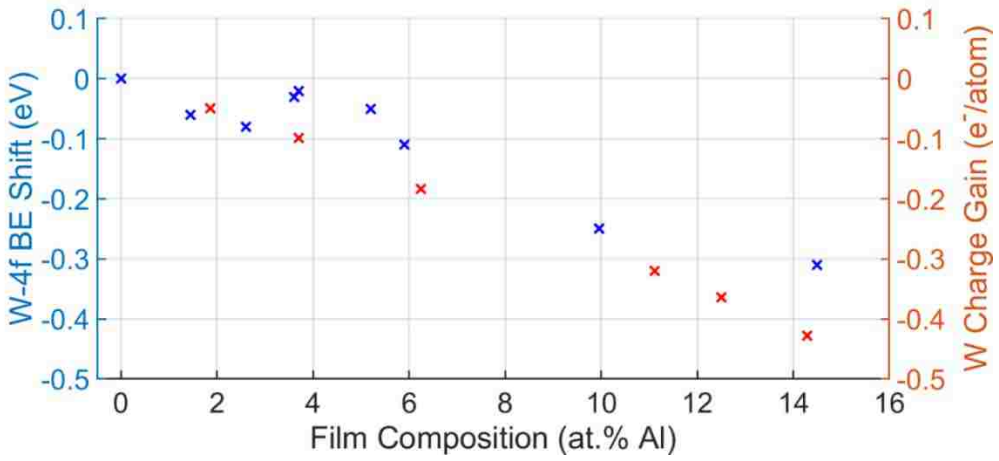

Figure 6.7 Results from Bader analysis are compared to XPS measurements for W atoms. The Bader analysis indicates a transfer of charge from the Al to the W atoms that results in charge accumulation on the W atoms. XPS scans revealed a shift in the BE of the W-4f peak (each spectrum has been charge-corrected to match 285 eV for adventitious carbon). The magnitude and direction of each shift observed in XPS, as a function of Al concentration, are in good agreement with those given by the Bader analysis. This supports the interpretation that charge is transferred from the Al-3p to the W-5d orbitals.

These results still do not directly explain why the W-Al solid solution alloys exhibit a smaller lattice parameter as the Al solute concentration is increased Figure 6.5. A possible explanation is that the difference between an un-ionized Al atom and the oxidized Al atom, both of coordination number 8, is larger than the difference between an un-ionized W atom and the reduced W atom. Of course, these are competing effects, where the reduced atom will become larger and the oxidized atom smaller, but the net effect would be a decrease in lattice parameter.

6.3.4 Variation in Work Function

The EWF is a fundamental electronic property that is largely considered to reflect the surface state of the material [192]. The EWF is defined as the minimum energy that is required to transport an electron from the Fermi level to a field-free region outside the solid when at 0 K and there is no electric field present [193, 194]. The EWF of the gradient films manufactured for this study are plotted in Figure 6.8 a) as a function of aluminum concentration and show that the EWF decreases gradually with increasing aluminum solute. The EWF of the pure W film differs significantly from the measured EWF of the gradient film with 14.5 at.% Al, exhibiting a difference of 0.36 eV. This decrease in EWF can be explained by considering the density of free electrons, as discussed below.

There are several methods that have been used in the past to calculate the EWF of a given material that have resulted in various states of agreement depending on the material being studied and its surface condition [194-197]. The prevailing model for calculating the EWF of a metal – Developed by Brodie in 1995 [195] and later modified by Halas and Durakiewicz in 1998 [197] (BHD model) - has shown excellent agreement with experimental results and is much simpler than its predecessors. The BHD approach has been shown to agree well with experimental EWF values for binary alloys that form solid solutions [194]. In the BHD model, the EWF of a material is expressed in terms of the Fermi energy and the electron density parameter, as shown below [196]:

$$\Phi = \frac{43.46\alpha}{r_s^{3/2} E_F^{1/2}} = \frac{e^3\sqrt{m}}{16\sqrt[3]{3}\pi^{\frac{5}{3}}\hbar\varepsilon_0^{\frac{3}{2}}} * \frac{z^{\frac{1}{6}}}{\sqrt{a}}$$

Equation 6.1 The Brodie-Halas-Durakiewicz (BDH) model for calculating work function based on the method of image forces.

where r_s is the electron density parameter, E_F is the Fermi energy, and α is a constant for the left-hand side of Equation 6.1. On the right-hand side of Equation 6.1, e is the charge of an electron, m is the mass of an electron, ε_0 is the vacuum permittivity, z is the number of valence electrons, and a is the lattice constant. It is noted that according to the right-hand side of Equation 6.1, the EWF is proportional to the valence state, $z^{1/6}$ and it has been shown that the free electron density is nominally equal to the valence state [197, 198]. Interpreting the results shown in Figure 6.8 b) in the context of Equation 6.1 explains why the EWF decreases with increasing Al content.

The spectra in Figure 6.8 b) were obtained in the low energy regime and represent the free electron density at the surface of the pure tungsten film and the aluminum rich film. The area under the respective curves in Figure 6.8 b) represent the total number of electron states at the surface of each material [198]. This area, multiplied by the Fermi-Dirac distribution can be used to show the total number of electron states at temperatures greater than 0 K. Importantly, however, the area under the curve is proportional to the valence state in Equation 6.1 [198]. As a result, when the valence decreases, a decrease in EWF should also be observed. When comparing the results in Figure 6.8 b) with the EWF results in Figure 6.8 a), it is observed that the EWF does indeed decrease as the area under the curve diminishes.

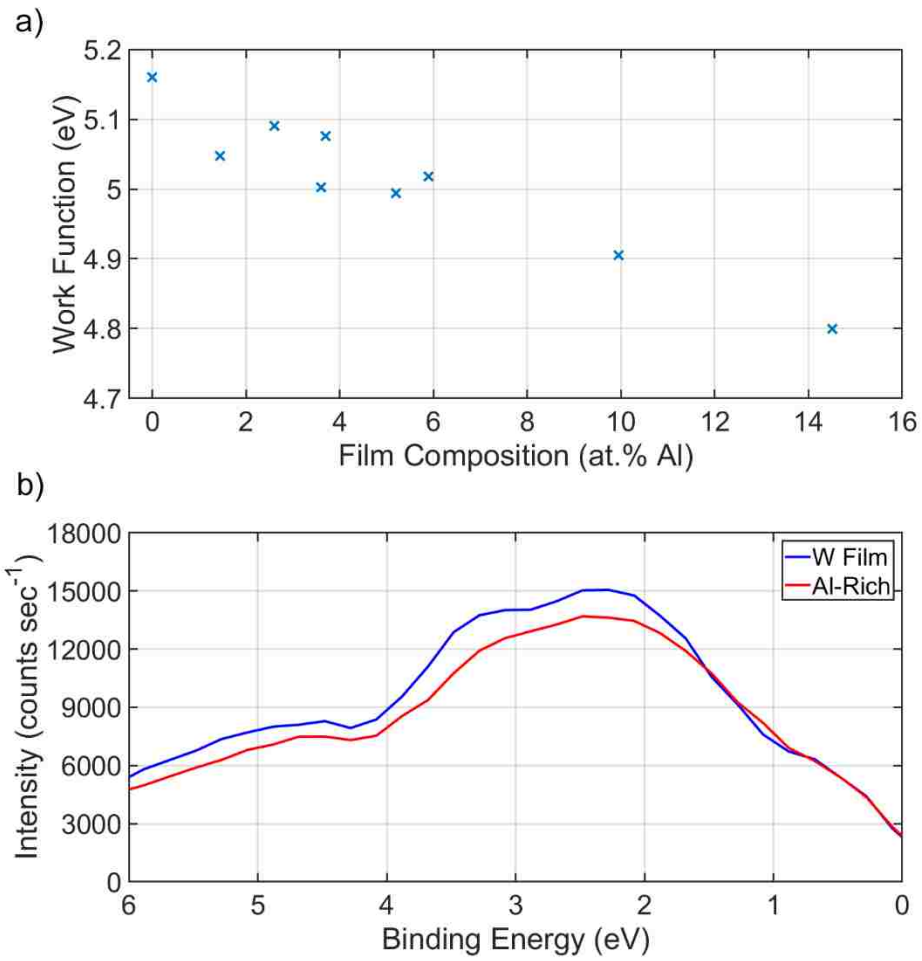

Figure 6.8 a) Contact potential difference was measured in vacuum to obtain the EWF values plotted for films with different Al content. Low energy XPS scans are shown in b) for the pure W film and the Al-rich film. These scans can be interpreted to indicate the valence band structure of each film, as the area under the curve is proportional to the number of free electrons in the sample.

The reason the BDH approach has been shown to perform so well in the prediction of the work function of metals and metallic binary solid solutions is largely due to the nature of the bonding between adjacent atoms and the effect this has on predicting the work done against the image forces [196]. Halas and Durakiewicz showed that the BHD model did not work well in predicting the EWF values for semiconductors [197]. This was primarily attributed to the localization of valence electrons resulting from the covalent

bonding between adjacent atoms. This affects the screening efficiency and results in an overestimated work function. The bonding between adjacent atoms in metals is predominantly metallic and therefore affects the screening efficiency to a much lesser extent. The W-Al system is no different. We have shown that the reason the W-4f BE shifts to lower values is because of screening effects when charge is transferred from the Al-3p to the W-5d orbitals. This screening effect also has an effect on the work function of the material because the distance at which the image force begins to act upon an ejected electron is larger; thereby lowering the EWF as more aluminum solute is added to the tungsten matrix.

The authors are of the impression that the decrease in EWF is primarily the result of a change in bonding character as aluminum is alloyed into the tungsten matrix and is not the result of changes in phases present or changes in texturing. The XRD results in Figure 6.3 a) show that all the sputtered films are single phase and highly (011) textured. It has been established that the different crystal faces of tungsten can lead to variations in EWF [199]. The XRD results in Figure 6.3 a) show that there are (011) and (112) diffraction, meaning that those planes are parallel to the surface of the film, with the (011) planes dominating; the (022) diffraction is just a higher order reflection of the (011) planes. This also makes sense when analyzing the EWF because the EWF associated with the (011) and (112) planes has been reported to be between $5.2 \leq \Phi_{011} \leq 5.4$ eV and $4.7 \leq \Phi_{112} \leq 4.9$ eV [199]. The EWF value for the (011) planes measured for the pure tungsten film is in good agreement with the literature value due to the high (011) texturing of the tungsten film. As aluminum is alloyed into the tungsten lattice, the texturing of the film is still dominated by the (011) texture and therefore cannot be the result of (112) texturing.

Table 6.2 A list of experimental values obtained for the lattice constant and the electron work function for the various W-Al alloyed films.

Film Composition (at %)	Lattice Constant (Å)	Electron Work Function (eV)
100	3.186	5.07
98.6	3.179	5.05
97.4	3.177	5.09
96.4	3.177	5.00
96.3	3.174	5.08
94.8	3.169	4.99
94.1	3.167	5.02
90.1	3.160	4.91
85.5	3.155	4.80

6.3.5 Mechanical Behavior

It is well known that obtaining accurate values of elastic modulus using the traditional Oliver-Pharr method for indentation is subject to significant substrate influence when the indentation depth is beyond 10% of the film thickness for the Berkovich geometry [36, 39, 49, 200]. However, when the mechanical behavior is sought for samples that have a thickness on the order of 100 nm, the small contact area associated with an indentation depth of 10 nm makes the elastic modulus and hardness prone to significant errors. By using the Hay-Crawford substrate deconvolution method to differentiate the elastic modulus of the film (E_f) from the elastic modulus of the substrate (E_s), these concerns can be alleviated for films that fall within the method limitations [36].

The Hay-Crawford method does have its limitations. The method has been shown to accurately predict the composite response for systems over the domain $0.1 < E_f/E_s < 10$, and is not able to deconvolute the substrate response for hardness. The literature value for the elastic modulus of (001) oriented silicon is approximately 170 GPa, and this value was verified by the authors of this study via nanoindentation [201]. The corollary to this argument is the testable range for the film modulus (17 GPa < Ef < 1700 GPa). This was deemed a satisfactory range for performing indentation on the films in this study based on literature values for elastic moduli of other similar sputter-deposited W and W-Al alloy films [162, 202]. The indentation results obtained on the W and W-Al alloy films in this study are shown in Figure 6.9. In the work of Hay-Crawford, they suggested that for a stiff film on a compliant substrate, the film modulus values were accurate up to an indentation depth to thickness ratio (δ/h) of 0.2 [36]. As a result, all the film modulus values in Figure 6.9 a) were taken at a δ/h value of 0.2. The film hardness values were taken at a δ/h value of approximately 0.35.

The elastic modulus of the pure tungsten film in Figure 6.9 a) does not agree well with the literature values. The elastic modulus of the pure tungsten film when analyzed using the Hay-Crawford method gave a value of 206 ± 40 GPa when measured at the appropriate δ/h ratio of 0.2. The literature value of pure tungsten has been reported to be 410 GPa and is in egregious disagreement with the value measured when using the Hay-Crawford method [39]. While the Hay-Crawford method was stated to give accurate values for both thin compliant films on stiff substrates, and for thin hard films on compliant substrates, the results for the pure tungsten film (218 nm in thickness) on the silicon substrate do not support that conclusion. Since the tungsten film is estimated to have a

modulus about 2.5 times greater than the silicon substrate, the authors are of the impression that this leads to deflated values of elastic film modulus because the contact area is over-estimated. The Hay-Crawford method was actually only shown to yield deconvoluted results with small associated error for the stiff films on the compliant substrates when the mismatch in modulus between the substrate and the film was rather mild ($E_f/E_s < 2$). The pure tungsten film on the silicon substrate is beyond that threshold, which may be why there is such a discrepancy.

With this in mind, it is dubious to try to extract meaningful information from the modulus values that are outside of this proven mismatch threshold, which would equate to be $E_f < 240$ GPa. There are two points in Figure 6.9 a) that are below that threshold and those are the films with the most aluminum content. Those films with approximately 10 and 14.5 at.% Al have elastic modulus values of 212 ± 23 GPa and 185 ± 13 GPa, respectively. It makes sense that the elastic modulus values would tend to decrease as aluminum is alloyed into the tungsten matrix because the work function of the material decreases with increasing aluminum content. This has recently been shown to be a good indicator of the strength of the atomic bonds between adjacent atoms in a crystalline lattice and a screening parameter for mechanical properties [198, 203-205].

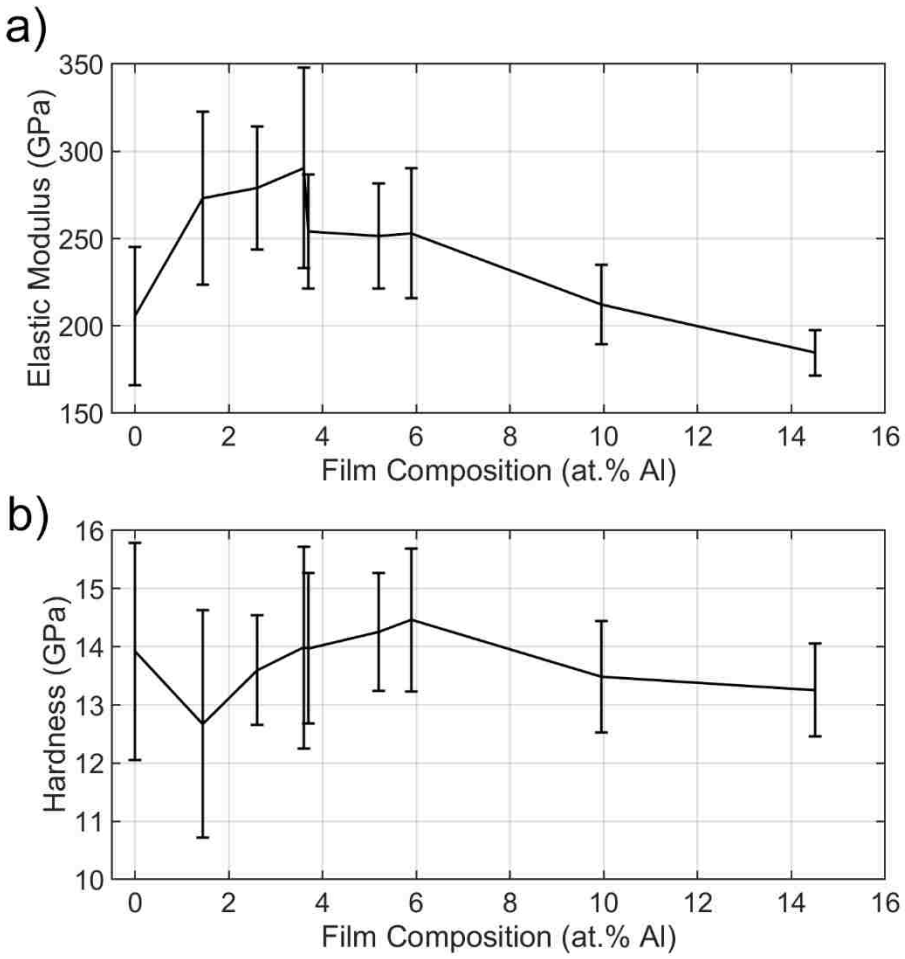

Figure 6.9 The Hay-Crawford substrate deconvolution method for thin films was used to obtain the values for elastic modulus shown in a) and the Oliver-Pharr technique was used to obtain the hardness values shown in b).

6.3.6 Conclusions

W-Al alloy films were deposited via magnetron sputtering to study how small changes in aluminum content affects the physical and electronic properties of the resulting films. XRD showed that the films were single phase BCC across the entire range investigated in this study. Furthermore, the lattice parameter was observed to decrease with increasing aluminum solute, which is opposite to predictions based on Vegard's law. Vegard's law was founded on models of continuum elasticity and does not consider

changes in the atom size when there is charge transfer/orbital hybridization. Shifts in XPS binding energy of tungsten core-electrons can be used to estimate the amount of charge being transferred between atoms due to screening effects. These shifts were corroborated by theoretical calculations based on Bader analysis to show that charge was being transferred and pDOS calculations imply that this occurred from the Al-3p to the W-5d orbitals. The decrease in lattice parameter with increasing aluminum solute, along with the charge transfer/orbital hybridization arguments, were used as evidence to support the idea that the rate at which the aluminum atoms get smaller upon transferring an electron is greater than the rate at which tungsten gets larger upon gaining an electron over the composition range studied. The screening effects that occur upon aluminum alloying also influences the EWF. As more charge is transferred to the tungsten atoms, the screening increases that results in a decrease in EWF.

7 Concluding Remarks and Future Work

The goal of the work related to the Si-Mg system was to increase the thickness of the resulting nanoporous silicon films such that the mechanical behavior could be studied. A previous student was able to show preliminary results where she was able to create nanoporous silicon by using distilled water at 50°C. The nanoporous silicon films had a thickness on the order of 200 nm and her attempts to increase the film thickness further resulted in film delamination. I extended this method of dealloying using distilled water to thicker films that resulted in nanoporous Si-Mg films on the order of 1 μm in thickness. This was achieved by reducing the temperature of the dealloying to just above freezing at 0.5°C and the entire dealloying procedure required between 48-72 hours to completely dealloy. The procedure was further optimized by utilizing a two-step procedure where I first would dealloy the films in 50°C distilled water for 30 minutes and then transfer the vials to the 0.5°C chiller for the remainder of the dealloying time. Gradient films of silicon and magnesium were sputtered to determine the parting limit range, and appeared to be between 51 and 54 at.% Si, with the best bicontinuous structure resulting from precursor films having a composition of 51 at.% Si. Also, several dealloying solutions were attempted, many of which used distilled water dissolved in various alcohol solutions. These results produced interesting microstructures in their own right, the most notable of which was completely black when viewed with the naked eye. The optimal dealloying solution, however, to create a bicontinuous structure was simply distilled water.

The structure of the nanoporous Si-Mg was thoroughly characterized with electron microscopy throughout the film thickness. The as-dealloyed films exhibited a bimodal distribution of ligaments, where the larger ligaments had an average width of 83 nm and

the smaller ligaments an average width of 19 nm. Additionally, there was a porous surface layer on the order of 100 nm thick that was present on most as-dealloyed films. XPS showed this layer to be largely composed of silicon and magnesium oxides. TEM of the as-dealloyed film showed that the structure was amorphous, but nanocrystalline grains formed after vacuum annealing at 500°C. XRD showed that the precursor films were also amorphous before dealloying. This implies that the as-dealloyed material retains the crystal structure of the precursor film. EDS mapping combined with XPS revealed three distinct chemical composition regions throughout the film thickness, where the residual magnesium increases as a function of film thickness, with the highest amount of retained magnesium at the surface. Since the technique does retain some magnesium within the structure, we have chosen to refer to the resulting structure as nanoporous Si-Mg. The ligament size, composition, and structure, combined with the simple, non-hazardous nature of the dealloying technique for efficient and scalable production of lithium-ion battery anode material. In the future, the procedure to create nanoporous silicon could be further optimized. For example, there may be instances where it would be desirable to create nanoporous silicon that is more homogeneous in terms of structure and composition.

Preliminary attempts to create micro-pillars of nanoporous silicon for the purpose of micro-pillar compression were unsuccessful. Consequently, nanoindentation was used to investigate the mechanical behavior of the nanoporous Si-Mg thin films. The as-dealloyed and annealed films of nanoporous Si-Mg were fabricated with a final thickness on the order of 1 μm such that the mechanical behavior could be studied with nanoindentation without muddling the film behavior with that of the substrate. A Berkovich tipped nanoindenter was used to probe the material behavior because it’s self-similarity

allows the most accurate probing of thin films. Preliminary attempts to study the mechanical response of the nanoporous silicon revealed slight time-dependence. As a result, the nanoporous silicon thin films were characterized in both the time and frequency domains. The as-dealloyed and annealed samples were investigated using a modified continuous stiffness measurement technique that optimizes the ability to achieve steady-state harmonic motion, such that accurate phase angle measurements could be obtained; the as-dealloyed and annealed samples exhibit distinct phase angles of 1.9° and 2.6°, respectively. Observations made in the time domain suggest that the time-dependence of nanoporous Si-Mg stems largely from plasticity. The reduced modulus values of as-dealloyed and annealed samples were investigated using the continuous stiffness measurement technique and have corresponding values of 5.78 GPa and 11.9 GPa, respectively. Similarly, the hardness of as-dealloyed and annealed samples are 167 MPa and 250 MPa, respectively. The point of investigating the mechanical behavior is to help inform how this material may behave in a lithium-ion battery during cycling. The true test of the cycling behavior will be when it has undergone rigorous testing in a model lithium-ion battery.

Preliminary XPS scans of a representative scandate cathode of excellent emission behavior showed that the binding energy for the W 4f peaks had shifted to lower values than expected. After interpreting the XPS work alongside EDS work that had been performed on a cross-section of a representative tungsten grain in the scandate cathode, it was thought that aluminum may diffuse into the matrix of tungsten grains near the surface and play a role in the excellent emission behavior of the scandate cathode. To further study this system, model films of W-Al were created in compositions that were similar to the

EDS results. Specifically, $W_{1-x}Al_x$ (x = 0-0.15) thin film alloys on the order of 150 nm in thickness were produced via magnetron sputtering to study how small changes in film composition affected the physical and electronic properties of the alloy films. XRD showed that all the films produced were single phase BCC where the lattice parameter of the W-Al alloy films decreased with increasing aluminum solute. The change in lattice parameter can not be explained using models of continuum elasticity, but rather with charge transfer resulting from orbital hybridization. DFT calculations along with Bader analysis were used to interpret core-level binding energy shifts observed with XPS to show that charge had been transferred from the Al-3p to the W-5d valence orbitals. The electron work function of the various films was measured with a Kelvin probe operating in CPD mode and showed that the electron work function decreased with alloying additions of aluminum. In the future, these thin films of W-Al could have other elements (Ba, Sc, Ca) sputtered on them and heated up to observe how the work function changes before, during and after heating.

Appendix A

```
%This gives the average and standard deviation for roughly the last 5
%seconds of the 60s hold period. Of course, I had to rename each file
%individually according to the convention: testn.dat, where n = 1-14.
%It then outputs the mean and stdev into .txt files in the same folder
%where this is run.

%Some initializations
nfiles = 14; %this is the number of separate files
filenameprefix = 'test'; %this is the filename prefix
filenameextension = '.dat'; %this is the filename extension
timecolumnstart = 5400;
timecolumnincrement = 1;
timecolumnend = 5900;
counter_stop = 500; %this represents 5 seconds
phase_angle_column = 2; %this is the phase angle column
DLDD_column = 8; %DLDD = dynamic load/dynamic displacement
E_r_column = 9; %reduced modulus column

for i = 1:nfiles
    counter = 0;
    for j = timecolumnstart:timecolumnincrement:timecolumnend
        filename = [filenameprefix, int2str(i),filenameextension];
        tmpdata = load(filename,'-ascii');
        counter = counter +1;
        phase(i,counter) = tmpdata(j,phase_angle_column);
        DLDD(i,counter) = tmpdata(j,DLDD_column);
        E_r(i,counter) = tmpdata(j,E_r_column);
    end
end

    mean_values_phase = mean2(phase);
    stdev_values_phase = std2(phase);
    mean_values_DLDD = mean2(DLDD);
    stdev_values_DLDD = std2(DLDD);
    mean_values_E_r = mean2(E_r);
    stdev_values_E_r = std2(E_r);
    save('mean_valu_phase.txt','mean_values_phase','-ASCII');
    save('stdev_valu_phase.txt','stdev_values_phase','-ASCII');
    save('mean_valu_DLDD.txt','mean_values_DLDD','-ASCII');
    save('stdev_valu_DLDD.txt','stdev_values_DLDD','-ASCII');
    save('mean_valu_E_r.txt','mean_values_E_r','-ASCII');
    save('stdev_valu_E_r.txt','stdev_values_E_r','-ASCII');
```

```
%calculate corrected phase angle and error propagation. This must be
%done for each frequency where the phase angle is experimentally
%determined. The equations used to correct the phase angle were
%published by Herbert et al. in 2008.

DLDD = (3.8222303e+03); %Dyn. Load/Dyn. Disp of sample (N/m)
DLDD_err = (8.8365989e+02); %Dyn. Load/Dyn. Disp of sample error (N/m)
DLDD_fs = 171.8897103; %Dyn. Load/Dyn. Disp in free space (N/m)
DLDD_fs_err = (2.84217E-14) ; %Dyn. Load/Dyn. Disp in free space error
(N/m)
delta_coupled = 2.1968703e+00; %measured phase angle of sample
(degrees)
delta_coupled_err = (8.0839197e-01) ; %Error in measured phase angle
(degrees)
delta_fs = 2.767311612; %measured phase angle in free space (degrees)
delta_fs_err = 0.001662726; %Error in measured phase angle in free
space (degrees)
K_lf = (19.35e+6); %Stiffness of load frame (N/m)
K_lf_err = 0; %Error in the load frame stiffness (N/m)

out_phase = DLDD*sin(delta_coupled*(3.14159/180))-
DLDD_fs*sin(delta_fs*(3.14159/180));
in_phase = (((1/(DLDD*cos(delta_coupled*(3.14159/180))-
DLDD_fs*cos(delta_fs*(3.14159/180)))-(1/K_lf))))^(-1);

partial_DLDD =
(sin(delta_coupled*(3.14159/180))*(1/(DLDD*cos(delta_coupled*(3.14159/1
80))-DLDD_fs*cos(delta_fs*(3.14159/180)))-1/K_lf)-
((cos(delta_coupled*(3.14159/180))*(DLDD*sin(delta_coupled*(3.14159/180
))-
DLDD_fs*sin(delta_fs*(3.14159/180))))/(DLDD*cos(delta_coupled*(3.14159/
180))-
DLDD_fs*cos(delta_fs*(3.14159/180)))^2))/((DLDD*sin(delta_coupled*(3.14
159/180))-
DLDD_fs*sin(delta_fs*(3.14159/180)))^2*(1/(DLDD*cos(delta_coupled*(3.14
159/180))-DLDD_fs*cos(delta_fs*(3.14159/180)))-1/K_lf)^2+1);
partial_DLDD_fs =
(((cos(delta_fs*(3.14159/180))*(DLDD*sin(delta_coupled*(3.14159/180))-
DLDD_fs*sin(delta_fs*(3.14159/180))))/(DLDD*cos(delta_coupled*(3.14159/
180))-DLDD_fs*cos(delta_fs*(3.14159/180)))^2)-
sin(delta_fs*(3.14159/180))*(1/(DLDD*cos(delta_coupled*(3.14159/180))-
DLDD_fs*cos(delta_fs*(3.14159/180)))-
1/K_lf))/((DLDD*sin(delta_coupled*(3.14159/180))-
DLDD_fs*sin(delta_fs*(3.14159/180)))^2*((1/(DLDD*cos(delta_coupled*(3.1
4159/180))-DLDD_fs*cos(delta_fs*(3.14159/180)))-1/K_lf))^2+1);
partial_delta_coupled =
(DLDD*cos(delta_coupled*(3.14159/180))*((1/(DLDD*cos(delta_coupled*(3.1
4159/180))-DLDD_fs*cos(delta_fs*(3.14159/180)))-
1/K_lf))+((DLDD*sin(delta_coupled*(3.14159/180))*(DLDD*sin(delta_couple
d*(3.14159/180))-
DLDD_fs*sin(delta_fs*(3.14159/180))))/(DLDD*cos(delta_coupled*(3.14159/
180))-
DLDD_fs*cos(delta_fs*(3.14159/180)))^2))/((DLDD*sin(delta_coupled*(3.14
```

```
159/180))-
DLDD_fs*sin(delta_fs*(3.14159/180)))^2*((1/(DLDD*cos(delta_coupled*(3.1
4159/180))-DLDD_fs*cos(delta_fs*(3.14159/180)))-1/K_lf)^2)+1);
partial_delta_fs = (-
DLDD_fs*sin(delta_fs*(3.14159/180))*((1/(DLDD*cos(delta_coupled*(3.1415
9/180))-DLDD_fs*cos(delta_fs*(3.14159/180)))-1/K_lf))-
((DLDD_fs*sin(delta_fs*(3.14159/180))*(DLDD*sin(delta_coupled*(3.14159/
180))-
DLDD_fs*sin(delta_fs*(3.14159/180))))/(DLDD*cos(delta_coupled*(3.14159/
180))-
DLDD_fs*cos(delta_fs*(3.14159/180)))^2))/((DLDD*sin(delta_coupled*(3.14
159/180))-
DLDD_fs*sin(delta_fs*(3.14159/180)))^2*((1/(DLDD*cos(delta_coupled*(3.1
4159/180))-DLDD_fs*cos(delta_fs*(3.14159/180))))-1/K_lf)^2+1);
error_prop_delta =
(partial_DLDD^2*DLDD_err^2+partial_DLDD_fs^2*DLDD_fs_err^2+partial_delt
a_coupled^2*(delta_coupled_err)^2+partial_delta_fs^2*delta_fs_err^2)^0.
5;

delta_corr = atan(out_phase/in_phase);
delta_corr = delta_corr*(180/3.14159);

save('corrected_phase.txt','delta_corr','-ascii')
save('corrected_phase_err.txt','error_prop_delta','-ascii')
```

Appendix B

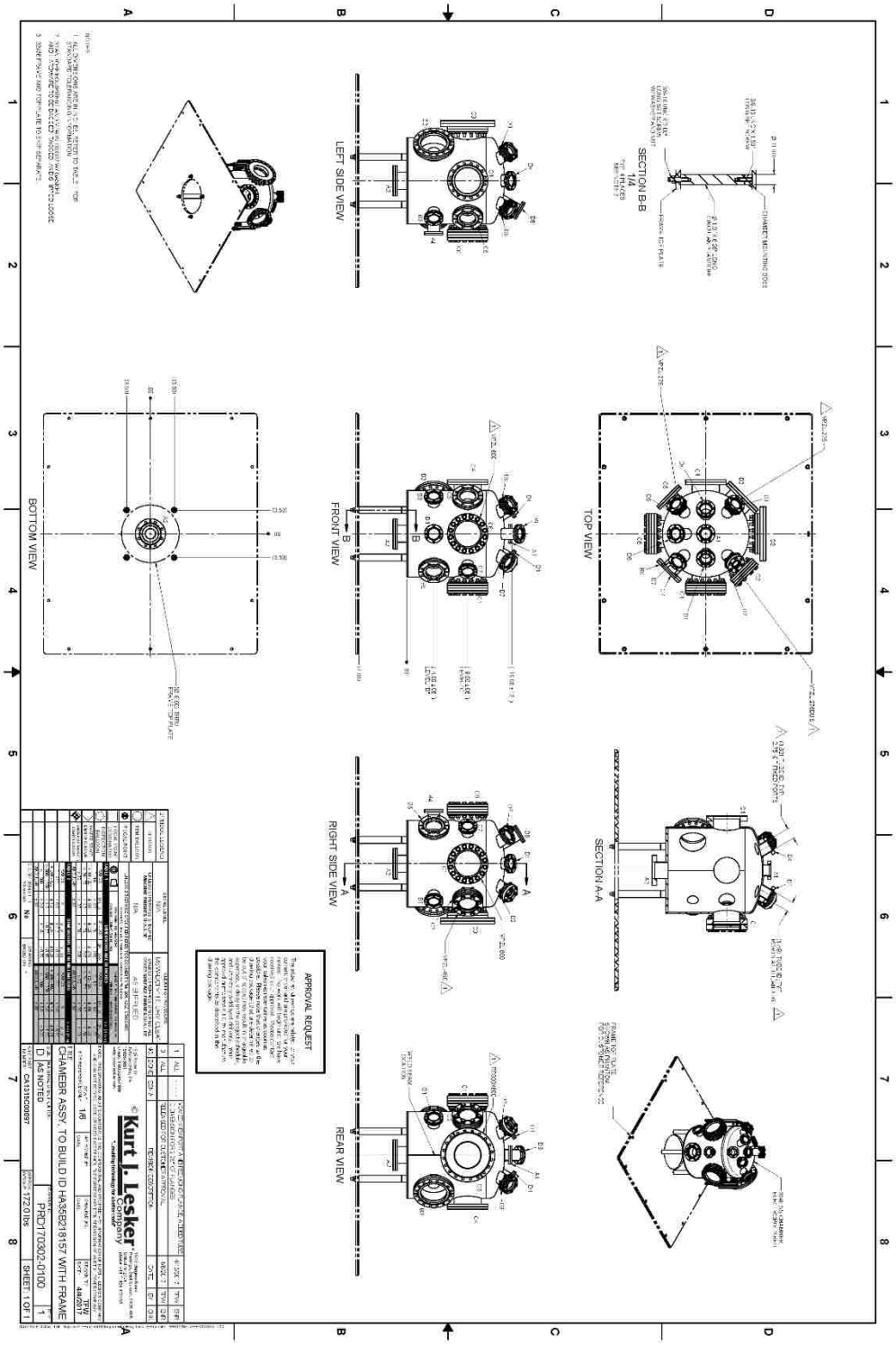
TOP VIEW
FRONT VIEW
RIGHT SIDE VIEW
LEFT SIDE VIEW
REAR VIEW
BOTTOM VIEW
SECTION A-A
SECTION B-B
APPROVAL REQUEST
Kurt J. Lesker
CHAMBER ASSY, TO BUILD ID H435E218157 WITH FRAME
PRD170302-0100
SHEET 1 OF 1

PORT IDENTIFICATION TABLE

PORT	FLANGE/BOSS	TUBE	TUBE OUT LENGTH	PORT LENGTH	PORT ID	FOCAL LENGTH	FOCAL LENGTH TOL +/-	FOCAL PT DIA	FOCAL PT TOL DIA	ALPHA °	BETA °	CUSTOMER REF	FUNCTION
A	FC275/1625T	SST-E 321	-	-	-	-	-	-	-	-	0	A	BP
AL	1340JC20R	SST-E350	-	2.00	3.06	-	-	-	-	-	180	A-BOTTOM	-
B	1320S1175R	SST-E 750	-	1.63	3.13	-	-	-	-	45	90	B	-
BD	1320S1175R	SST-E 750	-	1.63	3.13	-	-	-	-	135	90	D	-
BF	1320S1175R	SST-E 750	-	1.63	3.13	-	-	-	-	225	90	F	-
BL	1320S1175R	SST-E 750	-	1.63	3.13	-	-	-	-	270	90	L	-
BN	1340JC20R	SST-E350	-	1.69	3.19	-	-	-	-	315	90	N	-
C	1320S1175R	SST-E 750	-	1.63	3.13	-	-	-	-	0	90	J	-
C2	1340JC20R	SST-E350	-	1.69	3.19	-	-	-	-	45	90	M	-
C3	1320S1175R	SST-E 750	-	1.63	3.13	-	-	-	-	90	90	K	-
C4	1320S1175R	SST-E 750	-	1.63	3.13	-	-	-	-	135	90	E	-
C5	1340JC20R	SST-E350	-	1.69	3.19	-	-	-	-	225	90	I	-
C6	1320S1175R	SST-E 750	-	1.63	3.13	-	-	-	-	270	90	H	-
C7	1320S1175R	SST-E 750	-	1.63	3.13	-	-	-	-	315	90	G	-
D	FC275/1625T	SST-E 321	-	-	-	7.50	0.13	6	14	0	90	B	BSA
D2	FC275/1750	SST-E 750	-	-	-	8.50	0.13	8	18	45	45	F	L1
D3	FC275/1750	SST-E 750	-	-	-	8.50	0.13	8	18	90	45	D	L1
D4	FC275/1750	SST-E 750	-	-	-	7.50	0.13	6	14	180	90	C	RS
D5	1320S1175R	SST-E 750				8.50	0.13	8	18	225	45	I	L1
D6	FC275/1625	SST-E 321	-	-	-	5.50	0.13	6	14	135	90	P	BP
D7	FC275/1750	SST-E 750	-	-	-	8.50	0.13	8	18	315	45	I	PWD

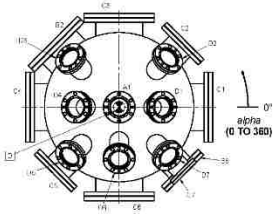

TOP VIEW

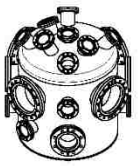

APPROVAL REQUEST

The above-listed drawings are ready to your comments and are provided for your review. Upon review, if no changes are required, please note your approval. Please contact your sales representative as soon as possible. Please note that changes to the drawing/package that are determined to be major scope may result in changes to the price, delivery, and ultimately delay/cancel delivery. Your approval authorizes LKL to manufacture the components as described in the drawing/package.

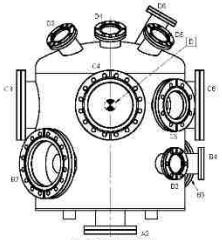
LEFT SIDE VIEW

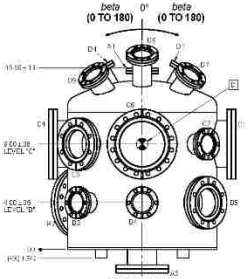

FRONT VIEW

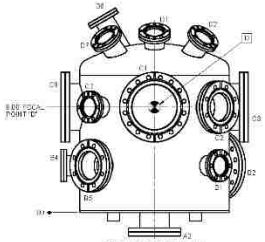
RIGHT SIDE VIEW

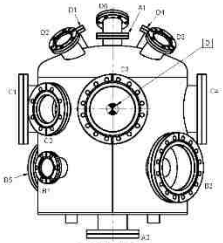
REAR VIEW

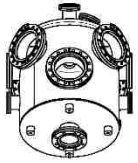

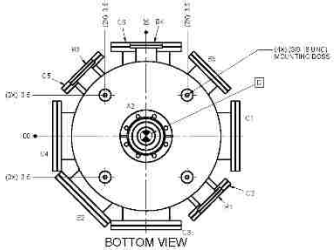
BOTTOM VIEW

NOTES:
1. ALL DIMENSIONS ARE IN INCHES. REFER TO TABLE 1 FOR STANDARD TOLERANCING INFORMATION.
2. ALL WELDS TO BE INTERNAL FULL PEN OR ONE DIAMETER UNLESS OTHERWISE NOTED.
3. VACUUM WELDED TO 4E-9 LEAK CHECKED WITH A HELIUM MASS SPECTROMETER WITH A SENSITIVITY TO 2 X 10 $^{-10}$ STD CC/SEC FOR HELIUM.
4. DIMENSIONS FOR ALL PARTS LISTED IN THE B.O.M. OF MATERIALS ARE NOMINAL.

SYMBOL LEGEND	INITIAL LEVEL: WOW PCP 11R, LEVEL 1	AS MODIFIED BY: WS/WELD 101, LEVEL 1
REVISION	UNLESS OTHERWISE SPECIFIED MACHINE FINISHES SHALL BE:	UNLESS OTHERWISE SPECIFIED ALL MACHINED SURFACES FINISHES SHALL BE:
ITEM BALLOON	N/A	ELECTROPOLISH
TOLERANCES	ALL DIMENSIONS ARE IN INCHES. TOLERANCES ARE +/- UNLESS OTHERWISE SPECIFIED. DIMENSIONS APPLY BEFORE PLATING.	

NO.	ZONE	BY	REVISION DESCRIPTION	DATE	BY	CHK
1	ALL		PORT 24 WAS FOR WELDS_28 WAS "+DD	1/12/2017	TFW	DHT
0	ALL	- - -	RELEASE FOR CUSTOMER APPROVAL	4/6/2017	TFW	DHT

Kurt J. Lesker Company
"...enabling technology for a better world"

TITLE	CHAMBER WELDMENT FOR CA1315C00097
SIZE	D
REFERENCE DESIGNATOR	AS NOTED
SCALE	1/4
DRAWING NO.	PRD170302-0500
REV	1
WEIGHT	96.0 lbs
SHEET	1 OF 1

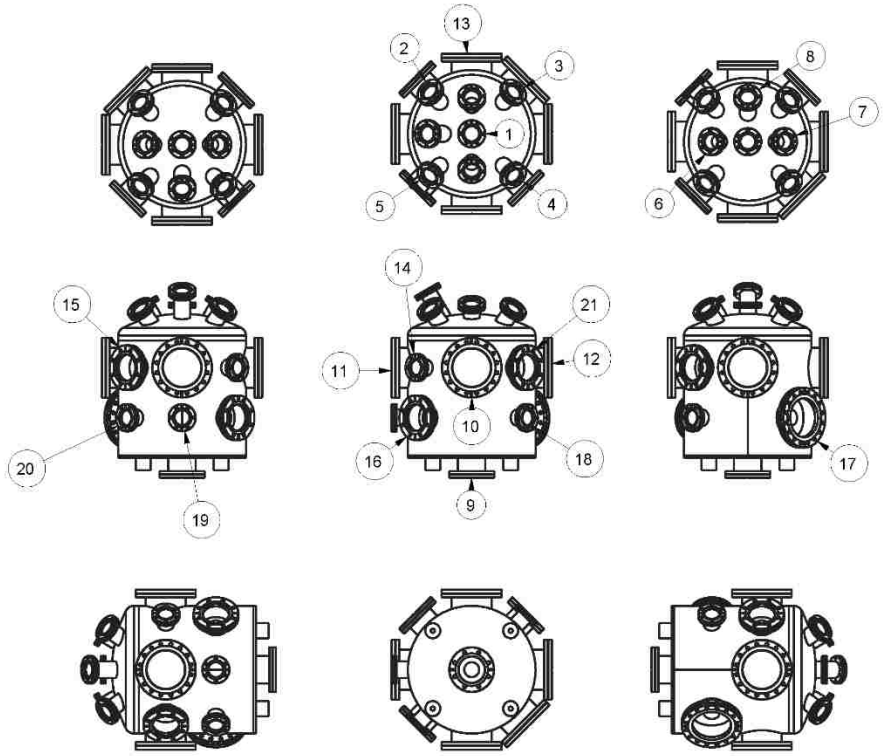

Port #	Port Size	Port Description
1	2.75"	Kelvin Probe
2	2.75"	SPS
3	2.75"	APS Camera
4	2.75"	UV LED
5	2.75"	APS
6	2.75"	RGA
7	2.75"	AES
8	2.75"	Ion Gun
9	4.5"	Heater
10	6"	View-port/Pyrometer
11	6"	View-port
12	6"	Transfer Arm
13	6"	Extra
14	2.75"	Rotary Shutter
15	4.5"	Extra
16	4.5"	Gas Inlet
17	6"	Ion Pump
18	2.75"	Extra
19	2.75"	Pressure gauge?
20	2.75"	Ti-sub Pump?
21	4.5"	View-port

References

[1] F. Östlund, K. Rzepiejewska-Malyska, K. Leifer, L.M. Hale, Y. Tang, R. Ballarini, W.W. Gerberich, J. Michler, Brittle-to-Ductile Transition in Uniaxial Compression of Silicon Pillars at Room Temperature, Adv. Funct. Mater. 19(15) (2009) 2439-2444.
[2] K. Feng, M. Li, W. Liu, A.G. Kashkooli, X. Xiao, M. Cai, Z. Chen, Silicon-Based Anodes for Lithium-Ion Batteries: From Fundamentals to Practical Applications, Small 14(8) (2018) 1702737.
[3] G. Gartner, P. Geittner, H. Lydtin, A. Ritz, Emission Properties of Top-Layer Scandate Cathodes Prepared by LAD, Applied Surface Science 111 (1997) 11-17.
[4] Clarification of the Mechanism of the De-Alloying Phenomena, Corrosion 25(12) (1969) 519-519.
[5] A. Wittstock, J. Biener, M. Baumer, Chapter 1 Introduction to Nanoporous Gold, Nanoporous Gold: From an Ancient Technology to a High-Tech Material, The Royal Society of Chemistry2012, pp. 1-10.
[6] A.J. Forty, Corrosion micromorphology of noble metal alloys and depletion gilding, Nature 282(5739) (1979) 597-598.
[7] J. Erlebacher, M.J. Aziz, A. Karma, N. Dimitrov, K. Sieradzki, Evolution of nanoporosity in dealloying, Nature 410(6827) (2001) 450-453.
[8] J. Erlebacher, An Atomistic Description of Dealloying, J. Electrochem. Soc. 151(10) (2004) C614.
[9] R.P. Elliott, F.A. Shunk, The Ag−Au (Silver-Gold) system, Bulletin of Alloy Phase Diagrams 1(2) 45-47.
[10] K. Sieradzki, N. Dimitrov, D. Movrin, C. McCall, N. Vasiljevic, J. Erlebacher, The Dealloying Critical Potential, J. Electrochem. Soc. 149(8) (2002) B370-B377.
[11] J.W. Cahn, J.E. Hilliard, Free Energy of a Nonuniform System. III. Nucleation in a Two-Component Incompressible Fluid, The Journal of Chemical Physics 31(3) (1959) 688-699.
[12] A. Uhlir, Electrolytic Shaping of Germanium and Silicon, Bell System Technical Journal 35(2) (1956) 333-347.
[13] D.R. Turner, Electropolishing Silicon in Hydrofluoric Acid Solutions, J. Electrochem. Soc. 105(7) (1958) 402-408.
[14] L.T. Canham, Silicon quantum wire array fabrication by electrochemical and chemical dissolution of wafers, Applied Physics Letters 57(10) (1990) 1046-1048.
[15] D. Dimova-Malinovska, M. Sendova-Vassileva, N. Tzenov, M. Kamenova, Preparation of thin porous silicon layers by stain etching, Thin Solid Films 297(1–2) (1997) 9-12.
[16] Z. Huang, N. Geyer, P. Werner, J. de Boor, U. Gösele, Metal-Assisted Chemical Etching of Silicon: A Review, Advanced Materials 23(2) (2011) 285-308.
[17] Y. Liu, Z.H. Xiong, Y. Liu, S.H. Xu, X.B. Liu, X.M. Ding, X.Y. Hou, A novel method of fabricating porous silicon material: ultrasonically enhanced anodic electrochemical etching, Solid State Communications 127(8) (2003) 583-588.
[18] A. Ulvestad, Porous Silicon as Anode Material for Li-ion Batteries, Materials Science and Engineering, Norwegian University of Science and Engineering, 2013, p. 140.
[19] S. Basu, J. Kanungo, Nanocrystalline Porous Silicon, in: S. Basu (Ed.), Crystalline Silicon- Properties and Uses, InTech, 2011, pp. 219-250.

[20] P. Granitzer, K. Rumpf, Porous Silicon—A Versatile Host Material, Materials 3(2) (2010) 943-998.
[21] O. Bisi, S. Ossicini, L. Pavesi, Porous silicon: a quantum sponge structure for silicon based optoelectronics, Surface Science Reports 38(1–3) (2000) 1-126.
[22] X.G. Zhang, Morphology and Formation Mechanisms of Porous Silicon, J. Electrochem. Soc. 151(1) (2004) C69-C80.
[23] E. Detsi, S. Punzhin, J. Rao, P.R. Onck, J.T.M. De Hosson, Enhanced Strain in Functional Nanoporous Gold with a Dual Microscopic Length Scale Structure, ACS Nano 6(5) (2012) 3734-3744.
[24] Y. Ding, J. Erlebacher, Nanoporous Metals with Controlled Multimodal Pore Size Distribution, Journal of the American Chemical Society 125(26) (2003) 7772-7773.
[25] N. Tsubaki, Y. Zhang, S. Sun, H. Mori, Y. Yoneyama, X. Li, K. Fujimoto, A new method of bimodal support preparation and its application in Fischer–Tropsch synthesis, Catalysis Communications 2(10) (2001) 311-315.
[26] Z. Qi, J. Weissmüller, Hierarchical Nested-Network Nanostructure by Dealloying, ACS Nano 7(7) (2013) 5948-5954.
[27] T. Song, M. Yan, Z. Shi, A. Atrens, M. Qian, Creation of bimodal porous copper materials by an annealing-electrochemical dealloying approach, Electrochim. Acta 164 (2015) 288-296.
[28] Q. Hao, D. Zhao, H. Duan, Q. Zhou, C. Xu, Si/Ag composite with bimodal micro-nano porous structure as a high-performance anode for Li-ion batteries, Nanoscale 7(12) (2015) 5320-5327.
[29] T. Wada, T. Ichitsubo, K. Yubuta, H. Segawa, H. Yoshida, H. Kato, Bulk-Nanoporous-Silicon Negative Electrode with Extremely High Cyclability for Lithium-Ion Batteries Prepared Using a Top-Down Process, Nano Lett. 14(8) (2014) 4505-4510.
[30] T. Wada, J. Yamada, H. Kato, Preparation of three-dimensional nanoporous Si using dealloying by metallic melt and application as a lithium-ion rechargeable battery negative electrode, Journal of Power Sources 306 (2016) 8-16.
[31] J.D. Harrison, C. Wagner, The attack of solid alloys by liquid metals and salt melts, Acta Metall. 7(11) (1959) 722-735.
[32] T. Wada, K. Yubuta, A. Inoue, H. Kato, Dealloying by metallic melt, Materials Letters 65(7) (2011) 1076-1078.
[33] L. Wang, N. Briot, P. Swartzentruber, T.J. Balk, Magnesium Alloy Precursor Thin Films for Efficient, Practical Fabrication of Nanoporous Metals, Metall and Mat Trans A 45(1) (2014) 1-5.
[34] X. Jiang, Synthesis, structure, properties and applications of nanoporous silicon and palladium, Chemical and Materials Engineering, University of Kentucky, UKnowledge, 2015.
[35] A. Gouldstone, N. Chollacoop, M. Dao, J. Li, A.M. Minor, Y.-L. Shen, Indentation across size scales and disciplines: Recent developments in experimentation and modeling, Acta Mater. 55(12) (2007) 4015-4039.
[36] J.L. Hay, B. Crawford, Measuring Substrate-Independent Modulus of Thin Films, J. Mater. Res. 26(6) (2011) 727-738.
[37] W.C. Oliver, G.M. Pharr, Measurement of hardness and elastic modulus by instrumented indentation: Advances in understanding and refinements to methodology, J. Mater. Res. 19(1) (2004) 3-20.

[38] A.C. Fischer-Cripps, Nanoindentation Testing, in: A.C. Fischer-Cripps (Ed.), Nanoindentation, Springer New York, New York, NY, 2002, pp. 20-35.
[39] W.C. Oliver, G.M. Pharr, AN IMPROVED TECHNIQUE FOR DETERMINING HARDNESS AND ELASTIC-MODULUS USING LOAD AND DISPLACEMENT SENSING INDENTATION EXPERIMENTS, J. Mater. Res. 7(6) (1992) 1564-1583.
[40] L.J. Gibson, M.F. Ashby, Cellular Solids: Structure and Properties, 2 ed., Cambridge University Press, Cambridge, 1997.
[41] D. Bellet, P. Lamagnère, A. Vincent, Y. Bréchet, Nanoindentation investigation of the Young's modulus of porous silicon, J. Appl. Phys. 80(7) (1996) 3772-3776.
[42] A.M. Hodge, J. Biener, J.R. Hayes, P.M. Bythrow, C.A. Volkert, A.V. Hamza, Scaling equation for yield strength of nanoporous open-cell foams, Acta Mater. 55(4) (2007) 1343-1349.
[43] N.J. Briot, T.J. Balk, Developing scaling relations for the yield strength of nanoporous gold, Philos. Mag. 95(27) (2015) 2955-2973.
[44] N.J. Briot, T. Kennerknecht, C. Eberl, T.J. Balk, Mechanical properties of bulk single crystalline nanoporous gold investigated by millimetre-scale tension and compression testing, Philos. Mag. 94(8) (2014) 847-866.
[45] M.F. Ashby, The properties of foams and lattices, Philos. Trans. R. Soc., A 364(1838) (2006) 15-30.
[46] X. Chen, Y. Xiang, J.J. Vlassak, Novel technique for measuring the mechanical properties of porous materials by nanoindentation, J. Mater. Res. 21(03) (2006) 715-724.
[47] E.W. Andrews, G. Gioux, P. Onck, L.J. Gibson, Size effects in ductile cellular solids. Part II: experimental results, International Journal of Mechanical Sciences 43(3) (2001) 701-713.
[48] N.J. Briot, T.J. Balk, Focused ion beam characterization of deformation resulting from nanoindentation of nanoporous gold, MRS Commun. 8(1) (2018) 132-136.
[49] J.L. Hay, M.E. O'Hern, W.C. Oliver, Tie Importance of Contact Radius for Substrate-Independent Property Measurement of Thin Films, MRS Proc. 522 (1998).
[50] X. Chen, J.J. Vlassak, Numerical study on the measurement of thin film mechanical properties by means of nanoindentation, J. Mater. Res. 16(10) (2001) 2974-2982.
[51] M. Herrmann, F. Richter, S.E. Schulz, Study of nano-mechanical properties for thin porous films through instrumented indentation: SiO2 low dielectric constant films as an example, Microelectronic Engineering 85(10) (2008) 2172-2174.
[52] K. Lionti, K. Virwani, W. Volksen, R. King, J. Frommer, G. Dubois, Accurate Measurement of Porous Low-k Thin-Films by Nanoindentation: Densification Scaling versus Substrate Effects, ECS Journal of Solid State Science and Technology 6(10) (2017) N209-N212.
[53] R.F. Cook, M.L. Oyen, Nanoindentation behavior and mechanical properties measurement of polymeric materials, International Journal of Materials Research 98(5) (2007) 370-378.
[54] E.G. Herbert, P. Sudharshan Phani, K.E. Johanns, Nanoindentation of viscoelastic solids: A critical assessment of experimental methods, Curr. Opin. Solid State Mater. Sci. 19(6) (2015) 334-339.
[55] E.G. Herbert, W.C. Oliver, A. Lumsdaine, G.M. Pharr, Measuring the constitutive behavior of viscoelastic solids in the time and frequency domain using flat punch nanoindentation, J. Mater. Res. 24(03) (2009) 626-637.

[56] M.L. Oyen, Analytical techniques for indentation of viscoelastic materials, Philos. Mag. 86(33-35) (2006) 5625-5641.
[57] E. Herbert, K. Johanns, R. Singleton, G.M. Pharr, On the Measurement of Energy Dissipation using Nanoindentation and the Continuous Stiffness Measurement Technique, J. Mater. Res. 28(21) (2013).
[58] E.G. Herbert, W.C. Oliver, G.M. Pharr, Nanoindentation and the dynamic characterization of viscoelastic solids, J. Phys. D: Appl. Phys. 41(7) (2008) 074021.
[59] A. Bolshakov, G.M. Pharr, Influences of pileup on the measurement of mechanical properties by load and depth sensing indentation techniques, J. Mater. Res. 13(4) (2011) 1049-1058.
[60] M. Hardiman, T.J. Vaughan, C.T. McCarthy, The effects of pile-up, viscoelasticity and hydrostatic stress on polymer matrix nanoindentation, Polym. Test. 52 (2016) 157-166.
[61] D. Tranchida, S. Piccarolo, J. Loos, A. Alexeev, Mechanical Characterization of Polymers on a Nanometer Scale through Nanoindentation. A Study on Pile-up and Viscoelasticity, Macromolecules 40(4) (2007) 1259-1267.
[62] J.L. Cronin, Modern dispenser cathodes, IEE Proceedings I - Solid-State and Electron Devices 128(1) (1981) 19-32.
[63] Engineered Surface Properties of Porous Tungsten from Cryogenic Machining, Chemical and Materials Engineering, University of Kentucky, UKnowledge, 2015.
[64] W. Liu, K. Zhang, Y. Wang, K. Pan, X. Gu, J. Wang, J. Li, M. Zhou, Operating model for scandia doped matrix scandate cathodes, Applied Surface Science 251(1) (2005) 80-88.
[65] P.M. Zagwijn, J.W.M. Frenken, U. van Slooten, P.A. Duine, A model system for scandate cathodes, Applied Surface Science 111 (1997) 35-41.
[66] R. Levi, Improved ``Impregnated Cathode'', J. Appl. Phys. 26(5) (1955) 639-639.
[67] G. Lesny, R. Forman, Surface studies on scandate cathodes and synthesized scandates, IEEE Transactions on Electron Devices 37(12) (1990) 2595-2604.
[68] R.S. Raju, C.E. Maloney, Characterization of an impregnated scandate cathode using a semiconductor model, IEEE Transactions on Electron Devices 41(12) (1994) 2460-2467.
[69] B. Vancil, I. Brodie, J. Lorr, V. Schmidt, Scandate Dispenser Cathodes With Sharp Transition and Their Application in Microwave Tubes, IEEE Transactions on Electron Devices 61(6) (2014) 1754-1759.
[70] Y. Wang, J. Wang, W. Liu, L. Li, Y. Wang, X. Zhang, Correlation Between Emission Behavior and Surface Features of Scandate Cathodes, IEEE Transactions on Electron Devices 56(5) (2009) 776-785.
[71] H. Yuan, X. Gu, K. Pan, Y. Wang, W. Liu, K. Zhang, J. Wang, M. Zhou, J. Li, Characteristics of scandate-impregnated cathodes with sub-micron scandia-doped matrices, Applied Surface Science 251(1) (2005) 106-113.
[72] J. Zhao, N. Li, J. Li, L.R. Barnett, M. Banducci, D. Gamzina, Z.A. Munir, N.C. Luhmann, High Current Density and Long-Life Nanocomposite Scandate Dispenser Cathode Fabrication, IEEE Transactions on Electron Devices 58(4) (2011) 1221-1228.
[73] E.L. Murphy, R.H. Good, Thermionic Emission, Field Emission, and the Transition Region, Physical Review 102(6) (1956) 1464-1473.
[74] O.W. Richardson, On the Positive Ionization produced by Hot Platinum in Air at Low Pressures, Proceedings of the Physical Society of London 18(1) (1903) 524.

[75] C.R. Crowell, The Richardson constant for thermionic emission in Schottky barrier diodes, Solid-State Electronics 8(4) (1965) 395-399.
[76] C. Wan, Study of Scandate Cathode Surface Materials, Department of Physics and Astronomy, Ohio University, 2015.
[77] M. Ohring, Chapter 4 - Discharges, Plasmas, and Ion–Surface Interactions, Materials Science of Thin Films (Second Edition), Academic Press, San Diego, 2002, pp. 145-202.
[78] M. Hughes, What is Sputtering? Magnetron Sputtering? <http://www.semicore.com/what-is-sputtering>, 2014).
[79] M. Ohring, Chapter 5 - Plasma and Ion Beam Processing of Thin Films, Materials Science of Thin Films (Second Edition), Academic Press, San Diego, 2002, pp. 203-275.
[80] M. Ohring, Chapter 3 - Thin-Film Evaporation Processes, Materials Science of Thin Films (Second Edition), Academic Press, San Diego, 2002, pp. 95-144.
[81] M. Ohring, Chapter 7 - Substrate Surfaces and Thin-Film Nucleation, Materials Science of Thin Films (Second Edition), Academic Press, San Diego, 2002, pp. 357-415.
[82] M. Ohring, Chapter 8 - Epitaxy, Materials Science of Thin Films (Second Edition), Academic Press, San Diego, 2002, pp. 417-494.
[83] M. Ohring, Chapter 9 - Film Structure, Materials Science of Thin Films (Second Edition), Academic Press, San Diego, 2002, pp. 495-558.
[84] Scanning Electron Microscopy, Mater. Charact.
[85] Transmission Electron Microscopy, Mater. Charact.
[86] Light Microscopy, Mater. Charact.
[87] R.b.P.D. Brown, Transmission Electron Microscopy-A Textbook for Materials Science, by David B. Williams and C. Barry Carter, Microsc. Microanal. 5(6) (2003) 452-453.
[88] L.A. Giannuzzi, B.W. Kempshall, S.M. Schwarz, J.K. Lomness, B.I. Prenitzer, F.A. Stevie, FIB Lift-Out Specimen Preparation Techniques, in: L.A. Giannuzzi, F.A. Stevie (Eds.), Introduction to Focused Ion Beams: Instrumentation, Theory, Techniques and Practice, Springer US, Boston, MA, 2005, pp. 201-228.
[89] L.A. Giannuzzi, F.A. Stevie, A review of focused ion beam milling techniques for TEM specimen preparation, Micron 30(3) (1999) 197-204.
[90] X-Ray Spectroscopy for Elemental Analysis, Mater. Charact.
[91] X-Ray Diffraction Methods, Mater. Charact.
[92] Electron Spectroscopy for Surface Analysis, Mater. Charact.
[93] R.R. Kanchi, N.K. Uttarkar, Study of Heat Loss from Hot Tungsten Filament Bulb Using AT89C51 Based Data Acquisition System, International Journal of Applied Physics and Mathematics 2(3) (2012).
[94] I.D. Baikie, P.J. Estrup, Low cost PC based scanning Kelvin probe, Rev. Sci. Instrum. 69(11) (1998) 3902-3907.
[95] I.D. Baikie, A.C. Grain, J. Sutherland, J. Law, Ambient pressure photoemission spectroscopy of metal surfaces, Applied Surface Science 323 (2014) 45-53.
[96] R.H. Fowler, The Analysis of Photoelectric Sensitivity Curves for Clean Metals at Various Temperatures, Physical Review 38(1) (1931) 45-56.
[97] G. Barillaro, Porous Silicon Gas Sensing, in: L. Canham (Ed.), Handbook of Porous Silicon, Springer International Publishing, Cham, 2014, pp. 845-856.
[98] E.J. Anglin, L. Cheng, W.R. Freeman, M.J. Sailor, Porous silicon in drug delivery devices and materials, Advanced Drug Delivery Reviews 60(11) (2008) 1266-1277.

[99] E. Luais, F. Ghamouss, J. Wolfman, S. Desplobain, G. Gautier, F. Tran-Van, J. Sakai, Mesoporous silicon negative electrode for thin film lithium-ion microbatteries, Journal of Power Sources 274(0) (2015) 693-700.
[100] G. Rong, A. Najmaie, J.E. Sipe, S.M. Weiss, Nanoscale porous silicon waveguide for label-free DNA sensing, Biosensors and Bioelectronics 23(10) (2008) 1572-1576.
[101] G. Shtenberg, E. Segal, Porous Silicon Optical Biosensors, in: L. Canham (Ed.), Handbook of Porous Silicon, Springer International Publishing, Cham, 2014, pp. 857-868.
[102] M.P. Stewart, J.M. Buriak, Chemical and Biological Applications of Porous Silicon Technology, Advanced Materials 12(12) (2000) 859-869.
[103] J. Kanungo, C. Pramanik, S. Bandopadhyay, U. Gangopadhyay, L. Das, H. Saha, T.T.G. Robert, Improved contacts on a porous silicon layer by electroless nickel plating and copper thickening, Semiconductor Science and Technology 21(7) (2006) 964.
[104] H. Saha, S.K. Dutta, S.M. Hossain, S. Chakraborty, A. Saha, Mechanism and control of formation of porous silicon onp-type Si, Bulletin of Materials Science 21(3) (1998) 195-201.
[105] M.I.J. Beale, J.D. Benjamin, M.J. Uren, N.G. Chew, A.G. Cullis, AN EXPERIMENTAL AND THEORETICAL-STUDY OF THE FORMATION AND MICROSTRUCTURE OF POROUS SILICON, Journal of Crystal Growth 73(3) (1985) 622-636.
[106] K. Kordás, J. Remes, S. Beke, T. Hu, S. Leppävuori, Manufacturing of porous silicon; porosity and thickness dependence on electrolyte composition, Applied Surface Science 178(1–4) (2001) 190-193.
[107] B.A. Boukamp, G.C. Lesh, R.A. Huggins, All-Solid Lithium Electrodes with Mixed-Conductor Matrix, J. Electrochem. Soc. 128(4) (1981) 725-729.
[108] J. Li, A.K. Dozier, Y. Li, F. Yang, Y.-T. Cheng, Crack Pattern Formation in Thin Film Lithium-Ion Battery Electrodes, J. Electrochem. Soc. 158(6) (2011) A689-A694.
[109] A.R. Beaber, J.D. Nowak, O. Ugurlu, W.M. Mook, S.L. Girshick, R. Ballarini, W.W. Gerberich, Smaller is tougher, Philos. Mag. 91(7-9) (2011) 1179-1189.
[110] Z. Bao, M.R. Weatherspoon, S. Shian, Y. Cai, P.D. Graham, S.M. Allan, G. Ahmad, M.B. Dickerson, B.C. Church, Z. Kang, H.W. Abernathy Iii, C.J. Summers, M. Liu, K.H. Sandhage, Chemical reduction of three-dimensional silica micro-assemblies into microporous silicon replicas, Nature Publishing Group, 2007, pp. 172-175.
[111] F. Dai, J. Zai, R. Yi, M.L. Gordin, H. Sohn, S. Chen, D. Wang, Bottom-up synthesis of high surface area mesoporous crystalline silicon and evaluation of its hydrogen evolution performance, Nat Commun 5 (2014).
[112] Y. Sun, T.J. Balk, Evolution of Structure, Composition, and Stress in Nanoporous Gold Thin Films with Grain-Boundary Cracks, Metall and Mat Trans A 39(11) (2008) 2656-2665.
[113] Y. Sun, S.A. Burger, T.J. Balk, Controlled ligament coarsening in nanoporous gold by annealing in vacuum versus nitrogen, Philos. Mag. 94(10) (2014) 1001-1011.
[114] Z. Lu, C. Li, J. Han, F. Zhang, P. Liu, H. Wang, Z. Wang, C. Cheng, L. Chen, A. Hirata, T. Fujita, J. Erlebacher, M. Chen, Three-dimensional bicontinuous nanoporous materials by vapor phase dealloying, Nature Communications 9(1) (2018) 276.
[115] L.Y. Beaulieu, K.W. Eberman, R.L. Turner, L.J. Krause, J.R. Dahn, Colossal Reversible Volume Changes in Lithium Alloys, Electrochemical and Solid-State Letters 4(9) (2001) A137-A140.

[116] L.-F. Cui, R. Ruffo, C.K. Chan, H. Peng, Y. Cui, Crystalline-Amorphous Core−Shell Silicon Nanowires for High Capacity and High Current Battery Electrodes, Nano Lett. 9(1) (2009) 491-495.
[117] J.P. Maranchi, A.F. Hepp, P.N. Kumta, High Capacity, Reversible Silicon Thin-Film Anodes for Lithium-Ion Batteries, Electrochemical and Solid-State Letters 6(9) (2003) A198-A201.
[118] J. Yin, M. Wada, K. Yamamoto, Y. Kitano, S. Tanase, T. Sakai, Micrometer-Scale Amorphous Si Thin-Film Electrodes Fabricated by Electron-Beam Deposition for Li-Ion Batteries, J. Electrochem. Soc. 153(3) (2006) A472-A477.
[119] T.L. Maxwell, T.J. Balk, The Fabrication and Characterization of Bimodal Nanoporous Si with Retained Mg through Dealloying, Adv. Eng. Mater. 20(2) (2018) 1700519-n/a.
[120] X. Lu, T.J. Balk, R. Spolenak, E. Arzt, Dealloying of Au–Ag thin films with a composition gradient: Influence on morphology of nanoporous Au, Thin Solid Films 515(18) (2007) 7122-7126.
[121] Y. Sun, T.J. Balk, A multi-step dealloying method to produce nanoporous gold with no volume change and minimal cracking, Scr. Mater. 58(9) (2008) 727-730.
[122] H. Fei, A. Abraham, N. Chawla, H. Jiang, Evaluation of Micro-Pillar Compression Tests for Accurate Determination of Elastic-Plastic Constitutive Relations, Journal of Applied Mechanics 79(6) (2012) 061011-061011.
[123] D. Kiener, P.J. Guruprasad, S.M. Keralavarma, G. Dehm, A.A. Benzerga, Work hardening in micropillar compression: In situ experiments and modeling, Acta Mater. 59(10) (2011) 3825-3840.
[124] H. Zhang, B.E. Schuster, Q. Wei, K.T. Ramesh, The design of accurate micro-compression experiments, Scr. Mater. 54(2) (2006) 181-186.
[125] T.L. Maxwell, T.J. Balk, The Fabrication and Characterization of Bimodal Nanoporous Si with Retained Mg through Dealloying, Adv. Eng. Mater. 20(2) (2018) 1700519.
[126] J. Schoop, T.J. Balk, Engineering Defect-Free Nanoporous Pd from Optimized Pd-Ni Precursor Alloy by Understanding Palladium-Hydrogen Interactions During Dealloying, Metall and Mat Trans A 45(4) (2014) 2309-2314.
[127] L. Wang, T.J. Balk, Synthesis of nanoporous nickel thin films from various precursors, Philosophical Magazine Letters 94(9) (2014) 573-581.
[128] Z. Zhang, Y. Wang, Z. Qi, J. Lin, X. Bian, Nanoporous Gold Ribbons with Bimodal Channel Size Distributions by Chemical Dealloying of Al−Au Alloys, The Journal of Physical Chemistry C 113(4) (2009) 1308-1314.
[129] A.A. Nayeb-Hashemi, J.B. Clark, The Mg−Si (Magnesium-Silicon) system, Bulletin of Alloy Phase Diagrams 5(6) (1984) 584-592.
[130] H.S. Chou, J.C. Huang, Y.H. Lai, L.W. Chang, X.H. Du, J.P. Chu, T.G. Nieh, Amorphous and nanocrystalline sputtered Mg–Cu thin films, J. Alloys Compd. 483(1–2) (2009) 341-345.
[131] P. Zaumseil, High-resolution characterization of the forbidden Si 200 and Si 222 reflections, J. Appl. Crystallogr. 48(Pt 2) (2015) 528-532.
[132] J.W. He, X. Xu, J.S. Corneille, D.W. Goodman, X-ray photoelectron spectroscopic characterization of ultra-thin silicon oxide films on a Mo(100) surface, Surface Science 279(1) (1992) 119-126.

[133] C.-H. Huang, Y.-L. Jan, W.-C. Lee, Investigation of Mg(O,OH) Films Prepared by Chemical Bath Deposition as Buffer Layers for Cu(In,Ga)Se2 Solar Cells, J. Electrochem. Soc. 158(9) (2011) H879-H888.
[134] L. Savio, E. Celasco, L. Vattuone, M. Rocca, Enhanced Reactivity at Metal−Oxide Interface: Water Interaction with MgO Ultrathin Films, The Journal of Physical Chemistry B 108(23) (2004) 7771-7778.
[135] M. Taheri, R.C. Phillips, J.R. Kish, G.A. Botton, Analysis of the surface film formed on Mg by exposure to water using a FIB cross-section and STEM–EDS, Corros. Sci. 59 (2012) 222-228.
[136] G.L. Makar, J. Kruger, Corrosion of magnesium, International Materials Reviews 38(3) (1993) 138-153.
[137] P.O. Guglielmi, E.G. Herbert, L. Tartivel, M. Behl, A. Lendlein, N. Huber, E.T. Lilleodden, Mechanical characterization of oligo(ethylene glycol)-based hydrogels by dynamic nanoindentation experiments, J. Mech. Behav. Biomed. Mater. 46 (2015) 1-10.
[138] J. Hay, E. Herbert, Measuring the Complex Modulus of Polymers by Instrumented Indentation Testing, Exp. Tech. 37(3) (2013) 55-61.
[139] E.G. Herbert, W.E. Tenhaeff, N.J. Dudney, G.M. Pharr, Mechanical characterization of LiPON films using nanoindentation, Thin Solid Films 520(1) (2011) 413-418.
[140] H. Jia, P. Gao, J. Yang, J. Wang, Y. Nuli, Z. Yang, Novel Three-Dimensional Mesoporous Silicon for High Power Lithium-Ion Battery Anode Material, Adv. Energy Mater. 1(6) (2011) 1036-1039.
[141] M.N. Obrovac, L. Christensen, D.B. Le, J.R. Dahn, Alloy Design for Lithium-Ion Battery Anodes, J. Electrochem. Soc. 154(9) (2007) A849-A855.
[142] T. Shen, Z. Yao, X. Xia, X. Wang, C. Gu, J. Tu, Rationally Designed Silicon Nanostructures as Anode Material for Lithium-Ion Batteries, Adv. Eng. Mater. 1700591-n/a.
[143] W.D. Nix, Elastic and plastic properties of thin films on substrates: nanoindentation techniques, Mater. Sci. Eng., A 234-236(Supplement C) (1997) 37-44.
[144] J. Capodagli, R. Lakes, Isothermal viscoelastic properties of PMMA and LDPE over 11 decades of frequency and time: a test of time–temperature superposition, Rheol. Acta 47(7) (2008) 777-786.
[145] L. Guerdoux, R.A. Duckett, D. Froelich, Physical ageing of polycarbonate and PMMA by dynamic mechanical measurements, Polymer 25(10) (1984) 1392-1396.
[146] M.L. Oyen, R.F. Cook, Load–displacement behavior during sharp indentation of viscous–elastic–plastic materials, J. Mater. Res. 18(01) (2003) 139-150.
[147] F. Stan, C. Fetecau, Characterization of viscoelastic properties of molybdenum disulphide filled polyamide by indentation, Mech. Time-Depend. Mater. 17(2) (2013) 205-221.
[148] Z. Chen, X. Wang, V. Bhakhri, F. Giuliani, A. Atkinson, Nanoindentation of porous bulk and thin films of La0.6Sr0.4Co0.2Fe0.8O3−δ, Acta Mater. 61(15) (2013) 5720-5734.
[149] T. Juarez, J. Biener, J. Weissmüller, A.M. Hodge, Nanoporous Metals with Structural Hierarchy: A Review, Adv. Eng. Mater. 19(12) (2017) 1700389.
[150] V. Kulikovsky, V. Vorlíček, P. Boháč, M. Stranyánek, R. Čtvrtlík, A. Kurdyumov, L. Jastrabik, Hardness and elastic modulus of amorphous and nanocrystalline SiC and Si films, Surf. Coat. Technol. 202(9) (2008) 1738-1745.

[151] R. Liu, A. Antoniou, A relation between relative density, alloy composition and sample shrinkage for nanoporous metal foams, Scr. Mater. 67(12) (2012) 923-926.
[152] W.E. Forsythe, A.G. Worthing, The Properties of Tungsten and the Characteristics of Tungsten Lamps, Astrophys. J. 61 (1925) 146.
[153] Z.G. Liu, L. Lu, M.O. Lai, Synthesis of nanocrystalline carbide in tungsten alloy by mechanical alloying and annealing, J. Alloys Compd. 394(1) (2005) 176-180.
[154] G.A. Niklasson, C.G. Granqvist, Electrochromics for smart windows: thin films of tungsten oxide and nickel oxide, and devices based on these, J. Mater. Chem. 17(2) (2007) 127-156.
[155] M. Rieth, S.L. Dudarev, S.M. Gonzalez de Vicente, J. Aktaa, T. Ahlgren, S. Antusch, D.E.J. Armstrong, M. Balden, N. Baluc, M.F. Barthe, W.W. Basuki, M. Battabyal, C.S. Becquart, D. Blagoeva, H. Boldyryeva, J. Brinkmann, M. Celino, L. Ciupinski, J.B. Correia, A. De Backer, C. Domain, E. Gaganidze, C. García-Rosales, J. Gibson, M.R. Gilbert, S. Giusepponi, B. Gludovatz, H. Greuner, K. Heinola, T. Höschen, A. Hoffmann, N. Holstein, F. Koch, W. Krauss, H. Li, S. Lindig, J. Linke, C. Linsmeier, P. López-Ruiz, H. Maier, J. Matejicek, T.P. Mishra, M. Muhammed, A. Muñoz, M. Muzyk, K. Nordlund, D. Nguyen-Manh, J. Opschoor, N. Ordás, T. Palacios, G. Pintsuk, R. Pippan, J. Reiser, J. Riesch, S.G. Roberts, L. Romaner, M. Rosiński, M. Sanchez, W. Schulmeyer, H. Traxler, A. Ureña, J.G. van der Laan, L. Veleva, S. Wahlberg, M. Walter, T. Weber, T. Weitkamp, S. Wurster, M.A. Yar, J.H. You, A. Zivelonghi, Recent progress in research on tungsten materials for nuclear fusion applications in Europe, J. Nucl. Mater. 432(1) (2013) 482-500.
[156] R.S. Vidyarthy, D.K. Dwivedi, Activating flux tungsten inert gas welding for enhanced weld penetration, Journal of Manufacturing Processes 22 (2016) 211-228.
[157] R.G. Abernethy, Predicting the performance of tungsten in a fusion environment: a literature review, Mater. Sci. Technol. 33(4) (2017) 388-399.
[158] H.E. Exner, J. Gurland, A REVIEW OF PARAMETERS INFLUENCING SOME MECHANICAL PROPERTIES OF TUNGSTEN CARBIDE–COBALT ALLOYS, Powder Metall. 13(25) (1970) 13-31.
[159] A. Marin, C.P. Lungu, C. Porosnicu, Influence of gaseous inclusions on aluminum-tungsten coatings investigated by XPS, J. Vac. Sci. Technol., A 35(6) (2017) 061304.
[160] M. Rafiei, S. Khademzadeh, N. Parvin, Characterization and formation mechanism of nanocrystalline W–Al alloy prepared by mechanical alloying, J. Alloys Compd. 489(1) (2010) 224-227.
[161] H.G. Tang, X.F. Ma, W. Zhao, X.W. Yan, R.J. Hong, Preparation of W–Al alloys by mechanical alloying, J. Alloys Compd. 347(1–2) (2002) 228-230.
[162] S.H. Yao, Synthesis, characterisation and wear performance of W–Al coatings, Mater. Res. Innovations 18(sup2) (2014) S2-233-S2-237.
[163] S. Higashino, M. Miyake, H. Fujii, A. Takahashi, T. Hirato, Electrodeposition of Al-W Alloy Films in a 1-Ethyl-3-methyl-imidazolium Chloride-AlCl3 Ionic Liquid Containing W6Cl12, J. Electrochem. Soc. 164(4) (2017) D120-D125.
[164] M. Metikoš-Huković, N. Radić, Z. Grubač, H.A. Tonejcv, The corrosion behavior of sputter-deposited aluminum–tungsten alloys, Electrochim. Acta 47(15) (2002) 2387-2397.
[165] C. Zhang, P. Lv, J. Cai, Y. Zhang, H. Xia, Q. Guan, Enhanced corrosion property of W-Al coatings fabricated on aluminum using surface alloying under high-current pulsed electron beam, J. Alloys Compd. 723 (2017) 258-265.

[166] R.H. Davies, A.T. Dinsdale, J.A. Gisby, S.M. Martin, Thermodynamic and Phase Equilibrium SOftware from the National Physical Laboratory, CALPHAD: Comput. Coupling Phase Diagrams Thermochem. 26(2) (2002) 229-271.
[167] K.T. Jacob, S. Raj, L. Rannesh, Vegard's law: a fundamental relation or an approximation?, International Journal of Materials Research 98(9) (2007) 776-779.
[168] V.A. Lubarda, On the effective lattice parameter of binary alloys, Mech. Mater. 35(1) (2003) 53-68.
[169] S.T. Murphy, A. Chroneos, C. Jiang, U. Schwingenschlögl, R.W. Grimes, Deviations from Vegard's law in ternary III-V alloys, Phys. Rev. B 82(7) (2010) 073201.
[170] L. Vegard, Die Konstitution der Mischkristalle und die Raumfüllung der Atome, Zeitschrift für Physik 5(1) (1921) 17-26.
[171] H.W. King, Quantitative size-factors for metallic solid solutions, Journal of Materials Science 1(1) (1966) 79-90.
[172] S. Diplas, G. Shao, S.A. Morton, P. Tsakiropoulos, J.F. Watts, Calculations of charge transfer in Nb–17Al and V–50Al alloys, using the Auger parameter, Intermetallics 7(8) (1999) 937-946.
[173] S. Diplas, G. Shao, P. Tsakiropoulos, J.F. Watts, J.A.D. Matthew, Calculations of charge transfer in Mg–and Al–transition metal alloys using the Auger parameter, Surf. Interface Anal. 29(1) (2000) 65-72.
[174] D. Chen, Z. Chen, J. Cai, Z. Chen, Preparation of W–Al intermetallic compound powders by a mechanochemical approach, J. Alloys Compd. 461(1) (2008) L23-L25.
[175] S. Higashino, M. Miyake, A. Takahashi, Y. Matamura, H. Fujii, R. Kasada, T. Hirato, Evaluation of the hardness and Young's modulus of electrodeposited Al–W alloy films by nano-indentation, Surf. Coat. Technol. 325 (2017) 346-351.
[176] D. Kek Merl, P. Panjan, J. Kovač, Corrosion and surface study of sputtered Al–W coatings with a range of tungsten contents, Corros. Sci. 69 (2013) 359-368.
[177] D. Kek Merl, P. Panjan, I. Milošev, Effect of tungsten content on properties of PVD sputtered Al-WX alloys, Surf. Eng. 29(4) (2013) 281-286.
[178] X. Nie, S. Mao, M. Yan, J. Li, Z. Song, Structure and property transitions of Al-based binary alloy coatings by magnetron sputtering, Surf. Coat. Technol. 254 (2014) 455-461.
[179] C.J. Zhu, X.F. Ma, W. Zhao, H.G. Tang, J.M. Yan, S.G. Cai, Processing, microstructure and mechanical properties of W50Al50 bulk alloy obtained by mechanical alloying and hot-pressing, Scr. Mater. 51(10) (2004) 993-997.
[180] C.J. Zhu, X.F. Ma, W. Zhao, H.G. Tang, J.M. Yan, S.G. Cai, Synthesis and thermal stability of Al75W25 alloy obtained by mechanically alloying, J. Alloys Compd. 393(1) (2005) 248-251.
[181] G. Kresse, J. Furthmuller, Efficient iterative schemes for *ab initio* total-energy calculation using a plane-wave basis set, Phys. Rev. B 54(16) (1996) 11169-11186.
[182] J.P. Perdew, K. Burke, M. Enrnzerhof, Generalized gradient approximation made simple, Phys. Rev. Lett. 77(18) (1996) 3865-3868.
[183] W. Tang, E. Sanville, G. Henkelman, A grid-based Bader analysis algorithm without lattice bias, J. Phys.: Condens. Matter 21(8) (2009) 084204.
[184] K. Momma, F. Izumi, VESTA 3 for three-dimensional visualization of crystal, volumetric and morphology data, J. Appl. Crystallogr. 44(6) (2011) 1272-1276.

[185] B. Pines, On Solid Solutions | The elastic sphere model as applied to solid solutions and deviations from Vegard's rule, Journal of Physics-USSR 3 (1940) 309-319.
[186] G. Shao, P. Tsakiropoulos, Lattice parameters of TM(3d)–Al solid solutions, Materials Science and Engineering: A 271(1) (1999) 286-290.
[187] R.F.W. Bader, Atoms in Molecules - A Quantum Theory Oxford University Press1990.
[188] P.S. Bagus, F. Illas, G. Pacchioni, F. Parmigiani, Mechanisms responsible for chemical shifts of core-level binding energies and their relationship to chemical bonding, J. Electron. Spectrosc. Relat. Phenom. 100(1) (1999) 215-236.
[189] P.S. Bagus, E.S. Ilton, C.J. Nelin, The interpretation of XPS spectra: Insights into materials properties, Surface Science Reports 68(2) (2013) 273-304.
[190] W.F. Egelhoff, Core-level binding-energy shifts at surfaces and in solids, Surface Science Reports 6(6) (1987) 253-415.
[191] K. Siegbahn, A Discussion on photoelectron spectroscopy - Electron spectroscopy for chemical analysis (e.s.c.a.), Philos. Trans. R. Soc., A 268(1184) (1970) 33.
[192] S. Halas, T. Durakiewicz, Is work function a surface or a bulk property?, Vacuum 85(4) (2010) 486-488.
[193] N.D. Lang, W. Kohn, Theory of Metal Surfaces: Work Function, Phys. Rev. B 3(4) (1971) 1215-1223.
[194] J.A. Rothschild, M. Eizenberg, Work function calculation of solid solution alloys using the image force model, Phys. Rev. B 81(22) (2010) 224201.
[195] I. Brodie, Uncertainty, topography, and work function, Phys. Rev. B 51(19) (1995) 13660-13668.
[196] T. Durakiewicz, S. Halas, A. Arko, J.J. Joyce, D.P. Moore, Electronic work-function calculations of polycrystalline metal surfaces revisited, Phys. Rev. B 64(4) (2001) 045101.
[197] H. Stanislaw, D. Tomasz, Work functions of elements expressed in terms of the Fermi energy and the density of free electrons, J. Phys.: Condens. Matter 10(48) (1998) 10815.
[198] H. Lu, Z. Liu, X. Yan, D. Li, L. Parent, H. Tian, Electron work function–a promising guiding parameter for material design, Scientific Reports 6 (2016) 24366.
[199] C.J. Todd, T.N. Rhodin, Work function in field emission — the (110) plane of tungsten, Surface Science 36(1) (1973) 353-369.
[200] O.O. Okudur, K. Vanstreels, I. de Wolf, U. Hangen, A. Qiu, Substrate Independent Elastic Modulus of Thin Low Dielectric Constant Materials, Adv. Eng. Mater. 19(8) (2017) 1600653-n/a.
[201] Z. Zeng, X. Ma, J. Chen, Y. Zeng, D. Yang, Y. Liu, Effects of heavy phosphorus-doping on mechanical properties of Czochralski silicon, J. Appl. Phys. 107(12) (2010) 123503.
[202] H.L. Sun, Z.X. Song, D.G. Guo, F. Ma, K.W. Xu, Microstructure and Mechanical Properties of Nanocrystalline Tungsten Thin Films, Journal of Materials Science & Technology 26(1) (2010) 87-92.
[203] H. Guomin, L. Dongyang, The correlation between the electron work function and yield strength of metals, physica status solidi (b) 249(8) (2012) 1517-1520.
[204] G. Hua, D. Li, Generic relation between the electron work function and Young's modulus of metals, Applied Physics Letters 99(4) (2011) 041907.

[205] H. Lu, G. Hua, D. Li, Dependence of the mechanical behavior of alloys on their electron work function—An alternative parameter for materials design, Applied Physics Letters 103(26) (2013) 261902.

Vita

Tyler L. Maxwell was born in Lexington, Ky, and raised in the foothills of the Appalachian Mountains in Whitley City, Ky. He graduated from Berea College in 2013 with a degree in physics and immediately started graduate school at the University of Kentucky under the supervision of Dr. T. John Balk during the summer of 2013 to pursue a Ph.D. in Materials Science and Engineering.

Peer-reviewed Papers and Conference Proceedings

1. **Maxwell, T. L.,** Zhou, Q., Liu, X., Vancil, B. K., Beck, M. J. & Balk, T. J. A Fundamental Study of W-Al Alloying and Modifications of Electronic State. *Journal of Alloys and Compounds.* **In preparation.**
2. **Maxwell, T. L.** & Balk, T. J. An Investigation of the Mechanical Behavior of Bimodal Nanoporous Si-Mg Films through Nanoindentation. *Global Challenges.* **Under review**.
3. Liu, X., Zhou, Q., **Maxwell, T. L.,** Vancil, B. K., Beck, M. J., Balk, T. J. Scandate Cathode Surface Characterization: Emission Testing, Elemental Analysis and Morphological Evaluation. *Materials Characterization,* (2018).
4. Zhou, Q., Liu, X., **Maxwell, T. L.,** Vancil, B. K., Balk, T. J., Beck, M. J. $Ba_xSc_yO_z$ on W (001), (110), and (112) in Scandate Cathodes: Connecting to Experiment via μ_O and Equilibrium Crystal Shape. *Applied Surface Science,* (2018).
5. **Maxwell, T. L.,** Zhou, Q., Liu, X., Vancil, B. K., Beck, M. J. & Balk, T. J. Scandate Cathode Work Function Measurements at Elevated Temperature. *Proceedings of*

the 2018 IEEE International Vacuum Electronics Conference (IVEC), 229-230 (2018).

6. Liu, X., **Maxwell, T. L.,** Zhou, Q., Vancil, B. K., Beck, M. J. & Balk, T. J. Characterization of Scandate Cathode at Different Stages of Processing. *Proceedings of the 2018 IEEE International Vacuum Electronics Conference (IVEC)*, 233-234 (2018).
7. Zhou, Q., Liu, X., **Maxwell, T. L.,** Vancil, B. K., Balk, T. J. & Beck, M. J. Mapping Conditions for the Formation of High-Performance Scandate Cathodes: New Insights into the Role of Sc. *Proceedings of the 2018 IEEE International Vacuum Electronics Conference (IVEC)*, 325-326 (2018).
8. Liu, X., Zhou, Q., **Maxwell, T. L.,** Vancil, B. K., Beck, M. J. & Balk, T. J. Analysis of Faceted Tungsten Grains on the Surfaces of Scandate Cathodes Fabricated from L-S and L-L Powders. *Proceedings of the 2018 IEEE International Vacuum Electronics Conference (IVEC)*, 323-324 (2018).
9. Beck, M. J., Zhou, Q., Liu, X., **Maxwell, T. L.,** Vancil, B. K. & Balk, T. J. The Dipole Model at the Atomic Scale: Explaining Variations in Work Function Due to Configurational and Compositional Changes in Ba/Sc/O/ Adsorbates on W (001), (110), and (112). *Proceedings of the 2018 IEEE International Vacuum Electronics Conference (IVEC)*, 43-44 (2018).
10. Balk, T. J., Liu, X., Zhou, Q., **Maxwell, T. L.,** Vancil, B. K. & Beck, M. J. Materials Characterization of Surface Phases in Scandate Cathodes. *Proceedings of the 2018 IEEE International Vacuum Electronics Conference (IVEC)*, 329-330 (2018).

11. **Maxwell, T. L.** & Balk, T. J. The Fabrication and Characterization of Bimodal Nanoporous Si with Retained Mg through Dealloying. *Advanced Engineering Materials.* **20,** 1700519 (2018).

12. Chang-Eun, K., Rahimi, R. M., **Maxwell, T. L.**, Balk, T. J. & Bahr, D. F. Age-hardening in a two component immiscible nanolaminate metal system. *Scripta Materilia.*, **136,** 33-36 (2017).

Conferences Participations

1. *The Physical Behavior and Characterization of Nanoporous Silicon and Dispenser Cathode Surfaces,* **Maxwell, T. L.,** Zhou, Q., Liu, X., Vancil, B. K., Beck, M. J., & Balk, T. J.; Local graduate program symposium during the Spring of 2018, Lexington, KY.

2. *Scandate Cathode Work Function Measurements at Elevated Temperature,* **Maxwell, T. L.** Zhou, Q., Liu, X. Vancil, B. K., Beck, M. J. & Balk; IVEC Spring meeting 2018, Monterey, CA.

3. *Investigation of Time-Dependent Deformation of Porous Silicon through Nanoindentation,* **Maxwell, T. L.** & Balk, T. J.; Mechanical Behavior and Failure Mechanisms of Materials at MRS Fall meeting 2016, Boston, MA.

4. *Deformation Behavior of Nanoporous Silicon and Gold During Nanoindentation and Cyclic Loading,* **Maxwell, T. L.,** Briot, N. J., & Balk, T. J.; Second International Symposium on Nanoporous Materials by Alloy Corrosion, Lake Bostal, Germany.

5. *Time-Dependent Mechanical Behavior of Porous Silicon,* **Maxwell, T. L.,** & Balk, T. J.; Thin Film and Small Scale Mechanical Behavior, The Gordon Research Conference, Summer 2016, Lewiston, ME.

6. *The Fabrication and Deformation of Nanoporous Silicon,* **Maxwell, T. L,** & Balk, T. J.; Mechanical Behavior at the Nanoscale, MRS Fall meeting 2015, Boston, MA.